Identification of dynamic properties via a method based on Force Analysis Technique : application to flax fibre reinforced PA11

Federico Amenini

THESE DE DOCTORAT DE

L'UNIVERSITE BRETAGNE SUD
COMUE UNIVERSITE BRETAGNE LOIRE

ECOLE DOCTORALE N° 602
Sciences pour l'Ingénieur
Spécialité : *Mécanique des solides, des matériaux, des structures et des surfaces*

Par

Federico AMENINI

Identification of dynamic properties via a method based on Force Analysis Technique: application to flax fibre reinforced PA11

Thèse présentée et soutenue à Laval, le 15 octobre 2019
Unité de recherche : Estaca'Lab, Pôle Mécanique des Structures Composites et Environnement
IRDL, UMR CNRS 6027, Université Bretagne Sud
Thèse N° : 532

Rapporteurs avant soutenance :

Manuel Collet Directeur de recherche CNRS, Ecole Centrale de Lyon
Vincent Placet Ingénieur de Recherche - HDR, Université de Franche-Comté

Composition du Jury :

Président :	Laurent Guillaumat	Professeur des universités, ENSAM
Examinateurs :	Jean-Michel Génevaux	Professeur des universités, Le Mans Université
	Christophe Poilane	Maître de conférences - HDR, Université de Caen Normandie
	Manuel Collet	Directeur de recherche CNRS, Ecole Centrale de Lyon
	Vincent Placet	Ingénieur de Recherche - HDR, Université de Franche-Comté
Dir. de thèse :	Sandrine Thuillier	Professeur des universités, Université Bretagne Sud
Co-dir. de thèse :	Julien Brocail	Maître de conférences, ESTACA
	Michael Chauvin	Maître de conférences, ESTACA

No wise fish would go anywhere without a porpoise.

(Lewis Carroll)

Acknowledgments

Les travaux de cette thèse ont été effectués au sein de l'Ecole Supérieure des Techniques Aéronautiques et de Construction Automobile (ESTACA) dans le cadre d'un projet de collaboration avec l'Institut de Recherche Dupuy de Lôme (IRDL) de l'Université Bretagne Sud (UBS).

Je tiens à remercier Monsieur Manuel Collet, Directeur de recherche CNRS à l'Ecole Centrale de Lyon, ainsi que Monsieur Vincent Placet, Ingénieur de recherche HDR à l'Université de Franche-Compté pour avoir accepté d'être rapporteurs. Je remercie aussi Monsieur Laurent Guillaumat, Professeur à l'ENSAM d'Angers, Monsieur Jean-Michel Génevaux, Professeur de l'Université du Maine et Monsieur Christophe Poilâne, Maître de conférences HDR de l'Université de Caen Normandie, d'avoir accepté d'examiner ces travaux de thèse.

Je remercie la directrice de thèse Sandrine Thuillier pour m'avoir guidé avec patience tout au long de ce doctorat, pour sa disponibilité et ses conseils. Merci également à Julien Brocail et Michael Chauvin pour leur encadrement et nos échanges quotidiens qui ont fait de cette période une expérience humainement riche.

Merci aux collègues et amis de l'ESTACA : Romain, pour ces trois ans de partage et énorme divertissement, Anthony pour les discussions et les diners délicieux, Stéphane pour nos rendez-vous sportifs et ceux moins sains (Eveline me doit encore 20 francs, pas un de moins pas un de plus), Virginie et sa famille, Margaux, Béatrice, Melanie, les anciens Jean pour la potion magique et Yann pour m'avoir toujours surveillé, les stagiaires Fréderic et Guillaume. Je remercie tous les enseignants, les enseignants-chercheurs, techniciens, les personnes de l'ADE pour chaque interaction toujours agréable. Merci aussi à l'inconnue infirmière qui m'a accompagné longtemps dans cette expérience.

Merci aux collègues de l'UBS, en particulier Stéphanie, Cynthia, Amine et Miguel pour les moments partagés ensemble ces quatre derniers mois.

Merci également à Valentin, Julie et Johanne pour avoir rendu agréable chaque soir et... RAF !

Merci à Nono et Coco, ainsi que mes amis angevins et ceux qui sont plus loin, pour chaque discussion, chaque rigolade, chaque verre, chaque moment passé ensemble.

Un grande ringraziamento alla mia famiglia: grazie a mio padre, mia madre, Sara, Francesca e Mauro, per avermi spinto sempre a fare di più, con il loro inesorabile sostegno e saggi consigli.

Contents

List of Figures

List of Tables

Introduction

In recent years, special consideration is given to energy and environmental issues. The so called *2030 climate & energy framework* is a protocol of intentions signed by the European Union (EU) members which imposes the achievement of three main targets [1]:

- at least 40% cut in greenhouse gas emissions (from 1990 levels),
- at least 27% share for renewable energy,
- at least 27% improvement in energy efficiency.

This framework is in line with the longer term perspective included in the *Roadmap for moving to a competitive low carbon economy in 2050* [1]. Such energy policies lead to a reduction of the EU energy imports, ensuring the supplies by a larger use of sustainable energy. Moreover, they brings environmental and health benefits. Measures to reach the targets fixed in the *2030 climate & energy framework* are adopted by the Member States in many fields, such as agriculture, industry, buildings and transports [2]. In particular, as 25% of the world fuel consumption is due to transportation [3], car manufacturers point towards two main directions to reduce this contribution: the first is represented by the efficiency improvement by alternative fuels and powertrain systems [4, 5]; the second is the mass reduction by innovative design, where components are optimized to achieve the best compromise between their performances and mass, and a massive application of composite materials, even on low and mid range vehicles.

Polymer matrix composite materials are actually characterised by very good mechanical properties and by a low density. This makes them a good substitute to traditional materials such as steel. Indeed, it has been estimated that the use of glass fibre reinforced polymers for vehicle structural components leads to 35% of weight reduction and this contribution increases up to 65% with the use of carbon fibre reinforced polymers [6]. Furthermore, such materials have been recently produced by additive manufacturing, which gives net shape pieces with complex geometry, without joint or multi-step processes [7, 8]. Unfortunately, compared to steel, composite materials presents higher production costs [6] and their manufacturing processes are more energy intensive then those of metallic materials [9]. Furthermore, most composites are derived from synthetic raw materials of petrochemical origin or using chemical processes. Fibres such as aramide, carbon and glass used as reinforcement of epoxy, polyamide or other matrices, constitute composite materi-

als that, even if they achieve for the structure light-weighting, do not respect the more and more developed environmental awareness.

Natural plant fibres such as flax, hemp or sisal are considered as a good alternative to the glass fibres [10, 11]. Their advantages are not only the environmental and energy impacts, but also the recyclability [12, 13], the light-weighting capacity as well as the low price [14]. For these reasons, hemp and flax fibres are more and more used in the automotive industry. The Eco Elise (Fig. 1), a prototype manufactured by Lotus and produced with a large use of hemp and sisal fibres, represents a valid example [15]. Moreover, important progress is being made in the development of natural matrices [16]. In particular, thermoplastic matrices such as polylactic acid (PLA), polypropylene (PP) or polyamide 11 (PA11) are of special interest for their renewable source as well as their recyclability. Such matrices reinforced by plant fibre represent the constituents for 100% bio-sourced material.

Fig. 1. The Lotus Eco Elise is manufactured using sustainable hemp technical fabrics as the primary constituent in the composite body panels and spoiler. Car dimensions are 3726 mm $\times$ 1719 mm $\times$ 1202 mm [15].

The interest of natural fibres for automotive industry lies not only in the good light-weighting process nor in the environmental advantages, but also in their good damping properties. Such a characteristic suggests their use for all structures in which vibration and noise comfort is required. An application of flax fibres for the realization of a car door panel is shown in Fig. 2. Indeed, for such applications, the use of materials characterized by high damping allows significant noise absorption [17, 18, 19]. Moreover, vehicle interior noise covers frequencies up to 4000 Hz [20]. Thus, the knowledge of the material dynamical properties over a wide range of frequencies is important. For this purpose, the application of a vibratory method for the characterization of the

Fig. 2. Automotive door panel made with flax fibres [21]. Dimensions of about 1 m.

dynamical properties of flax fibre reinforced polyamide 11 biocomposite represents the objective of this PhD study.

The first chapter of this thesis presents a bibliographic study on the raw materials used in the elaboration of composite. The process to obtain flax fibres (FF) is described from the sowing to the spinning. The structure of flax fibre as well as its mechanical properties are also presented. Afterwards, the polyamide 11 is introduced by the description of the synthesis process from the castor oil, from which it derives, to the polymer, as well as its mechanical properties. The manufacturing process usually used for FF reinforced PA11 is the film stacking and hot moulding process. A bibliographic study on the parameters involved in the manufacturing process is then presented. An overall description of the static and dynamical properties, as well as of the aptitude to impact resistance and recycling, completes the literature review on FF/PA11. The second

part of the chapter is then addressed to the characterization of the composite elaborated for this study constituted by PA11 matrix reinforced by unidirectional FF with a fibre volume fraction of 42 %. The attention is firstly focused on the microstructure analysed by Scanning Electron Microscopy (SEM) and X-ray tomography. Quasi-static mechanical tests are then performed and Young's modulus values are compared with results available in literature for several orientations to the fibre direction. Moreover, FF/PA11 composite is sensitive to ageing and the evolution of the mechanical properties is evaluated. Stress-relaxation tests are also conducted with the purpose to characterize the visco-elastic properties. Beyond confirming the good potential of FF/PA11, this chapter highlights the lack of information available on the material dynamical properties over a wide range of frequencies.

The second chapter is dedicated to the introduction of the dynamical property identification method used in this study. This method uses the local equation of motion of a thin plate together with the measured displacement field of a vibrating plate to identify the material dynamical properties. The theoretical background is firstly discussed, presenting the equation of motion as well as the approximation of the fourth order derivative expression involved. As the measurement of the displacement field is generally affected by noise, a preliminary step of signal windowing and filtering is necessary. The expression of the window and filter are thus presented as well as the algorithm for the application of the method. Digital Image Correlation is firstly used to measure the displacements of a vibrating plate. Thereafter, the laser Doppler vibrometer (LDV) is used because of its better reliability. Such a technique is firstly validated on a sheet moulding compound (SMC) plate, then used for the dynamic properties identification of 3 flax fibre reinforced plates.

Finally, the third chapter deals with an analysis of several parameter affecting the method results. A repeatability and reproducibility analysis is first carried out. Thereafter, a sensitivity analysis of the parameters involved in the identification method is conducted. The influence of the noise affecting the displacement field measurements is firstly addressed. Then, an analysis of the window and filter parameter is carried out. Moreover, the effects of the spatial resolution used in the displacement measurement is discussed. An improved method is proposed to automatically select the spatial step in agreement with the frequency. The influence of the dimensions of the area of interest, as well as its shape and location, is then investigated.

Conclusions and perspectives are then presented in the last chapter.

1

Flax fibre reinforced PA11

Contents

1.1 Introduction

This chapter is dedicated to a bibliographic study on the constituents, the elaboration and properties of FF/PA11 composites and to the presentation of the material of the present PhD work. Firstly, the flax fibres are described, focusing the attention on the growing process, the structure of the flax fibre and its properties. Then, the PA11 polymer is described from the synthesis process to the thermal and mechanical properties. An overview of the manufacturing process of the composite is presented and, in particular, the parameters that influence the mechanical behaviour of the composite are discussed. Quasi-static tensile properties as well as dynamic properties are also presented. The state of the art is then completed by a presentation of impact and post-impact behaviour and the recyclability. In the second part of the chapter, the raw materials used for the composite manufacturing and the film stacking and hot moulding process are presented. The parameters of the manufacturing process are chosen from the literature in such a way as to obtain a good quality of fibre/matrix interphase. Scanning electron microscopy (SEM) and X-ray tomography are carried out to have a knowledge of the composite structure at the microscale. SEM observations allow to verify that no porosity is present and that a good fibre impregnation is obtained after the manufacturing process. X-ray tomography allows to measure the fibre misalignment in the composite, which can have a crucial impact on the mechanical properties. Results on quasi-static tensile tests are also discussed and compared with available data from literature; ageing of FF/PA11 composite is also shortly addressed. A study on the visco-elastic properties is carried out by stress-relaxation tests and Dynamic Mechanical Analysis tests.

1.2 Bibliographic study

1.2.1 Flax fibres

Plant fibres such as flax, hemp and jute, have several economical, technical and ecological advantages over synthetic fibres in reinforcing polymer composites [22, 23]. Their abundance, low cost of raw material, low density and high specific properties, make them likely substitutes to some traditional composite reinforcements [24, 25]. As it can be observed in Fig. 1.1 where the ratio between Young's modulus and fibre density is reported for different materials, flax fibres have one of the best specific elastic properties among the natural fibres. A comparison of the costs per unit

length between natural and E-glass fibres is shown in Fig. 1.2. These values are obtained for fibres capable to resist a load of 100 kN, taking into account the costs per weight, the fibre density as well as the fibre tensile strength. This comparison shows how only some natural fibres are able to compete with glass fibres, particularly jute, sisal, kenaf, bamboo, and low cost flax or hemp [22]. For these reasons, flax fibre is chosen as composite reinforcement in this study.

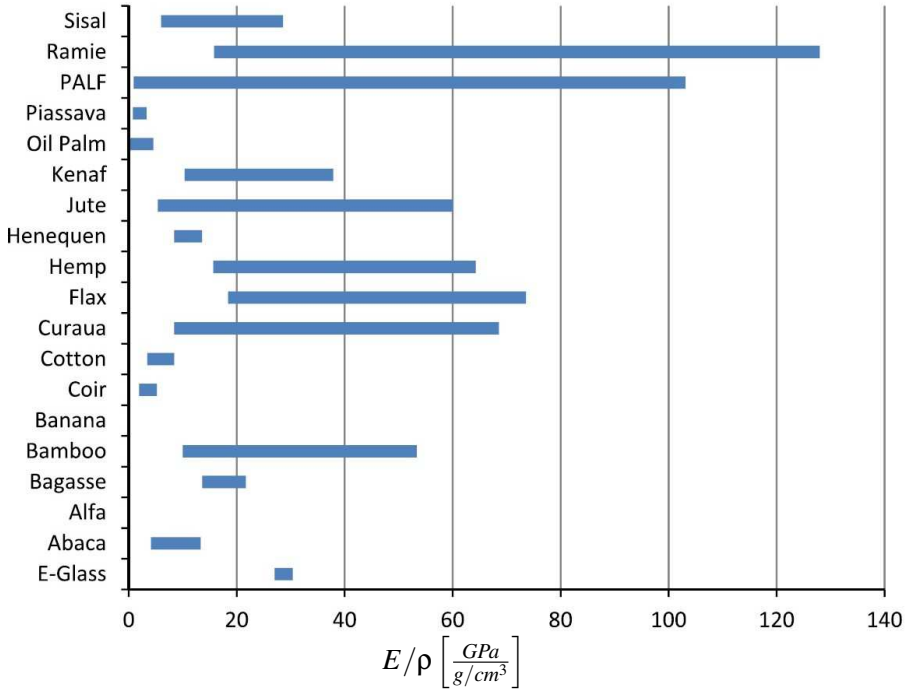

Fig. 1.1. Comparison between specific moduli of several natural fibres and E-glass fibre [22].

To obtain the flax fibres ready to be used as reinforcement in composite materials, a long process is necessary. In Europe, the period of sowing flax seeds is between March and April. Once the plant reaches maturity and flowers appear, between June and July, it is harvested [26]. Later, the retting process takes place: the plant is laid on the soil and, with the action of micro-organisms and moisture, the cellular tissues and pectins surrounding bast-fibre bundles are dissolved or rot away and so separation of the fibre from the stem is made easier [27, 28]. The separation process is carried out in two steps: the scutching process allow to separate the impurities from the raw materials such as the straw and the woody stem; and the combing, a process to separate out short and long fibres [29]. The long fibres are then ready for spinning. In the composite manufacturing, different configurations of flax fibre can be used: woven fibres can be found in unidirectional or multiaxial configurations, while non-woven fibres are generally randomly distributed.

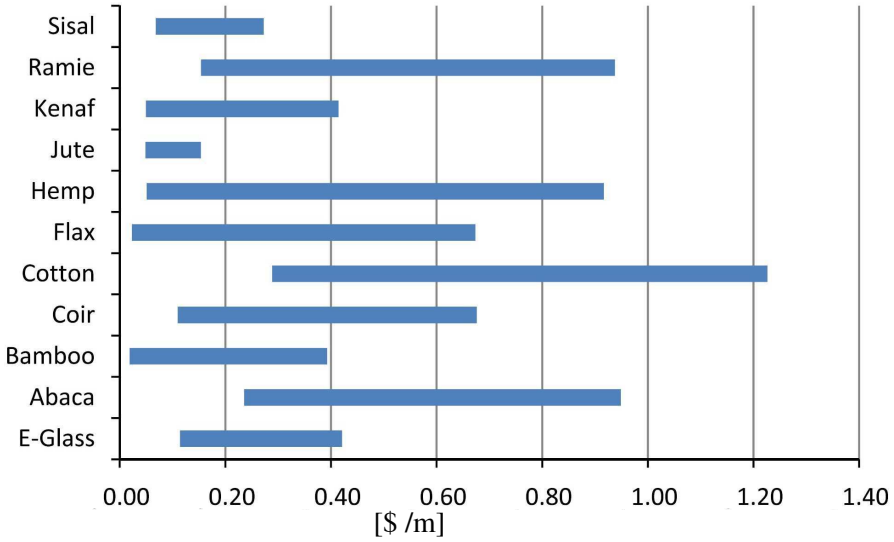

Fig. 1.2. Comparison between costs in $\$/m$ of several natural fibres and E-glass fibre [22].

The structure of flax, from the stem to the fibre, is shown in Fig. 1.3. The stem (1), of a diameter of about 1 mm to 3 mm [30], has a complex structure composed from the outer by the bark (the outer part), the phloem constituted by fibre bundles, and the xylem which is a thick layer of wood enclosing a central void. The phloem is composed by 20 to 50 bundles of fibres (2), which in their turn include 10 to 40 fibres (3) [31]. The diameter of flax fibre is about 10 µm to 30 µm [30]. The elementary flax fibre, as better shown in Fig. 1.4, is composed by concentric layers: the outer layer, the primary cell wall coats the thicker secondary cell wall, which encloses a hole in the centre, the lumen. Each layer is composed of microfibrils of cellulose which form an angle with the fibre direction. Better flax fibre mechanical properties are reached for smaller angle between microfibrils and fibre directions [33].

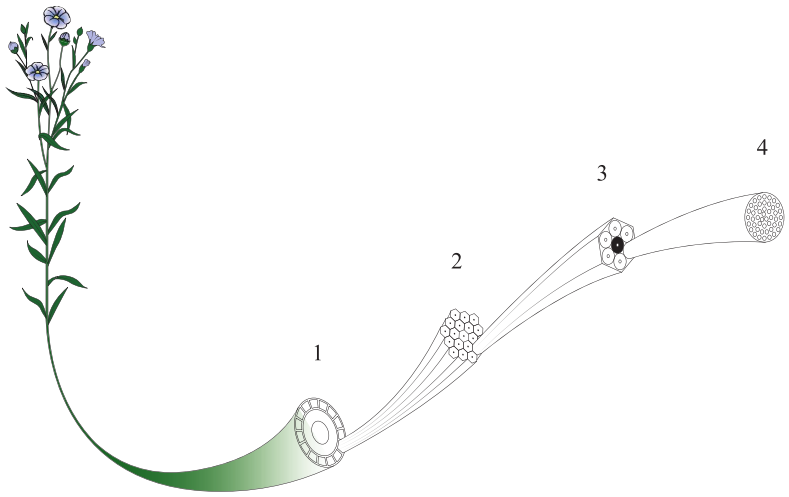

Fig. 1.3. Structure of flax fibre, from the stem to the microfibril. (1) stem, (2) bundles of fibres, (3) fibre. The fibre is composed of three concentric layers: the primary cell wall coats the thicker secondary cell wall which encloses the lumen (in black). Each of these layers is composed of microfibrils (4) [32].

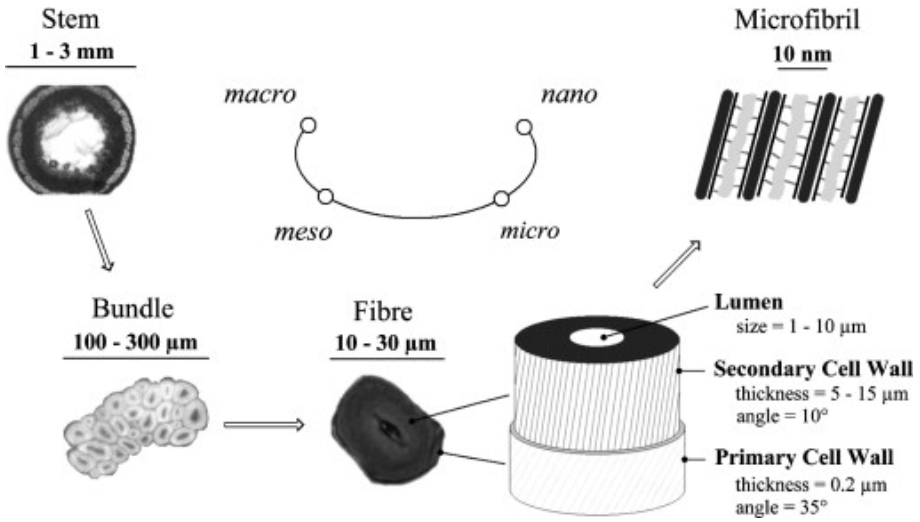

Fig. 1.4. Elementary flax fibre [30].

Fibre mechanical properties are generally identified by tensile tests on elementary fibres [34, 35]. The stress-strain curve is strongly influenced by the rate of loading, moisture content, specimen length and the extent of mechanical preconditioning [36]. Regardless of the influence of any of these parameters, the resulting stress-strain curve for flax fibres is usually of the type TIII represented in Fig. 1.5, and characterized by 3 sections [37, 38]:

1. the first linear portion of the curve corresponding to the beginning of the fibre loading;
2. a curved section characteristic of the elasto-visco-plastic deformation of the amorphous fibre parts and of the alignment of the microfibrils to the fibre axis;
3. a third linear portion associated to the elastic deformation of the microfibrils.

Young's modulus of fibres is generally calculated from the slope measured in the last stress-strain curve section [36, 39]. An average Young modulus of 54 GPa ($\pm$ 15 GPa) is determined in [36]. Such a large spread of values is mainly due to the approximation of the fibre cross section, from its geometrical characteristics to the presence of the lumen. The tensile properties of 50 batches of French flax fibres cultivated between 1993 and 2011, are calculated and compared obtaining an average Young modulus of 52.5 GPa ($\pm$ 8.6 GPa) [40]. Nevertheless, Young's modulus and

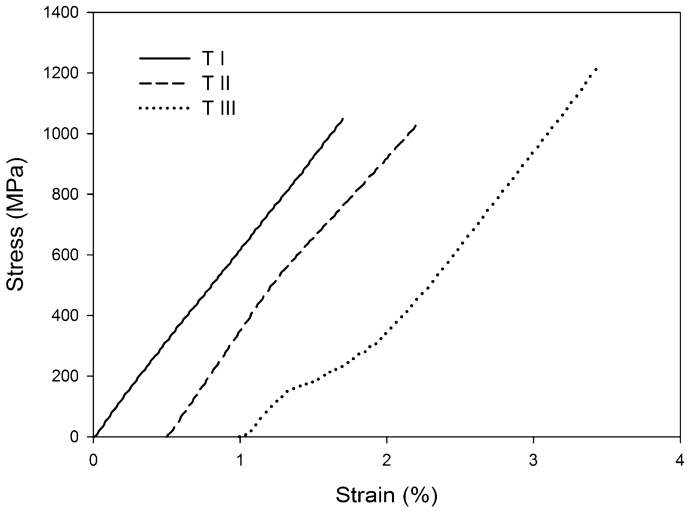

Fig. 1.5. Stress-strain curves: TI (solid line), TII (dashed line) and TIII (dotted line) behaviours [38].

strength at break suffer an important deterioration when the fibres are subjected to a thermal cycle [41, 42]. Therefore, to avoid exposing the fibres to high temperature during the manufacturing process, an accurate selection of the polymer is required.

1.2.2 Polyamide 11

Polyamide 11 is a thermoplastic polymer fully derived from renewable sources, synthesized for the first time during the Second World War and industrially manufactured since 1947 [43]. Being bio-sourced and having good mechanical properties, it is very attractive for industrial applications as environmentally friendly polymer. Further key properties are: low density, low moisture pick up, temperature resistance, chemical stability, ageing resistance. These features make this polymer suitable for a wide range of applications, in automotive industry for fuel lines, fluid transfer lines, friction parts, quick connectors; in electrical cable industry for optical cable sheathing, connectors, fasteners and clips; in oil and gas industry for flexible liners for offshore and on-shore applications, gas pipes and fittings; in sports for racket eyelets and bumpers, ski top layers, shoes soles; in medical equipment and food packaging [44].

PA11 is synthesized starting from castor oil extracted from the castor plant (Ricinus communis L.), a plant widely cultivated in India, China and Brazil. The castor oil is constituted by 85% of ricinoleic acid which is subjected to a pyrolysis process to obtain the undecylenic acid [43]. The hydrolysis of the undecylenic acid and the subsequent hydrobromination produce the 11-bromoundecanoic acid, which is treated in order to replace the Bromine atom with an amine $-NH_2$ and obtain the 11-aminoundecanoic acid, which chemical formula is $H_2N(CH_2)_{10}COOH$. The 11-aminoundecanoic acid is the monomer precursor to PA11. Indeed, its polymerization (Fig. 1.6) carried out in the presence of nitrogen at a temperature between 250 °C and 280 °C, leads to PA11, which molecule has the chemical formula $[-C=O-(CH_2)_{10}-NH-]$, cf. Fig. 1.7 [45]. Despite its renewable source, the abovementioned transformations make PA11 a non-biodegradable polymer.

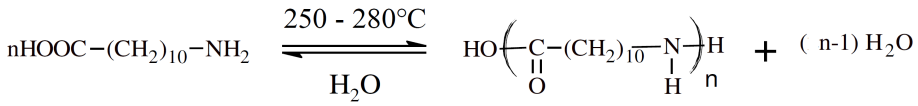

Fig. 1.6. PA11 polymerization reaction [45].

The PA11 mechanical properties are reported in Table 1.1 [44]. Though the mechanical properties of other polyamides such as PA6-10, PA6, PA6-6, PA4-6 or of the polylactic acid (PLA) are better than those of PA11, as can be seen in Table 1.2 [46], this latter remains more suitable to be used as matrix for natural fibre reinforced composites because of its low melting temperature.

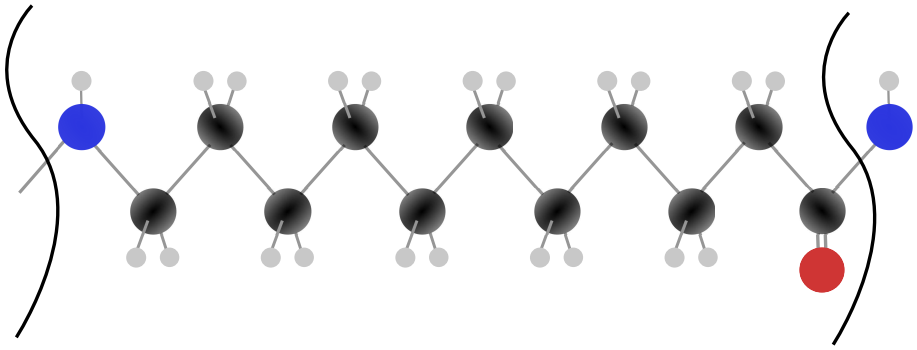

Fig. 1.7. 3D representation of a molecule of PA11: carbon atom (C) is represented in black, Oxygen (O) in red, Nitrogen (N) in blue and Hydrogen (H) in gray.

Property	PA11
Young's modulus [GPa]	1.1
Stress at break [MPa]	61
Strain at break [%]	>200
Density ρ [kg m^{-3}]	1020

Table 1.1: PA11 properties [44].

Indeed, together with the Polyamide 12, PA11 is one of the polyamides with the lowest melting

Property	PA6-10	PA6	PA6-6	PA4-6	PLA
Young's modulus [GPa]	1.5	1.2	1.8	3.3	3.4
Stress at break [MPa]	40-60	80	85	100	75
Strain at break [%]	140	50	45	30	2.4

Table 1.2: Polyamides and PLA mechanical properties [46].

temperature [47, 48]. Actually, the PA11 melting temperature measured by a Dynamic Scanning Calorimetry (DSC) lies between 186.5 °C and 191.5 °C [49, 50, 51]. By the same analysis, the glass transition temperature is obtained, resulting between 49 °C and 58 °C [46, 52, 53].

1.2.3 Manufacturing process

The film stacking and hot moulding process seems to be the most suitable manufacturing process for long fibre reinforced thermoplastics [54, 55]. Indeed, this manufacturing process presents numerous advantages: it is the least energy intensive among the manufacturing processes for long fibres and thermoplastic matrices; it leads to higher mechanical properties than those obtained by continuous melt impregnation [56]; it reduces the fibre degradation compared to injection moulding [57, 58] and a relatively high production rate can be achieved. The film stacking is usually

manual and the hot moulding process consists of the application of a time-temperature-pressure cycle on a part using a hot moulding press (Fig. 1.8). In particular, by the film stacking step, the layup is created: the long fibre fabric is cut in sheets of dimensions equal to those of the mould; then, the polymer, in the form of powder or films, is alternately stacked with fibre layers according to the desired weight fibre content. During the hot moulding process, the matrix is melted and, with the aid of pressure, it flows through the fibres.

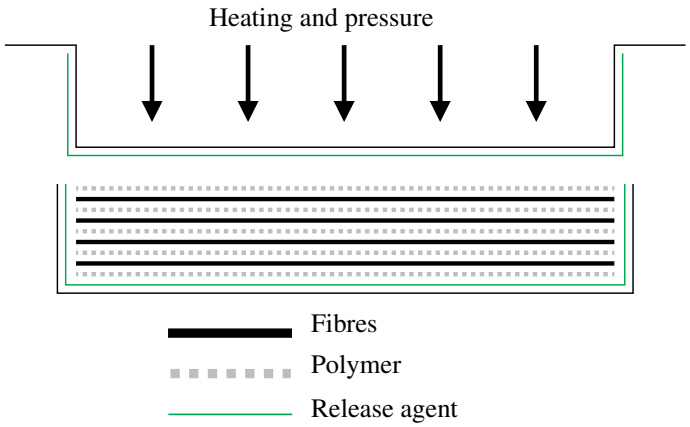

Fig. 1.8. Scheme of film stacking and hot moulding process.

Pressure, temperature and holding time are crucial parameters to take into account. Indeed, subjecting flax fibres to temperatures above 200 °C for more than 5 min leads to a decrease of the composite mechanical properties [53]. Otherwise, an increasing temperature leads to a better fibre impregnation and a higher fibre/matrix interphase quality [59]. The pressure has also a direct impact on the composite mechanical properties. Indeed, an increasing pressure allows a better fibre and matrix cohesion and a reduction of porosity [60, 52]. Both these effects lead to an increase of the mechanical properties. Several time-temperature-pressure parameter combinations for flax fibre reinforced PA11 (FF/PA11) manufacturing could be find in literature. Indeed, Destaing [53] keeps a constant pressure (varied between the values of 2 MPa, 3 MPa, 4 MPa, 6 MPa and 8 MPa) for the entire duration of the cycle while temperature increases continuously from room temperature up to the desired temperature (chosen between 190 °C, 200 °C and 210 °C), a holding phase of a duration of 1 min and a final cooling phase down to the demoulding temperature of 40 °C. Bourmaud et al. [41] and Le Duigou et al. [61] put raw materials in mould only once this latter reaches the temperature of 210 °C. After 2 min without any load application, the pressure is applied by 3 successive steps of 5 bar, 10 bar and 15 bar of a duration of 1 min and a fourth step up to 20 bar

held for 3 min are applied. Thus, the total holding time at 210 °C is 8 min, after which the cooling phase takes place. Lebaupin [52, 62] compares the mechanical properties of different types of flax fibre and PA11 (powder or films) subjected to different hot moulding cycle. In particular, dynamic mechanical analysis is employed to compare the fibre/matrix interphase quality. Indeed, a high storage modulus E' is a consequence of a good interfacial adhesion and bond strength between matrix resin and fibre [63, 64]. As conclusion of Lebaupin's study, the optimal cycle for flax fibre reinforced PA11 in form of film is characterized by a holding temperature time of 5 min at 210 °C during which the pressure is applied in 3 steps: an initial step of 25 bar at the beginning of the cycle of a duration of 2 min followed by a second step when pressure is increased up to 40 bar and held for further 2 min, then a last step with an increase of pressure up to 65 bar held until the end of the cycle. After 1 min of the application of the last pressure step, the cooling phase begins. Other studies confirm that a step evolution of pressure in hot moulding process leads to an improvement of the matrix/fibre interface [65].

1.2.4 Quasi-static properties of FF/PA11

In this study, only unidirectional composites are considered. As shown in Fig. 1.9, the tensile properties (Fig. 1.9(a)) as well as the specific tensile properties (Fig. 1.9(b)) of plant fibre reinforced polymers are affected by the fibre configuration, the manufacturing process and the matrix nature [66]. Moreover, it is noteworthy that the fibre configuration has an important impact on the material properties given that each configuration corresponds to a "bubble" in the charts whereas, comparing Figs. 1.9(a) and 1.9(b), it can be highlighted that the material density has only a slight impact on the shape of these bubbles. Furthermore, both thermoset and thermoplastic polymers reinforced by unidirectional fibres are characterized by higher tensile modulus and higher tensile strength in fibre direction.

In order to estimate Young's modulus in the fibre direction for the unidirectional FF/PA11, the theoretical mixing rule, described by the Eq. 1.1, can be applied.

$$E_1^{th} = E_1^f V_f + (1 - V_f) E^m \tag{1.1}$$

$$E_2^{th} = \left(\frac{Vf}{E_1^f} + \frac{1 - V_f}{E^m} \right)^{-1} \tag{1.2}$$

where E_1^f and E^m are respectively the longitudinal Young modulus of the fibre and the Young modulus of the matrix respectively and V_f is the fibre volume ratio. Considering a longitudinal Young modulus of the fibres between 44 GPa and 61 GPa [40], a Young modulus of matrix of 1.1 GPa and a fibre volume ratio of 42 %, the mixing rule leads to a composite Young's modulus in fibre direction between 19 GPa and 26 GPa and a Young modulus in transverse direction equal to 1.9 GPa. It is important to remark that these values are obtained considering Young's moduli of elementary flax fibre and that these latter are sensibly averaged and the deflection reduced once the fibre is inserted in the fabric.

Studies on unidirectional flax fibre reinforced polyamide 11 with a fibre volume ratio between 10 % and 70.3 % are available in literature. Such high volume ratios are possible for unidirectional fabric whereas for the composite with a random fibre orientation, the maximum value is much lower [67]. As shown in Fig. 1.10, an upward trend of the stress at break and Young's modulus with the fibre volume ratio is found for unidirectional FF/PA11 [41]. These results are in line with literature data on other flax fibre composites (Fig. 1.11) [41]. The resulting Young modulus values available in literature for a fibre volume ratio of about 41 % (corresponding to a fibre mass ratio M_f of about 50 %) are resumed in Table 1.3. It is important to note that these values are obtained on specimens constituted of non-identical unidirectional flax fabric, with different suppliers and fabric configurations, different types of PA11 (film or powder) and manufactured employing different hot moulding cycles. These differences could explain the spread of the Young moduli reported.

V_f (%)	M_f (%)	E (GPa)	Ref.
41	51	22.9±1.5	[46]
-	50	35	[52]
40.17	-	30.67±1.03	[53]

Table 1.3: Literature results on Young's modulus of unidirectional FF/PA11.

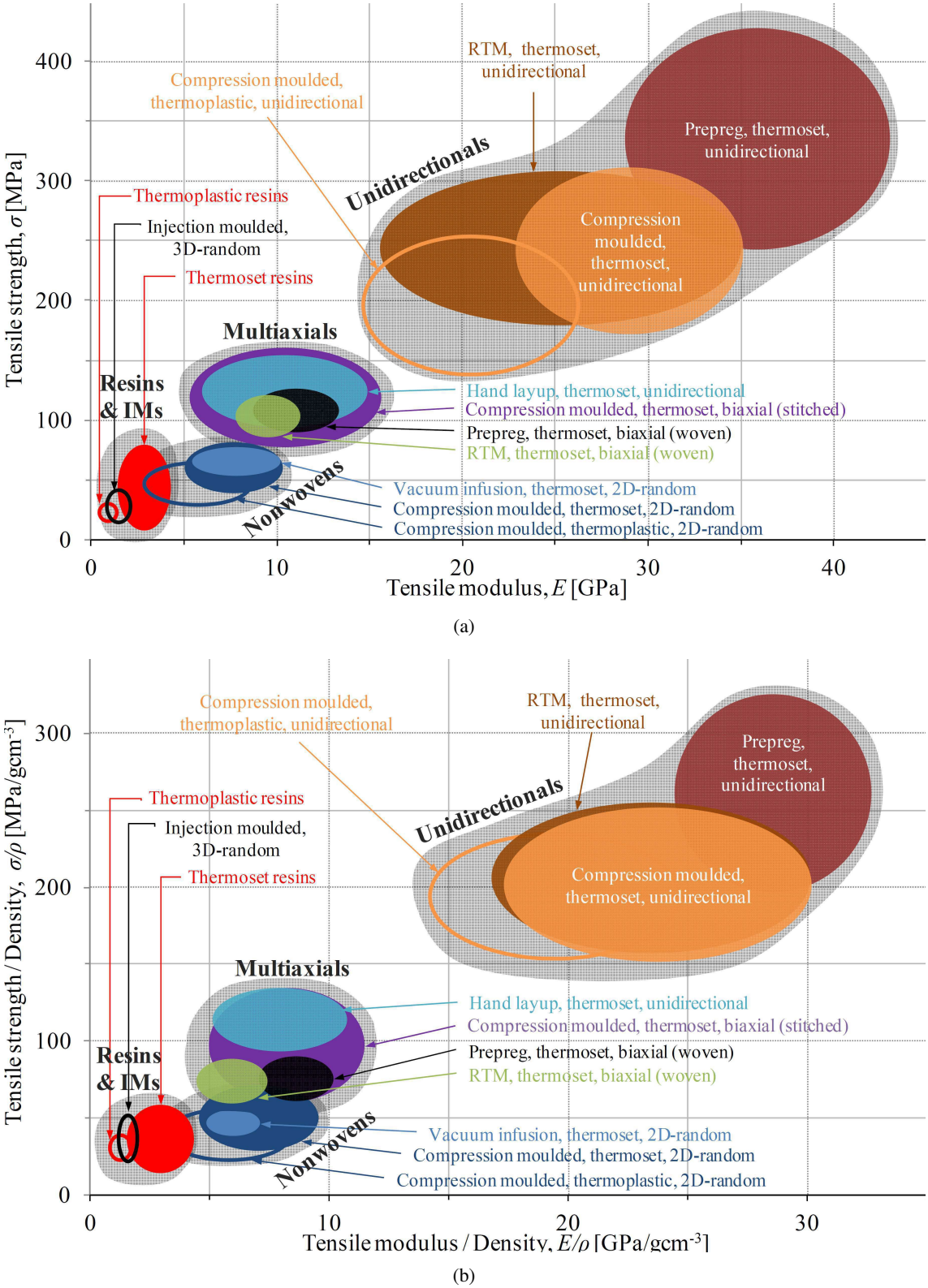

Fig. 1.9. Comparison of tensile properties (a) and specific tensile properties (b) for plant fibre reinforced polymers (random oriented, unidirectional or multi-axial) [66].

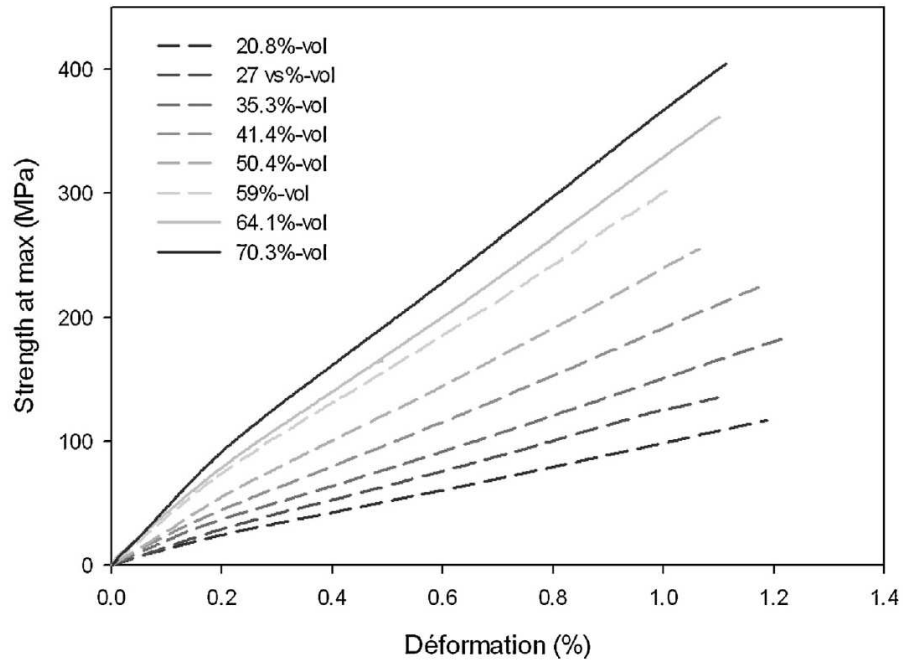

Fig. 1.10. Tensile stress-strain curves for FF/PA11 with fibre volume content between 20.8 % and 70.3 % [41].

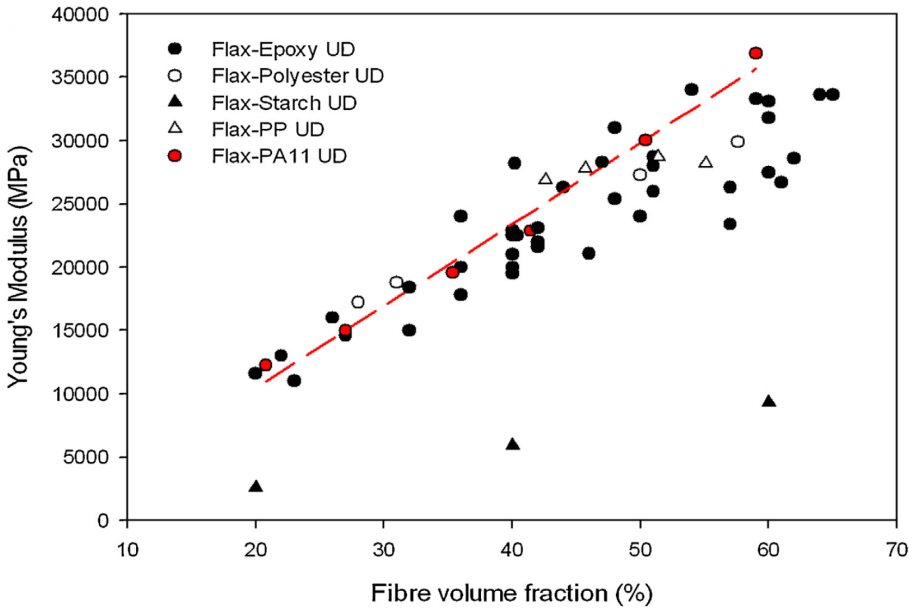

Fig. 1.11. Young's modulus of FF/PA11 and literature data against the fibre volume ratio. Linear regression for FF/PA11 in red line [41].

1.2.5 Visco-elastic behaviour

Fibre reinforced polymers generally present a visco-elastic behaviour. Visco-elastic solids are characterized by [68]:

- an increase of the strain with time when a constant stress is applied (creep)
- a decrease of the stress with time when a constant strain is applied (stress relaxation)
- an out-of-phase trend between stress and strain when a sinusoidal stress or strain is applied. The phase angle between strain and stress is usually denoted by δ.

In the visco-elasticity theory, the classical linear elastic theoretical Young modulus (E) is replaced by the so-called complex modulus (E^*) expressed by:

$$E^* = E' + jE'' \tag{1.3}$$

where E' is the storage modulus representing the elastic part of strain, in phase with the applied stress, and E" is the loss modulus, representing the viscous component of the strain, out of phase with the stress and $j^2 = -1$. Moreover, the abovementioned phase angle δ can be expressed by the ratio between the loss modulus and the storage modulus. Indeed:

$$\tan\delta = \frac{E''}{E'} \tag{1.4}$$

Therefore, a commonly used relation of the complex modulus is:

$$E^* = E'(1 + j\eta) \tag{1.5}$$

where $\eta = \tan\delta$ is called the loss factor.

As it will be discussed in chapter 2, different techniques are available to characterize the material dynamic mechanical behaviour. Here, the discussion is limited to the results obtained for FF/PA11 composites. Dynamic mechanical analysis (DMA) is used by Lebaupin [52] to characterise the FF/PA11 dynamic behaviour depending on the temperature. A Q800 device is used to measure storage modulus and loss factor between $-100\,°C$ to $300\,°C$ at a frequency of $1\,Hz$. Analysis is performed for temperatures between $25\,°C$ and $100\,°C$ on several FF/PA11 specimens

obtained using different manufacturing process parameters. The resulting curves are shown in Fig. 1.12. It can be observed that a peak of loss factor occurs for all composites at about 55 °C, corresponding to the composite glass transition temperature, in other words the temperature above which the material is in a rubbery state. Moreover, it is noteworthy that the composite corresponding to blue curves has storage modulus values greater than the other ones and smaller loss factors. Such a trend indicates a higher quality of fibre/matrix interphase [63, 64].

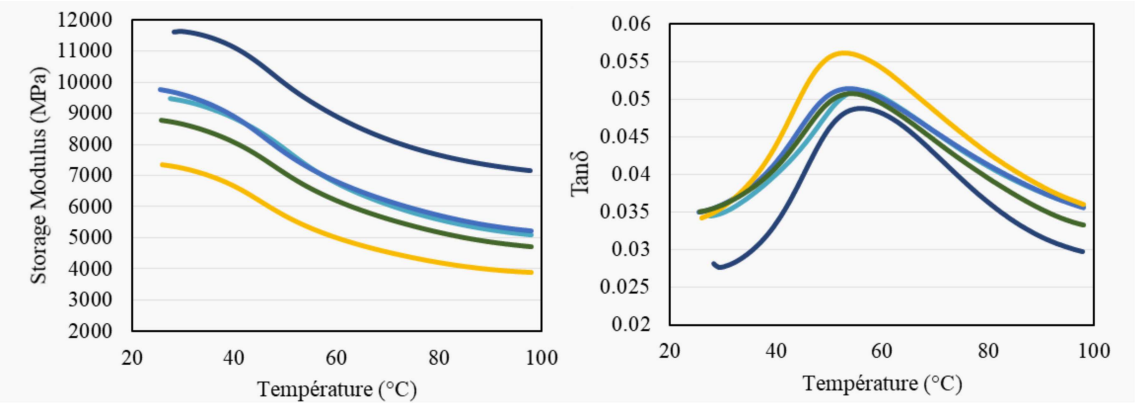

Fig. 1.12. Comparison of storage modulus (left) and loss factor (right) evolution with temperature, between FF/PA11 obtained from different manufacturing process cycles [52].

1.2.6 Impact behaviour

The properties of composite materials could be severely affected by impacts. In particular, natural fibre composites are very sensitive to impact loading [69]. Even if they are not visible, impacts can lead to a deterioration of the composite mechanical properties. Different studies are available in literature regarding the impact behaviour of natural fibre reinforced polymers [70, 71]. In particular, Jansma et al. [72] demonstrate the influence of moisture content on impact properties of a flax fibre 4×4 basket weave fabric reinforced PA11. Two different laminates having a different fibre volume ratio ($V_f = 45\,\%$ and $V_f = 59\,\%$) are analysed after being conditioned at several moisture conditions (0 %, 50 %, 95 % and 100 % of relative humidity (RH) at 23 °C). An increase of absorbed energy corresponding to higher moisture content and to higher fibre volume ratio is observed. Lebaupin et al. [52, 73] compare different staking sequences of flax fibre reinforce PA11: (1) $[0°]_8$, (2) $[0°/90°]_{2s}$, (3) $[0°_2/90°_2]_s$ and (4) $[45°/0°/-45°/90°]_s$. The ratio of the absorbed energy over the impacting one, related to the material capability to dissipate the energy, is calculated resulting of 97 % and 99 % for the first and third configurations, and substantially lower for

the others. Indeed, the specimens corresponding to the first configuration, thus the unidirectional composite, and to the third configuration, result with a more important damage. Post-impact tensile and compression tests carried out to analyse the residual mechanical properties confirm these results. Actually, the fourth configuration presents better residual properties than other configurations, showing that the presence of layers oriented at 45° leads to a better capability of the material to withstand a shock.

1.2.7 Recyclability

The interest in the natural fibre reinforced polymers lies especially in the lower environmental impact as compared to petroleum-based manufactured fibres. The main advantages are the reduction of production energy consumption and the weight reduction which results in fuel saving and emission reduction in transportation of goods [74]. Nevertheless, some studies advise against the replacement of glass fibres with natural fibres [75].

Gourier [46] investigates the possibility of long flax fibre reinforced PA11 to be recycled by grinding and injection. In particular, the evolution of the FF/PA11 mechanical properties with the number of grinding and injection cycles is observed. In order to analyse the influence of the matrix, FF reinforced PPgMA (maleic anhydride grafted polypropylene) is also studied. The FF/PA11 and FF/PPgMA composites, having an initial fibre volume ratio of 40% and 49% respectively, are divided into two parts. The first part of composites is grinded and injected obtaining a first batch of specimens called "undiluted" with the original fibre volume ratio. The second part of the composites is subjected to several grinding and injection cycles for which polymer is added in order to obtain a volume fibre ratio V_f of 21% for both FF/PA11 and FF/PPgMA. The injection temperatures are 210 °C and 190 °C for FF/PA11 and FF/PPgMA respectively. The trend of the fibre length with the number of cycles is shown in Fig. 1.13(a), whereas in Fig. 1.13(b) the Young modulus is reported for the "undiluted" specimens and for the specimens having a volume fraction of 21% . It is observed that for the FF/PA11 the length of fibres after a grinding and injection cycle drops to 145 µm ± 80 µm and it is constant at 60 µm after the third recycling process. The evolution of FF/PA11 Young's modulus follows the same trend as the fibre length. Indeed, its value decreases after the first recycling process but it remains rather stable after the third cycle. The study concludes that the recycling is a feasible solution for FF/PA11 composites.

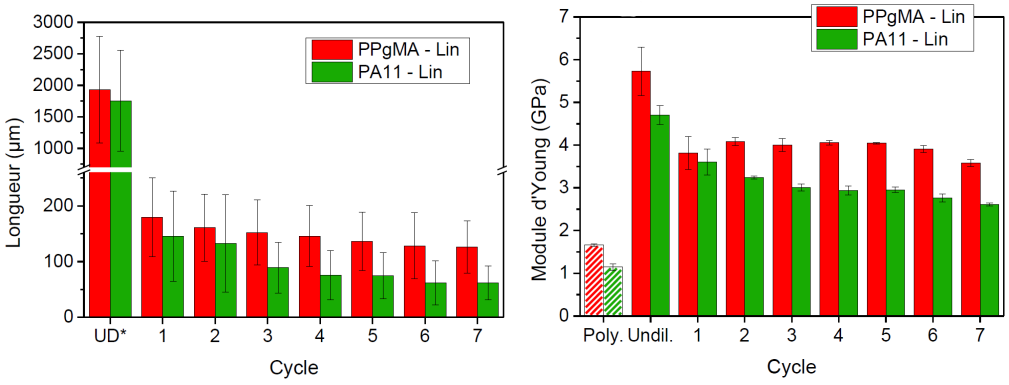

(a) Length (b) Young's modulus

Fig. 1.13. Fibre length (a) and Young's modulus (b) of recycled material, depending on grinding and injection cycles [46].

1.3 Material of this study

1.3.1 Raw materials

In the present study, the flax fibre employed for the composite manufacturing is in form of unidirectional flax fabric made of untwisted rovings (tows) of width of approximately 2 mm, fastened together with a flax weft so that no gap between adjacent rovings are presented (Fig. 1.14). The

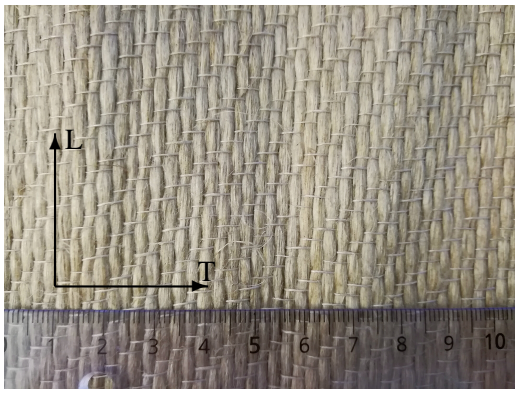

Fig. 1.14. Flax fibre fabric. The fibre (longitudinal) and transverse directions are indicated respectively with L and T vectors.

fabric, with area weight of 450 g m^{-2}, is supplied by Groupe Depestele [76] in roll of a 1 m width and 10 m length. Neither thermal nor chemical treatments are applied to fibres.

The PA11, supplied by Arkema, is used in form of film with a thickness of 100 µm and width of 0.2 m, traded under the name of Rilsan® LMFO.

1.3.2 Film stacking and hot moulding process

As already discussed in section 1.2.3, the optimal film stacking and hot moulding cycle which leads to the best fibre/matrix interphase quality is characterized by a holding temperature time of 5 min at 210 °C during which the pressure is applied in 3 steps: an initial step of 25 bar at the beginning of the cycle of a duration of 2 min followed by a second step when pressure is increased up to 40 bar and held for further 2 min, then a last step with an increase of pressure up to 65 bar held until the end of the cycle. After 1 min of the application of the last pressure step, the cooling phase begins [52]. Such a cycle, represented in Fig. 1.15 is employed for the manufacturing process of the present study. The composites realised in the present study are entirely manufactured in

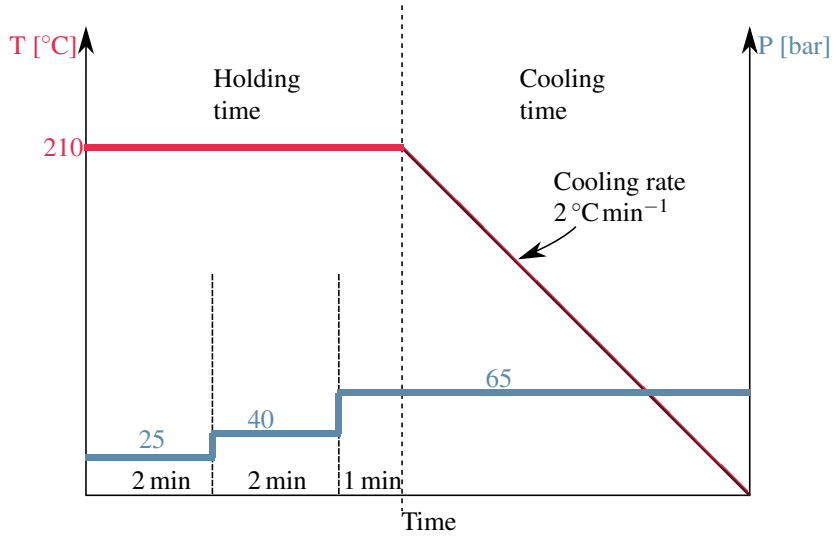

Fig. 1.15. Time-temperature-pressure cycle of film stacking and hot moulding process.

the laboratory of "Innovation Plasturgie Composites" (IPC, Laval - France). The hot moulding press employed is a Dieffennbacher with a load capacity of 1000 t. The hot moulding press can be separated in two parts: the mechanical part, responsible of the load application, which is composed by a static lower bolster and the upper slide; and a thermal part responsible of the heat transfer, consisting of a heating mould composed by the heating punch and die respectively fixed to the slide and the bolster of the press. The punch and the die are two metal plates of dimensions 460 mm × 500 mm crossed by a hot oil circuit. The oil temperature is adjusted by two temperature control units, one for each plate. The temperature control units are required to warm up the oil at the desired temperature and also for the cooling phase, using then a cold water circuit which leads to a cooling rate of about 2 °C min^{-1}. A preliminary phase of release agent application on the

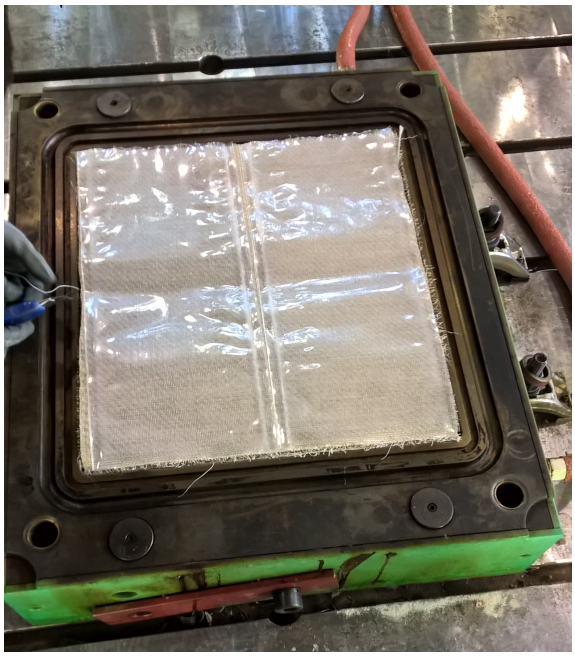

Fig. 1.16. Stacking is put into the die then the hot moulding cycle is applied. The inner die dimensions are 460 mm × 500 mm.

mould is necessary to make easier the plate demoulding at the end of the cycle. Polymer and fibre stacked layers are put into the die (Fig. 1.16) and the mould is closed for the hot moulding cycle application. A thermocouple inserted in the middle layer of the stack is employed to verify the evolution of the composite temperature during the hot moulding cycle. Actually, as shown in Fig. 1.17, a non linear trend of the temperature over the time is observed in the cooling phase. The plate is demoulded when the composite temperature reaches 140 °C, which leads to a cycle overall time of 47 min. Four flax fibre layers are alternated to five PA11 plies, weighed in such a way as to respect the weight fibre content of 50%, corresponding to a fibre volume ratio $V_f = 42\%$. A total of 10 plates of dimensions 460 mm × 500 mm are realized. The obtained plates have a mean thickness of 2.5 mm and a material density $\rho = 1220\,\mathrm{kg\,m^{-3}}$. This latter is measured on 5 specimens of dimensions 10 mm × 10 mm and thickness 2.5 mm, weighing them on a Sartorius balance characterized by a 0.01 mg resolution and calculating the ratio between their mass and volume.

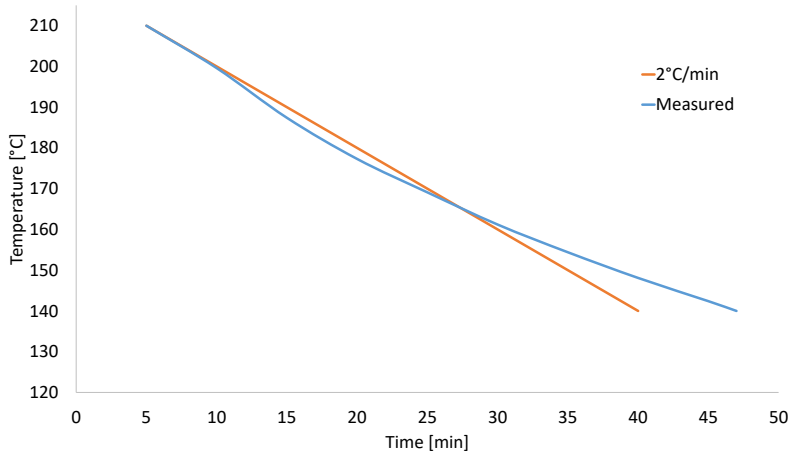

Fig. 1.17. Evolution of temperature during the cooling phase.

1.3.3 Microstructure characterization

1.3.3.1 Scanning electron microscopy

Scanning electron microscopy is often used to obtain high spatial resolution images. In this study cross section of specimens are observed in order to verify the fibre impregnation. Specimens are embedded in a resin, polished and sputter-coated with gold. Resulting images are shown in Fig. 1.18. Here, the flax tows (dark grey), the flax wefts (light grey) and the PA11 matrix (black) are clearly identifiable (Fig. 1.18(a)). Furthermore, as can be observed in Fig. 1.18(b) the material is characterized by a poor fibre individualization which can be the cause of the decrease of mechanical properties. Indeed, the presence of fibre bundle leads to a stress concentration at a microscale [77]. Thus, better mechanical properties are obtained when the fibres are separated by a layer of matrix. A similar limited fibre individualization is observed in [46], where three different samples of FF/PA11 with a fibre volume ratio of $V_f = 42\,\%$ are compared: a good individualization is obtained using flax fabric without weft (Fig. 1.19(a)) whereas tows are still well distinguished for composites using flax fabric with weft (Figs. 1.19(b) and 1.19(c)). As highlighted by the red arrows, porosity is also present in this type of composite. For the sake of clarity, composites shown in Figs. 1.19(b) and 1.19(c) are obtained using two different hot moulding cycles. The first

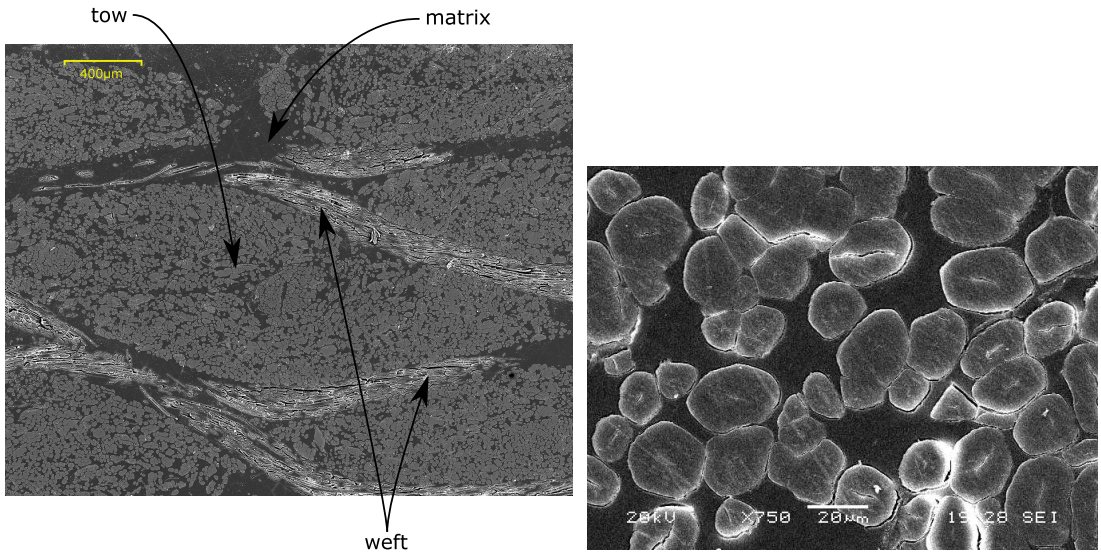

(a) (b)

Fig. 1.18. SEM observations on cross-section plane of a flax fibre reinforced PA11 plate (a) and a zoomed detail (b).

one (Fig. 1.19(b)) is characterized by a holding temperature of 210 °C kept for 8 min during which no pressure is applied for the first two minutes and then 3 successive steps of 5 bar, 10 bar and 15 bar of a duration of 1 min and a fourth step up to 20 bar held for 3 min are applied. For the second cycle (Fig. 1.19(c)) the stack is pre-heated at 210 °C for 10 min before the pressure application of 10 bar for 3 min. Comparing Fig. 1.18 and Fig. 1.19, it can be stated that the material obtained in the present study, even though characterized by a low fibre individualization, is not affected by porosity, confirming the good parameters set in the hold moulding process here employed.

1.3.3.2 X-ray tomography

In order to reach the best mechanical properties, a good fibre alignment and no-waviness are important for unidirectional composite materials [79, 80]. Therefore, it is important to verify the fibre alignment especially for a mainly manual manufacturing process as the film stacking. X-ray computed tomography is employed in the present study for this purpose. Indeed, X-ray computed tomography allows to analyse a specimen internal structure. The Phoenix v|tome| L 240 machine is used at the CRT Morlaix laboratory. A total of 18 squared specimens of dimensions 50 mm × 50 mm and thickness about 2.5 mm are cut from different locations of a plate (Fig. 1.20) in such a way to have information about the local fibre alignment over the entire plate and to estimate the

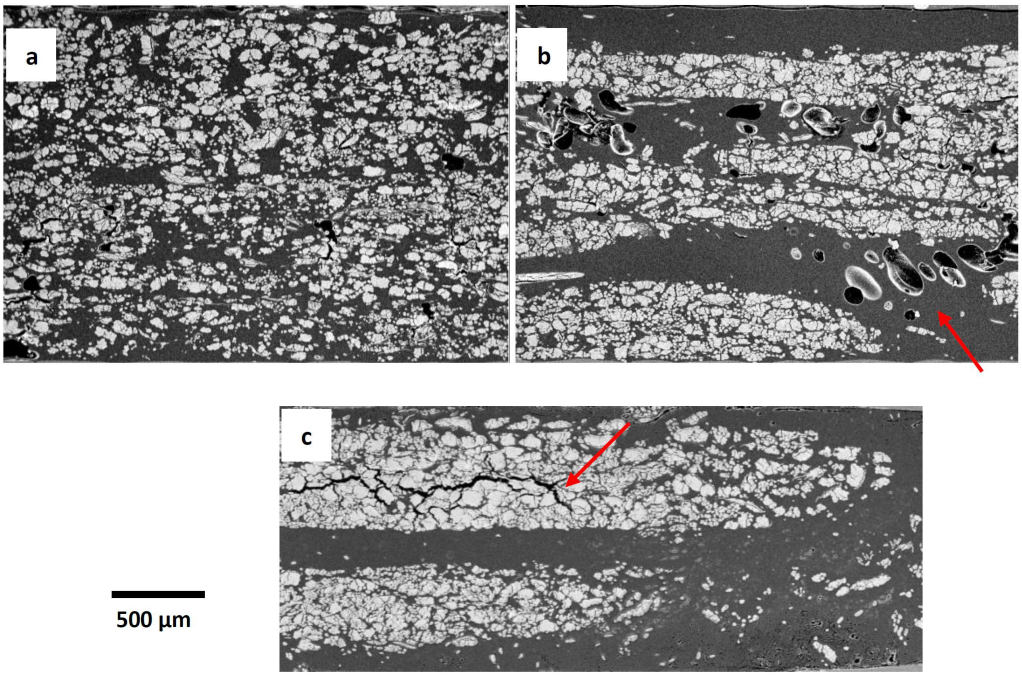

Fig. 1.19. SEM images on UD FF/PA11: (a) Flax fabric without weft, (b) flax fabric with weft obtained by a hot moulding cycle, (c) flax fabric with weft obtained by another hot moulding cycle. The red arrow highlights porosity presence within the matrix (b) and the fibre tows (c) [78].

fibre waviness. All the specimens are then stacked in two piles of 9 to be analysed together. A layer of foam with thickness about 2 mm is inserted between two adjacent specimens in order to make easier the separation in the post-treatment process. In this way two cubes are obtained, allowing to perform the tests on an optimised shape. Once the appropriate parameters for scanning are set, each cube is positioned on the rotating specimen holder and scanned. Then, the scanned images are analysed and the angle between the longitudinal direction of the plate and the fibre direction is evaluated for each specimen and for each layer of fibres, using the software myVGL distributed by Volume Graphics GmbH. In Table 1.4 the X-ray tomography observations are shown for two specimens (S1 and S2) and for each layer (L1, L2, L3 and L4). Moreover, the mean values of the fibre orientation for each layer evaluated for all specimens are reported. In particular, an overall mean value of $0.06° \pm 1.29°$ is calculated, whereas it is observed a maximum value of the angle up to 3°. These results confirm that the manufacturing process, even if strongly impacted by manual operations, does not result in a marked fibre misalignment.

Such small values of fibre orientation do not have an important effect on the tensile mechanical properties [81] nor on dynamic properties. Indeed, in order to characterize the variability in fibre

alignment and to verify its impact on the structure dynamic properties, a numerical modal analysis is performed on FF/PA11 plates to calculate the natural frequencies and the mode shapes of the first 30 vibration modes for different angle configurations. A preliminary experimental modal analysis is performed to validate the numerical model. For this purpose, a suspended plate is excited on several locations by using an impact hammer and the acceleration signals are recorded by an accelerometer glued in a point of the plate. The acceleration signals are then evaluated in the frequency domain and allow to calculate the first three natural frequencies and mode shapes over a frequency range up to 600 Hz. The correlation between the results of experimental modal analysis and those numerically obtained for a free-free plate allows to validate the numerical model. Thus, a unidirectional configuration with orientation angle equal to 0° taken as reference, is compared with a configuration for which all layers have an orientation angle of 2.5° and two other configurations for which the orientation angle is randomly chosen among three values ($-2.5°$, 0° and 2.5°) or in a range between $-3°$ and 3°. Results, presented in Appendix A, show that there is a good correlation of the natural frequencies of the first 30 modes for all configurations which results in a deviation smaller than 5 %, confirming that such values of fibre alignment lower than 3° have not an impact on the structure dynamic behaviour.

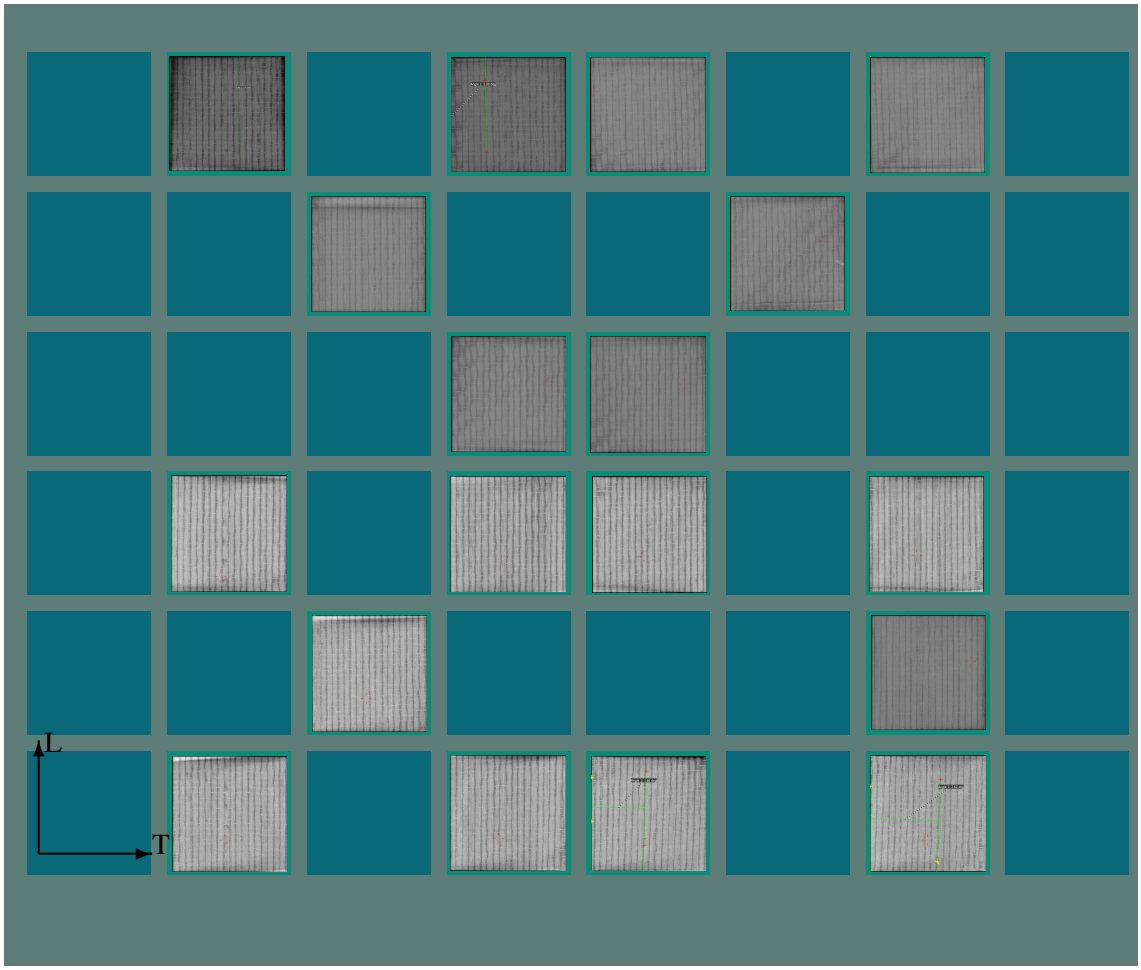

Fig. 1.20. 18 specimens of dimensions 50 mm × 50 mm cut from a plate of dimensions 460 mm × 500 mm. The longitudinal (L) and transverse (T) directions are indicated.

Layer	S1	S2	Mean misalignment value [°]
L1	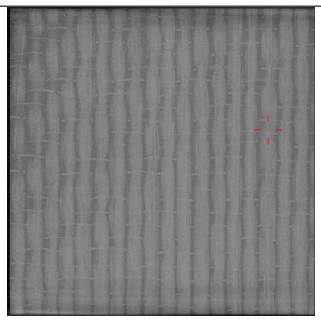	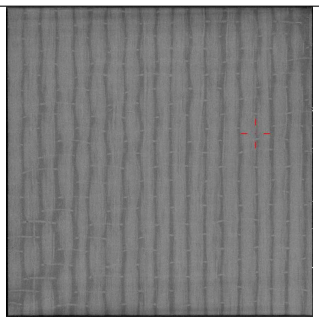	0.26 ± 0.84
L2	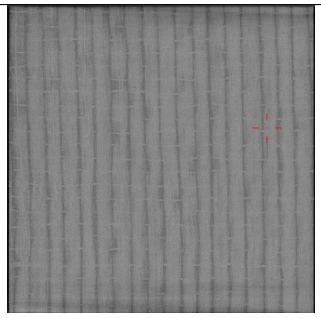	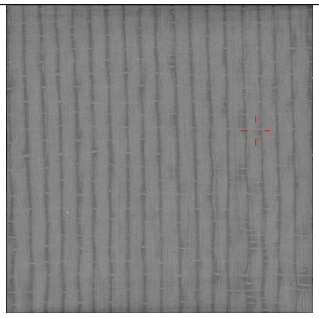	-0.95 ± 1.60
L3	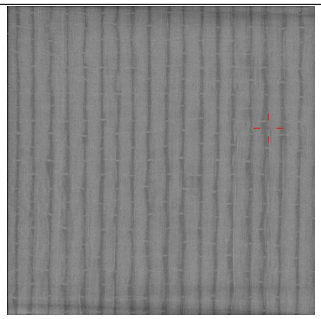	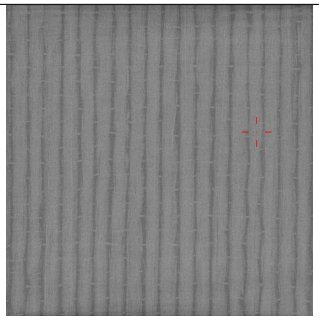	0.60 ± 1.00
L4	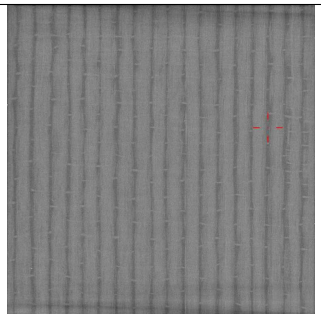	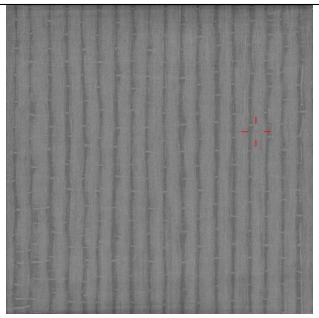	0.35 ± 1.06

Table 1.4: X-ray computed tomography observations of the four plies on two specimens and the average fibre orientation values for each ply.

1.3.4 Quasi-static mechanical behaviour

Quasi-static tensile tests are performed to identify Young's moduli and Poisson's ratios in the fibre direction and in the transverse one. Young's moduli are then compared with literature data, whereas Poisson's ratios are calculated to be used as input data for further investigations dealt with in the following chapters. Specimens in fibre and in transverse directions are obtained by cutting different plates using a numerical control milling machine. A milling cutter of 2 mm is employed with a spindle speed of 7500 rpm and a feed speed of 10 mm min^{-1}. Though the chosen dog-bone geometry, which dimensions are reported in Fig. 1.21, is specific to short fibre composites, its use is justified in the course of discussion on the obtained results. The specimens have a nominal

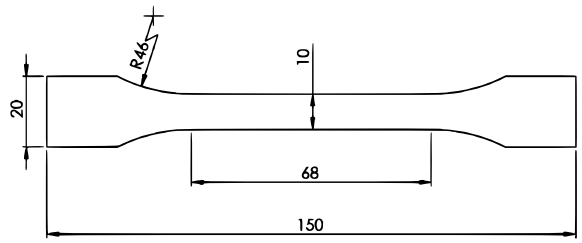

Fig. 1.21. Dog-bone specimen geometry. Dimensions are given in mm.

length of 68 mm and a nominal width of 10 mm, while thickness is measured for each specimen to verify the eventual variability of the plate thickness. Moreover, tests are also performed on rectangular specimens according to the international ISO 527-5 standards, to validate such results. The rectangular specimens, machined in longitudinal and transverse directions, have dimensions equal to 250 mm $\times$ 25 mm. A Loctite 406 glue is used to bond end tabs of dimensions 50 mm $\times$ 25 mm to the top and bottom specimen surfaces under the grips.

Tests conducted with a deformation rate around 0.01 s^{-1} at room temperature and a relative humidity of about 50 % are carried out in two laboratories: IRDL and ESTACA. In IRDL laboratory, a tensile machine INSTRON 5969 equipped with a load cell of maximum capacity 50 kN and an INSTRON extensometer with a nominal length of 25 mm allowing to measure the longitudinal strain, is used. The ESTACA laboratory, instead, is equipped with an INSTRON 3369 tensile machine, a load cell of capacity 50 kN and two INSTRON extensometers: a longitudinal one with a nominal length of 50 mm used to measure the longitudinal strain and a transverse one with a nominal length of 10 mm allowing the measure of the transverse strain, thus the Poisson's ratio. Moreover, tests are conducted in three different campaigns: dog-bone specimens are firstly tested

in June 2017 at IRDL (2017 - D) and in February 2018 at ESTACA (2018 - E) laboratories. Then, dog-bone and rectangular specimens are tested in the IRDL laboratories in February 2019 (2019 - D and 2019 - D (R) respectively).

Nominal stress σ is given by Eq. 1.6:

$$\sigma = \frac{F}{S_0} \tag{1.6}$$

where F is the load measured by the load cell and S_0 is the nominal cross section of the specimen. The longitudinal and transverse logarithmic strains are directly given in the raw output data. The resulting stress-strain curves both for longitudinal and transverse directions for the dog-bone geometry over the three testing campaigns are shown in Fig. 1.22. A comparison with literature results obtained in longitudinal direction is also reported with a dotted line (Fig. 1.22(a)). It is noteworthy that the stress-strain curves in longitudinal direction are characterized by two different sections: a first linear behaviour is observed for slight values of deformation, whilst, for strain values greater than 0.2 % a lost of linearity is detected. Poilane et al. [82] observe a similar trend for a flax fibre reinforced epoxy composite. Similar observations can be found in literature concerning plant fibre composites [41, 78, 79, 83, 84]. Such trends could be related to the natural fibre behaviour and, in particular, to the reorientation of microfibrils [83, 85, 86]. Below the inflection point, the curves related to the longitudinal direction are rather close and do not exhibit a significant dispersion between the different testing campaigns. Such a dispersion increases for larger values of strain. On the contrary, a different trend is observed in Fig. 1.22(b). Indeed, three different slopes can be observed for the three testing campaigns and, in particular, an increase of the curve slopes occurs with the time period. As for the longitudinal direction, dispersion is also present in the stress-strain curves relative to tests conducted on the transverse direction, for strain above 0.2 %. Such a dispersion is maybe due to different types of damage [52].

Although the ISO 527 standard requires the Young modulus calculation between strain values in the range 0.05 % to 0.25 %, given the presence of the inflection point, the longitudinal Young modulus is calculated on only the first section of the curve with strain values between 0.05 % and 0.15 %. The mean and standard deviation (Std) values of Young's moduli and Poisson's ratios, calculated at the beginning of the curves, in both longitudinal and transverse directions are given in Table 1.5. An increase of the Young moduli in the transverse direction of 36 % occurs between data from the first testing campaign carried out in June 2017 and those coming from the tests

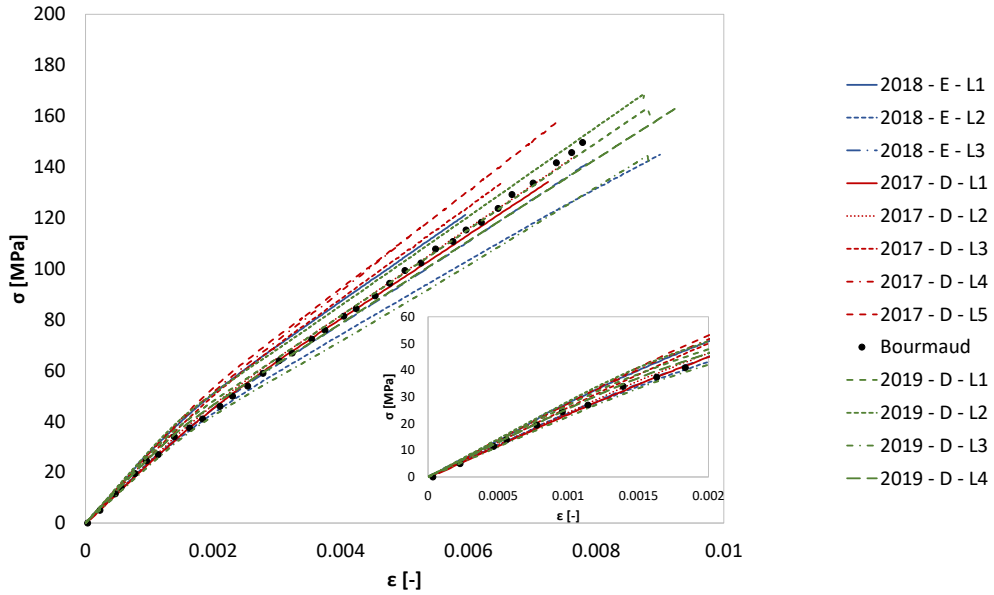

(a) Longitudinal direction.

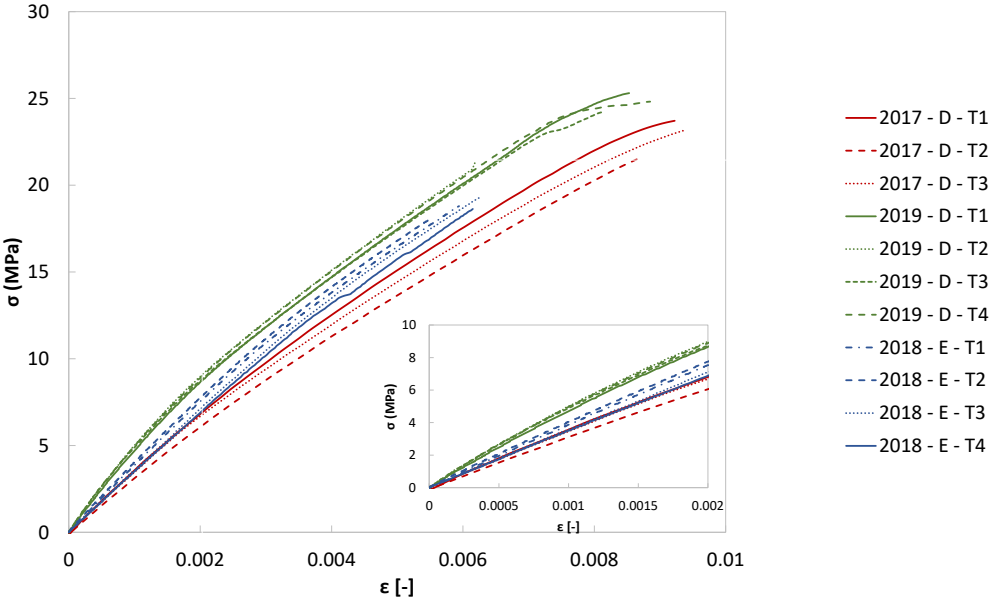

(b) Transverse direction.

Fig. 1.22. Tensile strain-stress curves for FF/PA11 UD in longitudinal (a) and transverse (b) directions for dog-bone specimens. The colour identifies different campaign of measurements whereas the dotted black curve is a literature result used for comparison [41].

conducted in February 2019. Such an increase of the Young modulus could be mainly due to the ageing phenomena occurring for the thermoplastic matrix. Actually, as it results from Eq. 1.1, for UD composites with a fibre volume ratio equal to 42 %, an increase of matrix Young's modulus of 36 % leads to a gain of the transverse composite modulus of about 38 % and a not relevant modification of the longitudinal modulus. Even though the chosen specimen geometry is not specific to

Property	Mean value (Std)
Young's Modulus E_1 [GPa]	26.6 (1.6)
Young's Modulus (2017) E_2 [GPa]	3.3 (0.24)
Young's Modulus (2018) E_2 [GPa]	3.6 (0.21)
Young's Modulus (2019) E_2 [GPa]	4.6 (0.14)
Poisson ratio ν_{12} [-]	0.41 (0.07)
Poisson ratio ν_{21} [-]	0.06 (0.03)

Table 1.5: Young's modulus and Poisson's ratio of UD flax fibre reinforced PA11 for dog-bone specimens.

the type of material in question, the results on the Young moduli are in line with others found in literature for similar fibre volume ratio [46]. The specimens geometry is then not relevant for the identification of the Young modulus. Tests conducted on rectangular specimens corresponding to the international ISO 527-2 standards related to UD fibre-reinforced thermoplastic, validate this assumption. Fig. 1.23 reports the comparison of stress-strain curves obtained by tests performed on dog-bone and rectangular specimens. The identified longitudinal Young modulus from tests performed on rectangular specimens is slightly higher than the one obtained from the dog-bone specimens, whereas the transverse Young modulus follows an opposite trend. Such a difference between the results obtained on the two geometries is, however, limited to 7 % in the longitudinal direction and 11 % in the transverse one. Nevertheless, the stress at break could be strongly impacted by the specimen geometry. Moreover, the individualization of the fibre is an important factor impacting on the composite mechanical properties and the low individualization of the flax fibres shown in section 1.3.3.1 leads to a degradation of the stress at break [87].

Stress relaxation tests are also conducted to characterize the visco-elastic composite response to a constant strain. The aim of these tests is to correlate the calculated visco-elastic material properties to those obtained by the identification method presented in chapter 2. Generally, the material visco-elastic behaviour is described by massless mechanical models composed by springs and dashpots combined in different configurations. The most used mechanical models to describe the visco-elastic behaviour of materials are Kelvin-Voigt model, composed by a spring and a

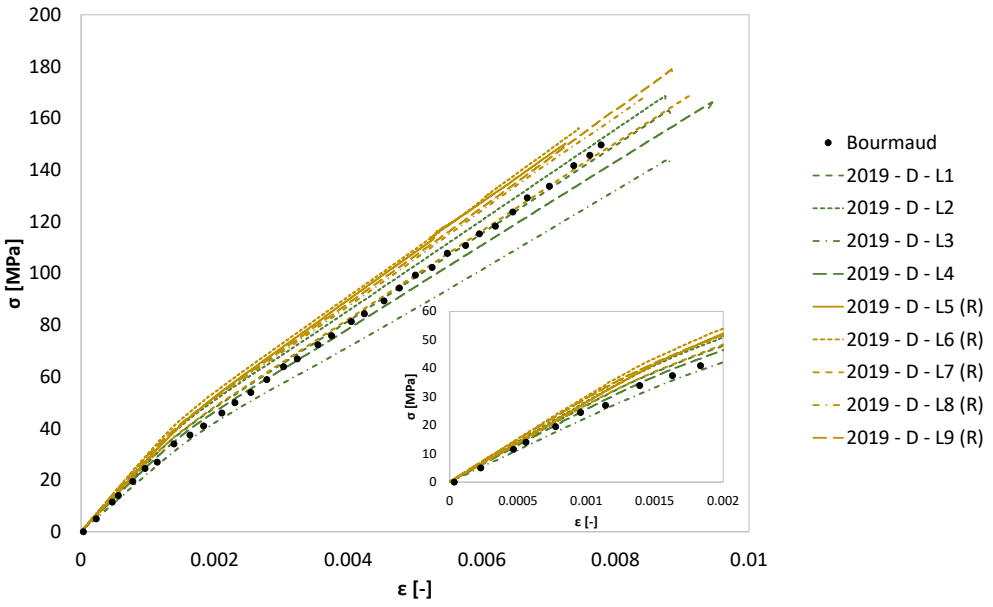

(a) Longitudinal direction.

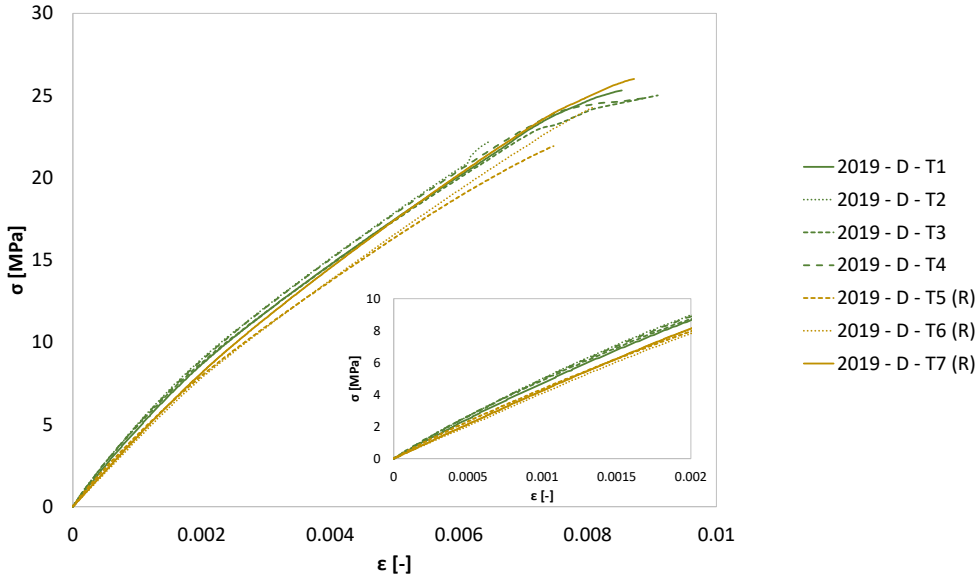

(b) Transverse direction.

Fig. 1.23. Tensile strain-stress curves for FF/PA11 UD in longitudinal (a) and transverse (b) directions for dog-bone and rectangular specimens. The dotted black curve is a literature result used for comparison [41].

dashpot in parallel, and Maxwell model, composed by a spring and a dashpot in series. In this study Maxwell model is considered. Conversely to the linear elastic material described by a linear relationship between the stress σ and the strain ε, $\sigma = E\varepsilon$ with E the Young modulus, the Maxwell equation to describe the visco-elastic behaviour results in:

$$\sigma = E_s\varepsilon_s = C_d\dot{\varepsilon_d} \tag{1.7}$$

where E_s represent the stiffness of the spring, C_d the damping of the dashpot, ε_s the strain of the spring and ε_d the strain of the dashpot. From Eq. 1.7 the expressions of ε_s and ε_d can de derived:

$$\varepsilon_s = \frac{\sigma}{E_s} \qquad \varepsilon_d = \int \frac{\sigma}{C_d} dt \tag{1.8}$$

and, since the spring and the dashpot are in series, the total strain is given by:

$$\varepsilon = \varepsilon_s + \varepsilon_d = \frac{\sigma}{E_s} + \int \frac{\sigma}{C_d} dt \Rightarrow \dot{\varepsilon} = \frac{\dot{\sigma}}{E_s} + \frac{\sigma}{C_d} \tag{1.9}$$

For a relaxation test, the strain is kept constant, which gives:

$$0 = \frac{\dot{\sigma}}{E_s} + \frac{\sigma}{C_d} \Rightarrow \sigma = \sigma_0 e^{-t/\tau_R} \tag{1.10}$$

where σ_0 is the initial stress at which the constant strain is applied and $\tau_R = C_d/E_s$ represents the relaxation time, thus the time stress takes to vanish.

The underlying idea of the experimental tests is to apply a constant strain to a specimen, measuring the trend of the stress with the time and then correlate such results with the function of stress described in Eq. 1.10 to obtain the parameters σ_0 and τ_R. A number of three dog-bone specimens obtained in fibre direction are tested following the loading and unloading cycle shown in Fig. 1.24(a). Different values of strain are applied and kept constant for 20 min. The stress measured during the cycle is shown in Fig. 1.24(b). It can be observed that the attenuation of the stress is much faster for higher value of strain. Indeed, the ratios between the initial stress and the final stress, after a 20 min relaxation, for each step of strain are 0.94, 0.86 and 0.82 respectively for applied strain values of 0.001, 0.0025 and 0.004. For a lack of time, the correlation between the Maxwell model and the experimental results is not performed in this study.

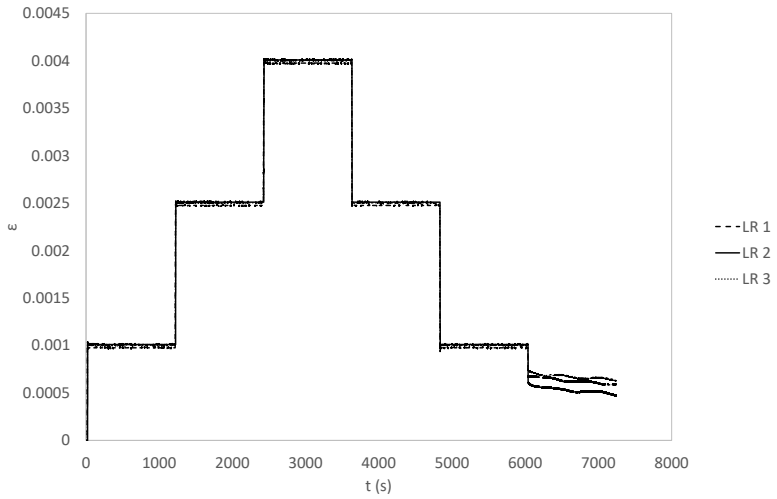

(a) Loading and unloading cycle of relaxations tests: strain is applied and kept constant for 20 min.

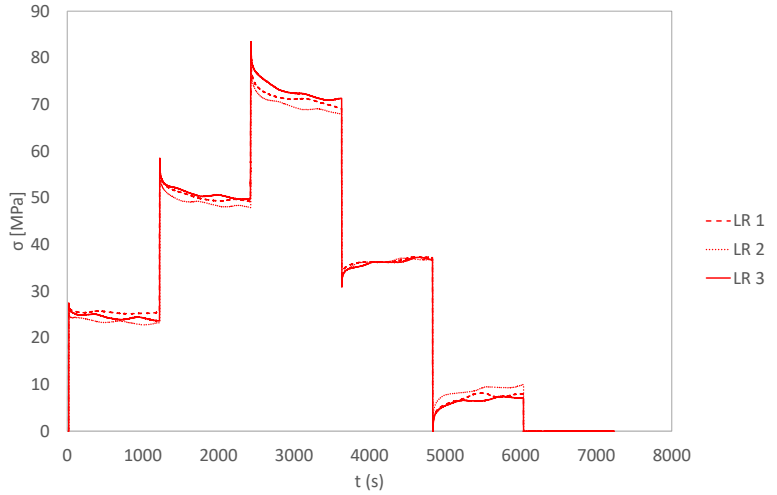

(b) Stress measurements following the application of a constant strain for 20 min.

Fig. 1.24. Stress-relaxations results.

1.3.5 Dynamic Mechanical Analysis

A Dynamic Mechanical Analysis (DMA) is also performed to characterize the visco-elastic behaviour of FF/PA11 depending on the temperature. A NETZSCH-DMA 242 machine is used to characterize the storage modulus and loss factors trend over a range of temperature going from 10 °C to 100 °C. Two specimens, machined in fibre direction and in the perpendicular one, having dimensions 50 mm × 10 mm × 2.5 mm, are tested in a 3-points bending configuration and a dynamic force of 9.2 N applied at 1 Hz. The resulting curves of storage modulus and loss factor for each of the two specimens are presented in Fig. 1.25. As can be seen in Fig. 1.25(a), the glass

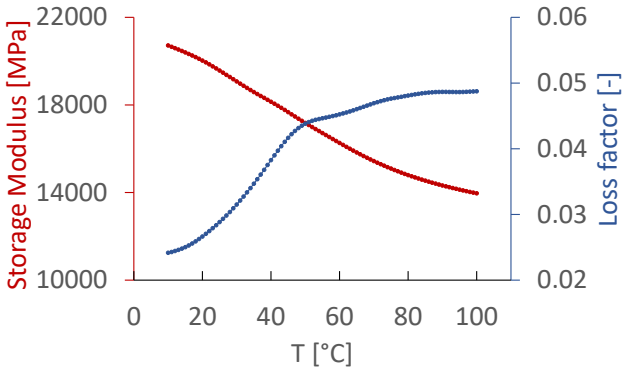

(a) Longitudinal direction

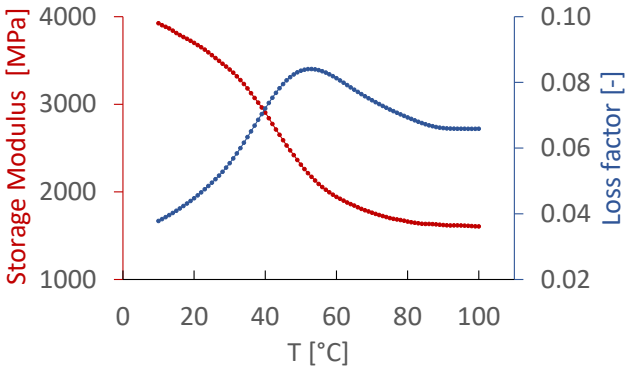

(b) Transverse direction

Fig. 1.25. DMA results on longitudinal and transverse directions (f = 1 Hz).

transition region is not clearly identified from the test carried out on the specimen cut in the fibre direction. Indeed, the storage modulus curve is characterized by a decreasing trend quite constant over the range of frequencies, with values going between 21 MPa to 13 MPa. The absence of the sharp drop in storage modulus characteristic of the glass transition in the polymers, is already

observed in previous works on FF-thermoplastic polymers [19]. Moreover, the loss factor does not present any peak over the analysed temperature range and assumes values between 0.02 and 0.05. On the contrary, the curve related to the specimen machined in transverse direction present a noticeable drop of the storage modulus and a peak of the loss factor which allow to detect a glass transition temperature at 52 °C, in agreement with previous results [52].

1.4 Conclusions

This chapter is dedicated to the description of the material used in the present study. Firstly, an introduction to flax fibres has been addressed. The process to obtain the flax fibre fabric is described from the sowing of seeds up to the spinning process. Moreover, a microscale structure of the flax fibre is presented, to better understand its mechanical properties. Secondly, the polyamide 11 and it synthesizing process are described. Though the PA11 mechanical properties are lower than those of other polyamides, it has the lowest melting temperature which makes it suitable to be used as matrix for natural fibre reinforced composites.

The manufacturing process generally chosen for UD flax fibre reinforced PA11 is the film stacking and hot moulding process. Thus, a bibliography study on the role of pressure, temperature and holding time is addressed: an optimized cycle leads to a good fibre/matrix interphase quality. Furthermore, literature results on quasi-static tests obtained on different fibre volume ratios, flax fabric configurations and manufacturing process are presented with Young's modulus values found between 22.9 GPa and 35 GPa. Moreover, some results on the dynamic mechanical analysis to characterize the material visco-elastic behaviour are presented. These results are used to verify the best fibre/matrix interphase quality. For the sake of completeness, the bibliography review includes some results on the impact behaviour and the recyclability of FF/PA11.

In the second part of this chapter, the raw materials employed in this study are presented as well as the manufacturing process. A number of 10 plates of dimensions 460 mm $\times$ 500 mm with a mean thickness of 2.5 mm are manufactured. The microstructure is observed by Scanning Electron Microscopy (SEM) and X-ray tomography. Observations carried out by SEM confirm a good impregnation of fibre and the absence of porosity. Nevertheless, the configuration of the flax fabric leads to a poor fibre individualization, which often results in a reduction of the mechanical properties. X-ray tomography confirms that the fibres are not affected by a significant misalignment. Indeed, an overall mean value of fibre orientation is of 0.06°. Quasi-static tensile tests are carried out on dog-bone specimens over three different testing campaigns in fibre and transverse directions to obtain Young's moduli and Poisson's ratios. When compared with the literature results, the obtained properties in the longitudinal direction are in agreement, with a Young modulus in the fibre direction of 26.6 GPa. However, an increase of the Young modulus in transverse direction is observed after one or two years. Indeed, transverse Young's modulus goes from 3.3 GPa to 4.6 GPa,

which corresponds to a variation of 36 % from results obtained in June of 2017 to those obtained in February of 2019. Such a variation could be related to ageing phenomena of the thermoplastic matrix. A comparison between results obtained from dog-bone specimens and rectangular ones meeting the international ISO standards for the UD fibre reinforced thermoplastic polymers, confirms that the geometry has not an important impact on Young's moduli calculation. Relaxations tests are also carried out in order to characterize the material visco-elastic behaviour. The aim of these tests is the correlation of the experimental results with the parameters of a Maxwell model. For a lack of time, such a correlation is not completed so far. Finally, DMA analysis are performed on two specimens cut in fibre and perpendicular directions. Such an analysis, performed between 10 °C and 100 °C, allows to detect a glass transition temperature of the material at 52 °C, in line with previous works available in literature. Moreover, a loss factor between 0.02 and 0.05 is also measured.

To the knowledge of the author, no previous study has been carried out on the FF/PA11 dynamic mechanical behaviour on a wide range of frequencies. For this reason, the next chapters are addressed to this topic.

2

Dynamic property identification method based on FAT: general presentation and validation

Contents

2.1 Introduction

The aim of this chapter is to give a general presentation of the dynamic property identification method and to apply it for the characterization of FF/PA11 plate. This method, inspired from the Force Analysis Technique, is based on the local equation of motion of a plate which provides a relationship between the displacement field and the material mechanical properties. These properties are calculated using the out-of-plane displacement field measured on a suspended vibrating plate together with the plate thickness, material density and Poisson's ratios. After a bibliography review on the results obtained by the method, the fundamental steps accomplished in the experimental measurement and calculating process are analysed in this chapter. A measurement technique based on digital image correlation is firstly applied to measure the displacement field of a vibrating plate. Two types of excitation signal are used: a slow and a fast sinusoidal chirps. As in both cases the measurement noise leads to highly dispersed results, another measurement technique, i.e. the laser Doppler vibrometer, is used. Such a technique is firstly validated on a transversely orthotropic plate, then applied to the material of interest of this PhD work presented in chapter 1. In order to characterize the dispersion related to the material, results obtained over 3 different plates are compared. Additional dynamic mechanical analysis tests are conducted to compare the results of the two methods [88]. A good correlation is obtained for the longitudinal storage modulus and for the loss factors.

2.2 Force Analysis Technique: a bibliography review

One of the first choices of car designers to reduce the vehicle mass is the use of composite materials, such as carbon, glass or natural fibre reinforced polymers. Indeed, such materials have very good specific properties, making them a particularly attractive solution in the lightning process, compared to metallic alloys. Moreover, these materials are often characterized by a frequency-dependent visco-elastic behaviour with a higher damping factor than metallic materials, which makes them interesting for applications subjected to dynamic loading. However the dynamic behaviour depends on the type of polymer and fibres: thermoplastic polymers present higher damping properties then thermoset ones [89]. The same trend is observed for flax fibre reinforced polymers, compared to the same matrix reinforced with carbon fibre [19], with a ratio around 2 or 3 for epoxy matrix [90]. However, dynamic properties in composite materials are not only influ-

enced by the nature of both matrix and fibres [91], but also by the fibre/matrix interface [92, 93] and/or damage. The characterisation of the dynamic mechanical properties over a large frequency domain is then important to ensure the reliability, performance or acoustic comfort and to obtain accurate results in simulation e.g. in finite element analysis.

The significant characteristics used to describe the material dynamic behaviour are the real and imaginary parts of the dynamic complex modulus E^* (see section 1.2.5). In particular, the ratio of the loss factor and the storage modulus describes the material energy dissipation or the material damping. Many ways are available to calculate the complex modulus. For non-resonance techniques, such as the dynamic mechanical analysis (DMA) [94], the specimens are excited in frequency by the application of a sinusoidal stress or strain and the specimen response is analysed. For visco-elastic materials, the response is characterized by a shifting phase angle with respect to the applied stress or strain. The in-phase and out-of-phase components of the response allow to calculate the storage modulus and the loss factor. Resonance techniques consist of exciting the specimen to obtain its frequency response function and analysing its natural vibration modes. Among these techniques, one of the most used method for the identification of material loss factor is the half-power bandwidth method [95]. Such a method is used in [96] to determine the damping ratios of a flax-epoxy composite plate. Furthermore, a method based on the resonance technique is used in [97] to characterize the visco-elastic parameters of a flax fibre reinforced epoxy laminate. The eigen-frequencies and damping ratios are extracted from the frequency response function. Then, using the equation of the tension-compression mode, the elastic modulus is calculated. A comparison of the shape memory polymer mechanical properties obtained by a resonance technique (modal analysis) with those obtained by DMA and quasi-static tensile tests is presented in [98]. Results on storage modulus and loss factors shown in Fig. 2.1 highlight a good correlation between the three methods. As it can be observed, modal analysis leads to results over a frequency range higher than the DMA. Another way to identify the material dynamic properties is the free decay technique [99] which is based on the time-dependent vibration amplitude measurement once the excitation is turned off. Recently, other methods based on the inhomogeneous wave correlation have been developed to identify dynamic structure behaviour [100, 101, 102, 103]. These methods use a correlation between the measured normal displacement fields and an analytical wavefield taking into account damped waves. Moreover, inverse methods based on the correlation between the experimental displacement fields and the results of a Finite Element Model Updating, are also

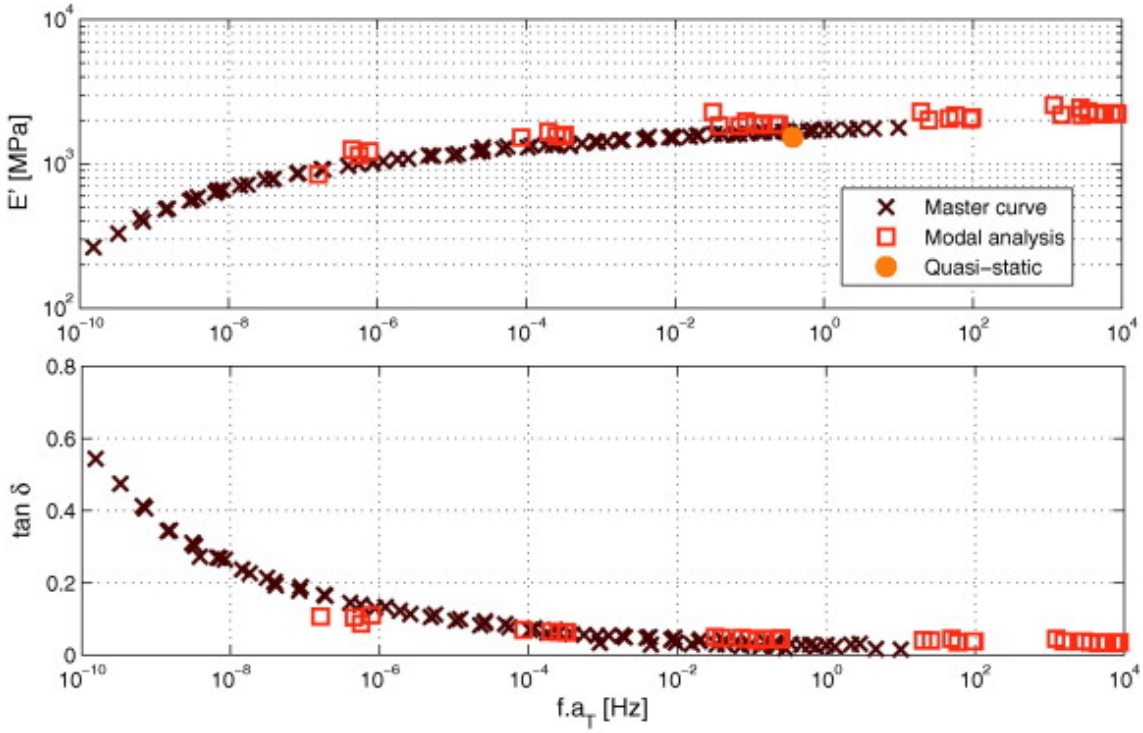

Fig. 2.1. Comparison of three experimental methods on the storage modulus and the loss factor for a temperature $T_0 = 26\,°\text{C}$ [98] .

used to identify material properties [104].

In addition to these methods, others inspired from Force Analysis Technique (FAT) are also increasingly applied. This technique has been developed to localize and identify vibration sources of a vibrating structure [105]. Such an objective allows, for example, to identify the sources of undesirable vibrations or noises, to measure a force when the use of a load cell is not possible or, moreover, to study local discontinuity or inhomogeneities that could be find in a simple structure such as a hole in a plate and to model them as a distribution of efforts. FAT aims at identifying all types of effort (concentrated, distributed or pressures..) in form of force distribution all over the structure. Based on the structure equation of motion, it makes use of a measured displacement field and to calculate any eventual applied effort. In other words, the equation of motion is discretized using the measured displacement field together with the partial derivatives being approximated by a finite difference scheme, in such a way that the only unknown of the equation is the force distribution. Even if, from a mathematical point of view, no matrix inversion occurs in the application of the method, the problem is defined *inverse* because usually, a direct problem corresponds to the determination a displacement field by the knowledge of the structure characteristics and applied

efforts. On the contrary, FAT leads to the identification of efforts knowing the structure properties and dimensions and measuring the displacement field. Moreover, since the derivative calculations lead to the amplification of the noise affecting the measured displacement, a regularization step consisting of the application of a window and a low-pass filter defined in the wavenumber domain, is usually employed [105]. One of the strengths of FAT is that, using the local equation of motion always verified in any parts of the structure, no information about the boundary conditions of the vibrating structure nor about the applied forces outside the zone of interest is required. The method, firstly developed for beams [106], is also extended to plates [107] and shells [108]. Indeed, all these structures are described by an analytical equation of motion. Other studies are carried out to apply the method to more complex shapes for which an analytical equation of motion is not available and a finite element model is needed [109]. Other developments of the FAT are addressed to overcome the difficulties involved in the application of the low-pass filter defined in the wavenumber domain. For this purpose, Leclère et al. [110] suggest to replace the filter expression by an relevant finite difference approximation of partial derivatives. Indeed, the discretization of the displacement field by the finite difference scheme constitutes itself a low-pass filter.

Several years after the first formulation of FAT, a similar approach was used to identify the dynamic properties of materials using the displacement field measured on plates [111, 112, 113, 114] and beams [114, 115]. Indeed, the structure equation of motion supplies a direct relationship between the displacement field and the material properties. While in the original formulation of FAT, the material properties are supposed known and the only unknown is the force distribution, in this case the material is to be characterized. As the local equation of motion is always verified in every zone of the vibrating structure, and in order to avoid that the force distribution constitutes another unknown in the problem, only an area of measurement far from the boundary conditions and the excitation point is considered in this approach. Therefore, substituting the displacement field and its derivatives in the discretized equation of the vibrating structure, the flexural stiffness can be calculated. From the real and imaginary part of such flexural stiffness, which are generally in form of complex values, information about the material properties are extracted. Also in this approach, the regularization step is necessary to reduce the noise of the measured displacements. Such FAT-based method is applied in [111] to identify the storage modulus and loss factor of an isotropic poly-methyl methacrylate (PMMA) plate over a range of frequencies between 16 Hz and 6400 Hz. A slight increasing trend with frequencies can be observed for storage modulus, which

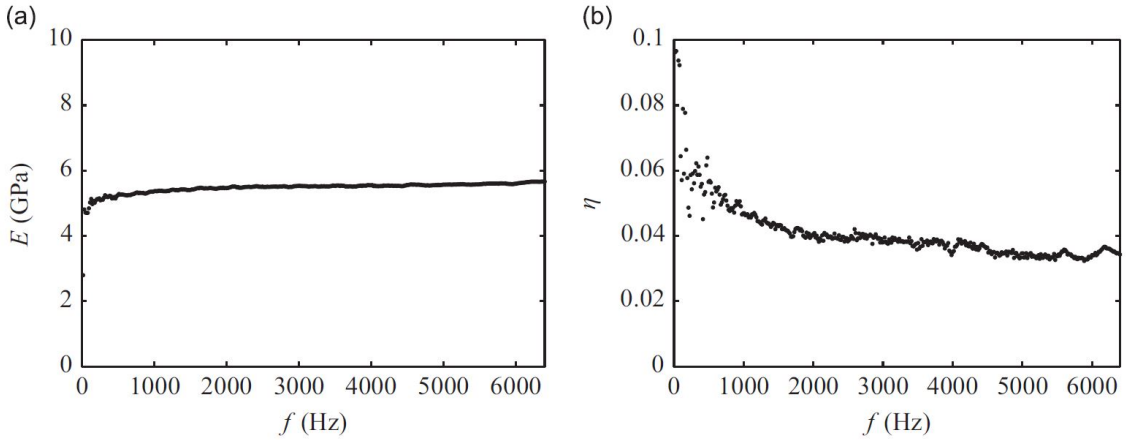

Fig. 2.2. Storage modulus (a) and loss factor (b) identified by displacement measurements of a PMMA plate [111].

assumes values of about 5 GPa at low frequencies at up to 6 GPa at high frequencies (Fig. 2.2(a)). On the contrary, a decreasing trend is observed for loss factor, which assumes values of 0.1 at low frequencies and drops with the frequency below 0.04. Moreover, in [112] a similar FAT-based method is used to identify the flexural stiffness as well as the angle between the axes of the measurement mesh and the directions of the orthotropic material. Results are obtained on an isotropic PMMA plate locally stiffened with aluminium beams as well as on a composite and bio-composite materials. Figure 2.3 presents the identified flexural stiffness calculated from the displacement fields measured on the PMMA plate over two areas, without and with stiffeners, and over a range of frequencies between 0 Hz and 5000 Hz. Concerning the area without stiffeners (Fig. 2.3(a)),

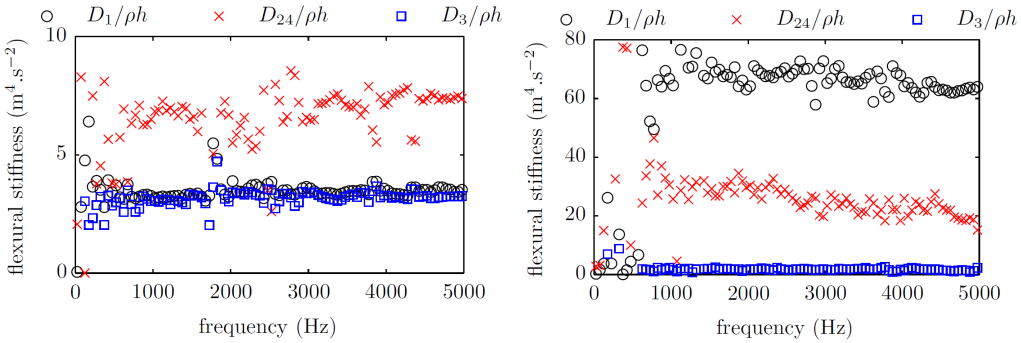

(a) Without stiffeners (b) With stiffeners

Fig. 2.3. Real part of flexural stiffness values identified by displacement measurements of a PMMA plate over an area without (a) and with stiffness (b) [112].

the identified D_1 and D_3 flexural stiffness values, directly related to the storage moduli over the

principal material directions, are identical, confirming the isotropic material behaviour. Moreover, also in this case, an increase of the flexural stiffness with the frequency is observed. The insertion of the aluminium stiffeners leads to a significant increase of the flexural stiffness D_1 as observed in Fig. 2.3(b). Nevertheless, a decreasing trend with the frequency characterizes the flexural stiffness curves. Results obtained from the displacement field measurements performed on a 8-ply unidirectional glass fibre reinforced vinyl ester composite panel are reported in Fig. 2.4. A noteworthy

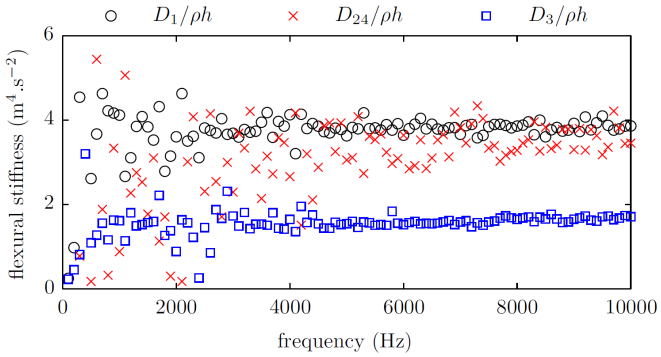

Fig. 2.4. Flexural stiffness values for a UD glass fibre reinforced vinyl ester composite panel. [112].

difference can be observed between the flexural stiffness values identified over the fibre direction D_1 and the transverse one D_3. A quite constant value of the flexural stiffness D_1 is obtained over a range of frequencies between 0 Hz and 10 000 Hz, whereas a slight increasing trend is observed in the case of D_3. Moreover, analysis between 0 Hz and 10 000 Hz are also performed on a 3-ply flax fibre reinforced composite panel. The results shown in Fig. 2.5 highlight, also in this case, a slight decreasing trend of the flexural stiffness in the fibre direction and an increase of the transverse one with the frequency. The same FAT-based method is also applied in [113] to identify the

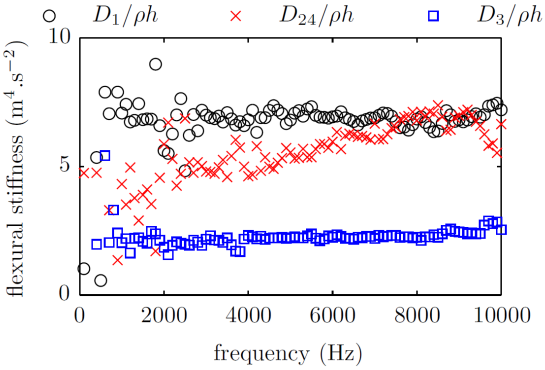

Fig. 2.5. Flexural stiffness values for a bio-composite panel. [112].

dynamic properties of a sheet moulded compound based on vinyl ester resin and reinforced with high ratio of chopped carbon fibres, over the principal directions of a rectangular plate. Results in term of storage moduli and loss factors are reported in Fig. 2.6 for frequencies going from 10 Hz to 10 000 Hz. The anisotropic material behaviour is highlighted by the two different identified values over the two directions (Fig. 2.6(a)). Indeed a value of 20.7 GPa is identified in x-direction and 42.1 GPa in y-direction. Similarly, also the loss factors present two different values on the two plate directions (Fig. 2.6(b)). In particular, loss factors are characterized by marked oscillations all over the range of frequencies. Because of the large scale chosen by the authors to represent the results, no comments can be made on the trends with the frequency neither for the storage moduli nor for the loss factors.

To summarize, results available in literature on the FAT-based method for the dynamic properties identification highlight increasing or decreasing trends of the storage moduli with the frequency. The origin of these trends is not always related to the real behaviour of the studied materials and but is often related to the abovementioned regularization step. Moreover, it is highlighted that the method does not allow to identify the loss factor when the noise affecting the displacement field measurements is high [112, 113]. Furthermore, it is noteworthy that an important dispersion generally characterizes results below 2000 Hz. Such a limitation is often associated to the limited dimensions of the observed area.

In this chapter, the application of the FAT-based method for the identification of FF/PA11 dynamic properties is presented. In section 2.3, the method is introduced. After a presentation of the local equation of motion, the partial derivative approximation scheme as well as the window and filter expressions are reported. As described in section 2.4, the digital image correlation is used in a first step as displacement measurements technique. However, the measurement noise leads to a significant dispersion of the results. Therefore, a laser Doppler vibrometer (LDV) is then employed in a second step. In section 2.5, three different experimental setups for LDV measurements are presented. A validation of the identification method is firstly conducted on a transversely orthotropic material and, subsequently, results on three FF/PA11 plates are reported. The identified storage moduli and loss factors are then compared with those obtained by dynamic mechanical analysis.

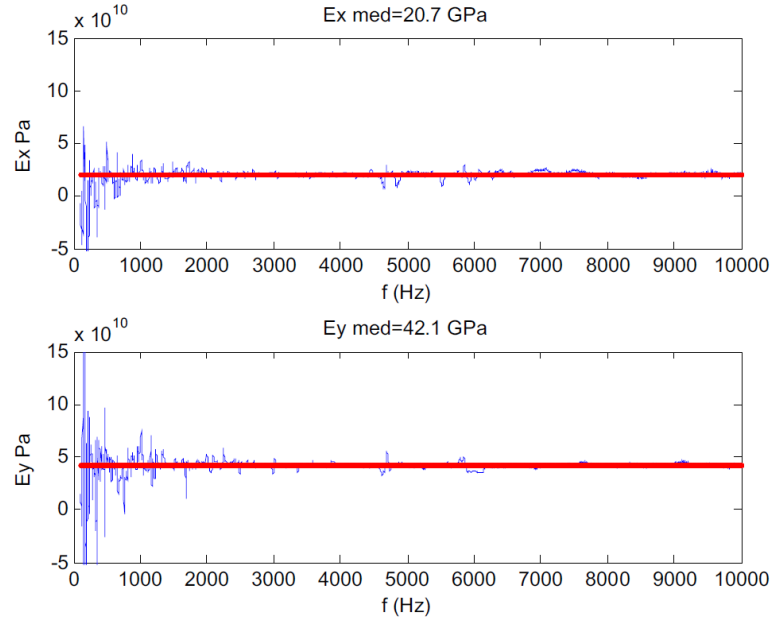

(a) Storage moduli over the principal directions of the plate

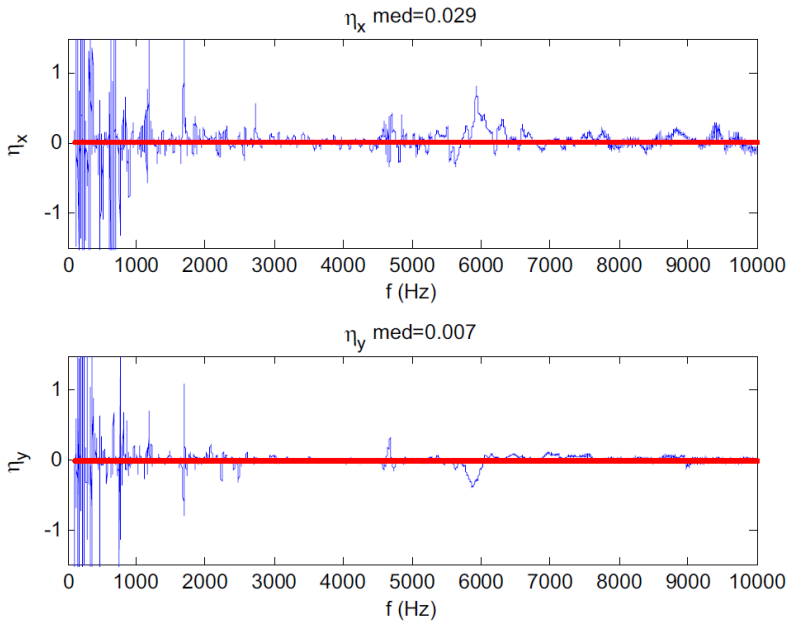

(b) Loss factors over the principal directions of the plate

Fig. 2.6. Storage moduli (a) and loss factors (b) identified by displacement measurements of a SMC plate [113].

2.3 Theory of the identification method

2.3.1 Equation of motion

The dynamic properties identification method studied in this chapter, inspired from FAT, is detailed in [111, 112]. It is based on the local equation of motion of a thin orthotropic plate in harmonic regime (Eq 2.1) [116]:

$$D_1\frac{\partial^4 w}{\partial x^4}+(D_2+D_4)\frac{\partial^4 w}{\partial x^2\partial y^2}+D_3\frac{\partial^4 w}{\partial y^4}-\rho h\omega^2 w(x,y)=p(x,y) \tag{2.1}$$

where x and y correspond to the axis of symmetry of the orthotropic plate, $p(x,y)$ represents the external force density, ω the angular frequency of excitation, h the plate thickness, ρ the material density and $w(x,y)$ the out-of-plane displacement. D_1, D_2, D_3, D_4 are the four unknown independent flexural stiffness parameters defined as:

$$\begin{aligned} D_1&=\frac{E_1'(1+j\eta_1)h^3}{12(1-\nu_{12}\nu_{21})} \quad D_2=\frac{E_2'(1+j\eta_2)\nu_{12}h^3}{6(1-\nu_{12}\nu_{21})}\\ D_3&=\frac{E_2'(1+j\eta_2)h^3}{12(1-\nu_{12}\nu_{21})} \quad D_4=\frac{G_{12}'(1+j\eta_{12})h^3}{3} \end{aligned} \tag{2.2}$$

Height parameters are introduced to describe the in-plane orthotropic behaviour, i.e. E_1' and E_2' are the storage moduli in x and y directions respectively, G_{12}' the shear modulus, ν_{12} and $\nu_{21} = E_2\nu_{12}/E_1$ are Poisson's ratios, η_1, η_2 and η_{12} are the loss factors, ratios of the imaginary and real parts of storage and shear moduli and $j^2=-1$.

Equation 2.1 is the equation governing the propagation of a wave in a plate. Such a wave can be described by two parameters: k_f and λ. The wavenumber k_f could be seen as the equivalent, for the spatial domain, of the frequency in the time domain and represents the magnitude of the wave vector having the same direction of the wave propagation. Such a vector can be divided into two components, in x- and y- directions, each one characterized by a wavenumber k_{f1} and k_{f2}, described by Eq. 2.3.

$$k_{f1}=\sqrt[4]{\rho h\omega^2/D_1} \qquad k_{f2}=\sqrt[4]{\rho h\omega^2/D_2} \tag{2.3}$$

As in the time domain, where the time frequency ω is directly related to the time period T ($\omega = 2\pi/T$), in the spatial domain the wavenumber k_f is directly related to the wavelength λ

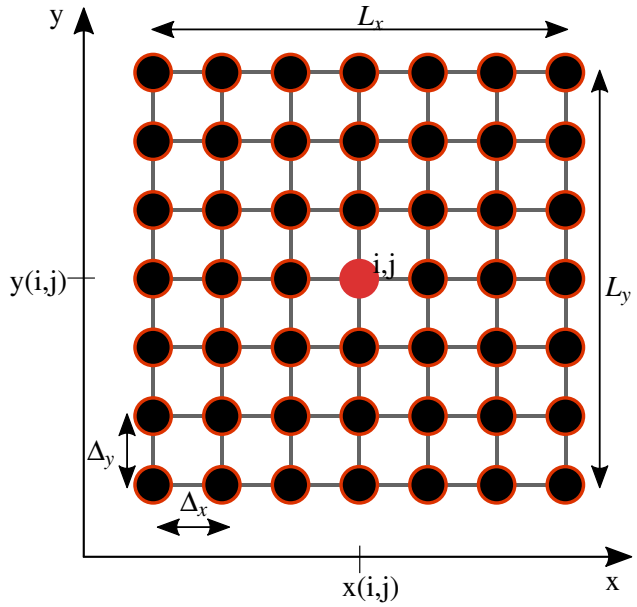

Fig. 2.7. Measurement grid

by Eq.2.4 [117].

$$\lambda = 2\pi/k_f \tag{2.4}$$

The wavelength λ represents then the length of the propagating wave. As for the wavenumber, the wavelength can also be described by the two orthogonal components, λ_x and λ_y.

Considering only a part of the structure free of any external load, in such a way that $p(x,y) = 0$, Eq. 2.1 becomes:

$$D_1 \frac{\partial^4 w}{\partial x^4} + (D_2 + D_4) \frac{\partial^4 w}{\partial x^2 \partial y^2} + D_3 \frac{\partial^4 w}{\partial y^4} = \rho h \omega^2 w(x,y) \tag{2.5}$$

Supposing that the material density ρ and the plate thickness h are known, measuring for each excitation frequency ω the displacement field $w(x,y)$ and calculating its derivatives $\partial^4 w/\partial x^4$, $\partial^4 w/\partial x^2 \partial x^2$ and $\partial^4 w/\partial y^4$, the only unknowns of Eq. 2.5 are the flexural stiffness velues. Measurements of the displacement fields are performed on a measurement grid constituted by points having coordinates such as the dimensions of the measured area L_x and L_y are discretized with a spatial resolution Δ_x and Δ_y for x- and y-directions respectively (Fig. 2.7). This approach allows to approximate the fourth order derivatives by a finite difference scheme and to write Eq. 2.5 in a

discretized form in the point (i,j):

$$\begin{bmatrix} \delta_{i,j}^{4x} & \delta_{i,j}^{2x2y} & \delta_{i,j}^{4y} \end{bmatrix} \begin{bmatrix} D_1 \\ D_2 + D_4 \\ D_3 \end{bmatrix} = \rho h \omega^2 w_{i,j} \tag{2.6}$$

where $i \in [1, N_x]$, $j \in [1, N_y]$ and N_x and N_y are respectively the number of points in each direction. The quantities $\delta_{i,j}^{4x}$, $\delta_{i,j}^{2x2y}$ and $\delta_{i,j}^{4y}$ are the fourth order approximated derivatives of displacement $w_{i,j}$ involved in the equation of motion. Theoretically, to know the dynamic properties at one point, only the displacements at this point and those necessary to calculate the spatial derivative approximations, have to be measured. Actually, in order to reduce the noise influence, an homogenization process is performed over a large number of measured points $N = N_x \times N_y$ constituting the measurement grid. Since that, as a consequence, the resulting equation system reported in Eq. 2.7 has a number of unknown lower than the number of equations, the least square resolution method is performed to find a solution for the identification of flexural stiffness values.

$$\begin{bmatrix} \delta_1^{4x} & \delta_1^{2x2y} & \delta_1^{4y} \\ & \dots & \\ \delta_N^{x4} & \delta_N^{2x2y} & \delta_N^{y4} \end{bmatrix} \begin{bmatrix} D_1 \\ D_2 + D_4 \\ D_3 \end{bmatrix} = \rho h \omega^2 \begin{bmatrix} w_1 \\ \dots \\ w_N \end{bmatrix} \tag{2.7}$$

The residual sum of squares ($\mathfrak{R}$) related to the found solution, can be calculated to estimate the quality of solution as:

$$\mathfrak{R} = \|\bar{w} - \nabla \bar{D}\|^2 \tag{2.8}$$

where $\bar{w}$ represents the right-hand side of Eq. 2.7, ∇ the derivatives matrix and $\bar{D}$ the identified vector of solutions. Once the solutions of Eq. 2.7 are obtained, the storage moduli and loss factors can be easily calculated by the real and imaginary part of the flexural stiffness values (Eq. 2.2).

2.3.2 Derivative approximation by finite differences

The finite difference scheme used to approximate the fourth-order partial derivatives of the displacement field involved in Eq. 2.1 is presented by Eq. 2.9:

$$
\begin{aligned}
\frac{\partial^4 w}{\partial x^4} \approx \delta_{i,j}^{4x} &= \frac{1}{\Delta_x^4}(w_{i+2,j} - 4w_{i+1,j} + 6w_{i,j} - 4w_{i-1,j} + w_{i-2,j}) \\
\frac{\partial^4 w}{\partial y^4} \approx \delta_{i,j}^{4y} &= \frac{1}{\Delta_y^4}(w_{i,j+2} - 4w_{i,j+1} + 6w_{i,j} - 4w_{i,j-1} + w_{i,j-2}) \\
\frac{\partial^4 w}{\partial x^2 y^2} \approx \delta_{i,j}^{2x2y} &= \frac{1}{\Delta_x^2 \Delta_y^2}(w_{i+1,j+1} - 2w_{i+1,j} + w_{i+1,j-1} - 2w_{i,j+1} \\
&\quad + 4w_{i,j} - 2w_{i,j-1} + w_{i-1,j+1} - 2w_{i-1,j} + w_{i-1,j-1})
\end{aligned}
\tag{2.9}
$$

where $i \in [3, N_x - 2]$, $j \in [3, N_y - 2]$. It should be pointed out that the identification of the dynamic properties can not be performed on all measured points because the derivative calculation at each point requires 13 surrounding points of measure (Fig. 2.8). Therefore, the displacement

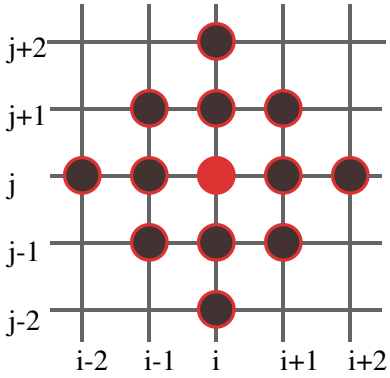

Fig. 2.8. Points involved in the approximation of the fourth order partial derivatives at the point (i,j).

measurements on the first and the last two rows and columns of the grid are fundamental to the calculation of the inner points, but no information about the dynamic properties on these points can be obtained.

2.3.3 Windowing and filtering

Displacement measurements are generally affected by noise which can compromise the identification results. Moreover, the fourth-order partial derivative approximations presented in section 2.3.2 contribute to amplify the noise related to displacement measure. For this reason, a preliminary regularization step is necessary. Therefore, before the least squares calculation of Eq. 2.7, the displacement field and its derivatives are windowed and filtered. The formulation of both the window and the low-pass filter are expressed as a function of the parameter k_c, represent-

ing the cut-off wavenumber. The solution of Eq. 2.7 is estimated using different values of k_c, then this latter is optimised in relation to the $\Re$ values (Eq. 2.8).

The windowing step allows to avoid the singularity issues over the edges of the measured area which occur with the application of the filter [105]. Indeed, the window replaces the truncation of the measured displacement field with a smooth variation. Different type of windows are available in literature [118]. In [111], the Tukey window is chosen because it is defined as a combination of a rectangular windows (in the core) and a Hanning one (on the edges) and therefore it allows to smooth the edges without altering the core data. Taking into account that the points of measure involved in the dynamic stiffness calculation are only the (i,j) for which $i \in [3, N_x - 2]$ and $j \in [3, N_y - 2]$ as explained in section 2.3.2, the expression of the two-dimensional Tukey window $\psi^{2D}_{i,j}$ calculated at the point (i,j) of coordinates $x_{i,j}$ and $y_{i,j}$, is the following:

$$\psi^{2D}_{i,j}(x) = \psi^{1D}(x_{i,j} - 2\Delta_x)\psi^{1D}(y_{i,j} - 2\Delta_y) \tag{2.10}$$

with

$$\psi^{1D} = \begin{cases} 0.5\left(1 - \cos\left(\frac{\pi x}{\alpha}\right)\right), & \text{if } 0 \leq x < \alpha \\ 1, & \text{if } \alpha \leq x < L - \alpha \\ 0.5\left(1 - \cos\left(\frac{\pi(x - L + 2\alpha)}{\alpha}\right)\right), & \text{if } L - \alpha < x \leq L \\ 0, & \text{else,} \end{cases} \tag{2.11}$$

and

$$\alpha = \begin{cases} \lambda_c, & \text{if } L \geq 2\lambda_c \\ L/2, & \text{else} \end{cases} \tag{2.12}$$

$L = L_x - 4\Delta_x$ and $\lambda_c = 2\pi/k_c$. The expressions of ψ^{1D}, L and α, here reported for the x direction, can be similarly written for the y direction. As shown in Fig.2.9, when α tends to zero the window takes a shape of a rectangular window, while when α tends to L/2 the window takes the expression of a Hanning one.

Once the displacement and derivative fields are windowed, they are convolved with the low-

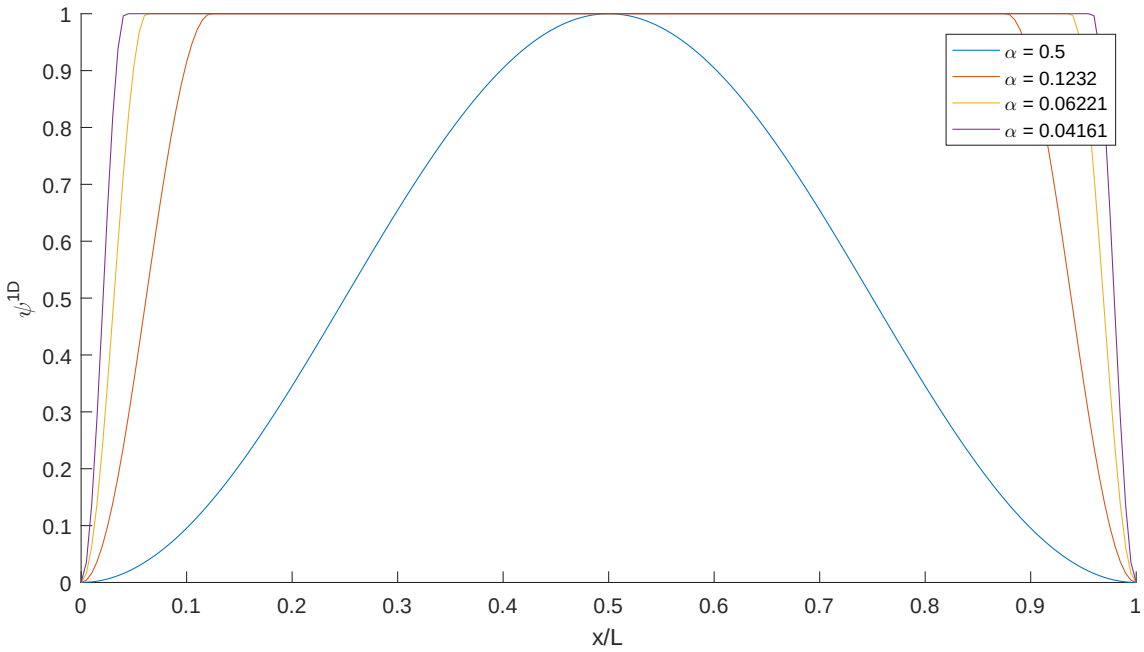

Fig. 2.9. Tukey window for different values of α. On the abscissa, the x-coordinate is normalized to the length L_x.

pass filter calculated as follows:

$$h(x,y) = \begin{cases} \frac{k_c^2}{4\pi^2 xyN_f}\left(1-\cos\left(\frac{k_c x}{2}\right)\right)\left(1-\cos\left(\frac{k_c y}{2}\right)\right)\sin(k_c x)\sin(k_c y), & \text{if x and y} \in \left[-\frac{2\pi}{k_c}, \frac{2\pi}{k_c}\right] \\ 0 & \text{else} \end{cases} \tag{2.13}$$

where N_f is a normalization parameter, such that $\int_{L_x}\int_{L_y} h(x,y)dxdy = 1$. As can be noted, both the window and the low-pass filter are expressed in function of k_c, which takes the same value for both, as suggested in the original FAT formulation [105]. The selection of the cut-off number k_c is crucial for the good identification of solution in Eq. 2.7. In [111] an automatic determination of this parameter is proposed: the flexural stiffness values and the related residuals $\Re$ are calculated using different values of k_c. Thus, the derivative of the residuals $\Re$ against the values of k_c is calculated. The optimal value k_c^{opt} is chosen as the maximum value of k_c for which the derivative remains below a certain threshold.

2.3.4 Algorithm

To give a clear insight of the procedure, the algorithm used for the dynamic property identification method is here reported:

1: **for** $f \in [f_{min}, f_{max}]$ **do**
2: $\bar{w} \leftarrow$ get displacement field at frequency f
3: $\nabla \leftarrow$ calculate the partial derivatives from Eq. 2.9
4: **for** $k_c \in [k_c^{min}, k_c^{max}]$ **do**
5: $\bar{w}$,$\nabla \leftarrow$ apply to each field the window and the filter using a cut-off wavenumber k_c
6: $\bar{D} \leftarrow$ calculate the least squares solution
7: $\mathfrak{R} \leftarrow$ calculate the residual sum of squares from Eq. 2.8 for each k_c
8: **end for**
9: D($\mathfrak{R}$) $\leftarrow$ calculate the derivatives in k_c of the least squares solutions
10: $k_c^{opt} \leftarrow$ choose the optimum k_c as in section 2.3.3
11: $D_{sel} \leftarrow$ select the solution D related to k_c^{opt} and frequency f
12: E_1', E_2', η_1, η_2, G_{12}', $\eta_{12} \leftarrow$ calculate storage moduli and loss factors for each D_{sel} and frequency f
13: **end for**

Such an algorithm is entirely implemented on Matlab [119] in the course of the present PhD work.

2.4 Displacement measurement by digital image correlation

The objective of this PhD work is to apply the FAT-based method presented above to identify the storage moduli and loss factors of the FF/PA11 composite introduced in chapter 1. For this purpose, the out-of-plane displacements of a vibrating plate are measured. As shown in Fig. 2.10, the plate is excited by an electro-mechanical shaker in the left bottom corner and suspended on a metallic frame at the two upper corners in a free-free boundary conditions in such a way to have fibres parallel to the x-direction. In the following of this study it is considered for convention that such a fibre orientation corresponds to a 0° configuration whereas, when the fibres are parallel to the y-direction the plate is in a 90° configuration. An impedance head B&K Type 8001 is used to measure the excitation force.

The first technique for the displacement measurements used in the present study is the digital image correlation (DIC). Indeed, a thorough search of the relevant literature yielded no results related to the application of such a technique to the FAT-based identification method.

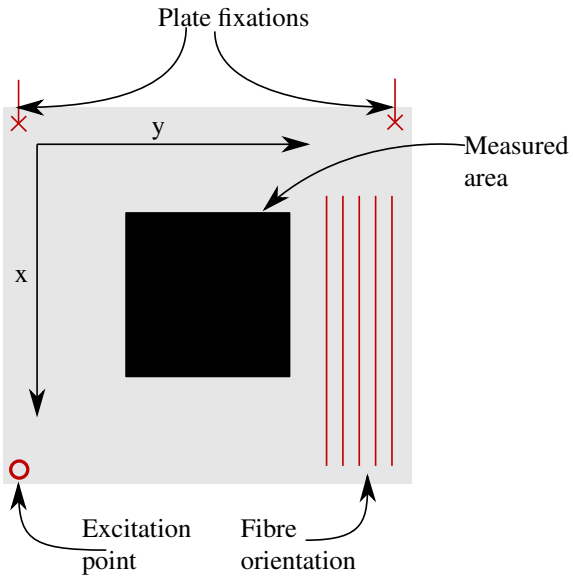

Fig. 2.10. Schema of the suspended plate (460 mm along x-direction and 500 mm along y-direction): two strings fix the plate to the metallic frame. The vertical red lines indicate the fibre orientation in case of 0° configuration.

DIC is a non-contacting technique that allows displacement measurement of an object by acquisition of images of the object in a digital form. Such a technique is already employed to study the mechanical behaviour of material and structures [120] as well as for the full-field vibration measurements [121, 122] and as support of the experimental modal analysis [123, 124, 125]. The main advantage of this technique is that the displacement field of the entire area of interest is measured at the same time, with a very high spatial resolution. For measurement of the out-of-plane displacement field by DIC technique, two cameras are required. Numerical correlation calculated between the two images captured simultaneously on the "deformed" area and the ones initially captured on the "undeformed" area and taken as references, gives a measure of the displacement field. To calculate this correlation, a speckle pattern (a black and white dotted pattern) may be applied on the area of interest. In order to reduce the noise impact on the results, some parameters have to be taken into account [126]:

- The size of the speckle pattern, such as the average dot diameter, for which a value between 3 pixels and 5 pixels is generally suggested.
- The coverage factor, which represents the ratio of the black dot area over the total observed area. A value between 40 % and 70 % leads to optimal measurements.
- The dimensions of the subsets, that are the sub-regions of some pixels in which the captured

images could be divided. In the correlation process, each subset is recognized in all the images and its comparison with the corresponding subset of the "undeformed" images, allows the calculation of the displacements. The dimensions of subsets are generally defined by the subset "entropy": a low value of entropy leads to ordered dots in a grid which corresponds to a small subset, whereas a high value of entropy leads to more dispersed dots, then to a larger subset. Good results are obtained with subsets large enough to be different from the others.

Two Photron SA1.1 high-speed cameras set in front of the plate (Fig. 2.11(a)) and characterized by a sampling frequency of 5400 Hz, are used in this study. Due the limited hard-disk capacity up to 5500 images in high resolution (1024 pixels $\times$ 1024 pixels), the signal can only be sampled over a time of 1 s. According to the Shannon-Nyquist sampling principle, the plate is excited with a sinusoidal chirp from 50 Hz up to 1000 Hz swept in 1 s. Moreover, a Deolight 400D lamp is used to illuminate the sample. A specific software is used to generate the speckle pattern respecting the optimal criteria which is then printed on a paper over an area of 180 mm $\times$ 180 mm and glued at the centre of the plate (Fig. 2.11(b)). The measured displacement field (Fig. 2.11(c)) is then obtained over the area covered by the speckle pattern with a spatial step lower than 1 mm and converted in the frequency domain.

Storage moduli and loss factors calculated by the FAT-based method using the displacement field obtained by the DIC measurements and the procedure described in section 2.3.4 are presented in Fig. 2.12. It can be seen that the results are affected by an important dispersion, making impossible an accurate dynamic property identification. Such a dispersion is initially ascribed to measurement noise. For this reason, a study of the impact of noise on the dynamic properties identification using an analytical displacement field is carried out and presented in section 3.3.

Nevertheless, the failure to achieve the expected results on the material dynamic properties identification could not be ascribed only to the noise impacting the measured displacement field. Indeed, further analysis and investigations [127] lead to pursue a reduction of the excitation time. Actually, a fast excitation leads to measure the displacements in a transition regime and no longer in a steady state condition. In this way, the establishment of a preponderant vibration mode, which occurs exciting the plate in the vicinity of a natural frequency, is avoided. Given that the noise has a more important impact when measurements are performed close to a modal vibration [105], an excitation by a slow chirp leads to noisy results. Therefore, additional analysis are carried out

exciting the plate with a sinusoidal signal between 25 Hz and 10 000 Hz swept in 0.3 s. The chirp is reiterated 10 times over a period of 3 s to average the measures and reduce the noise impact. Due to the limitation of the camera sampling rate, only frequencies up to 2000 Hz are considered. Such analysis leads to results similar to those shown in Fig. 2.12. Therefore, the next section of this work is addressed to a more reliable displacement field measurement technique, the laser Doppler vibrometer.

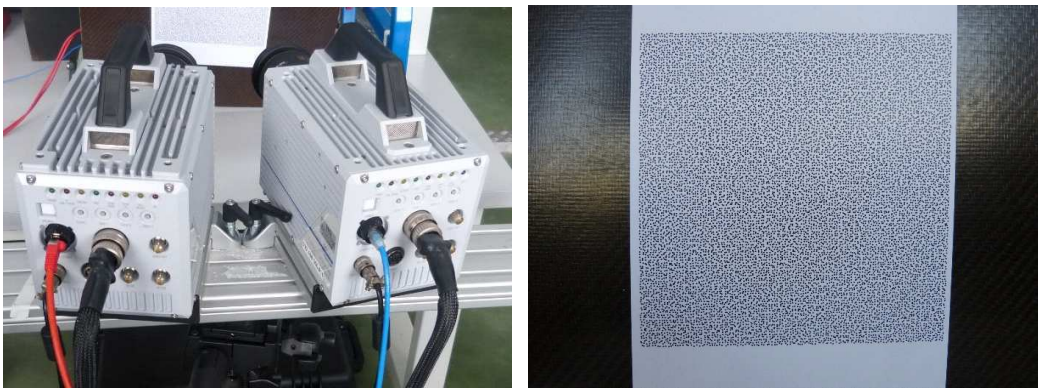

(a) (b)

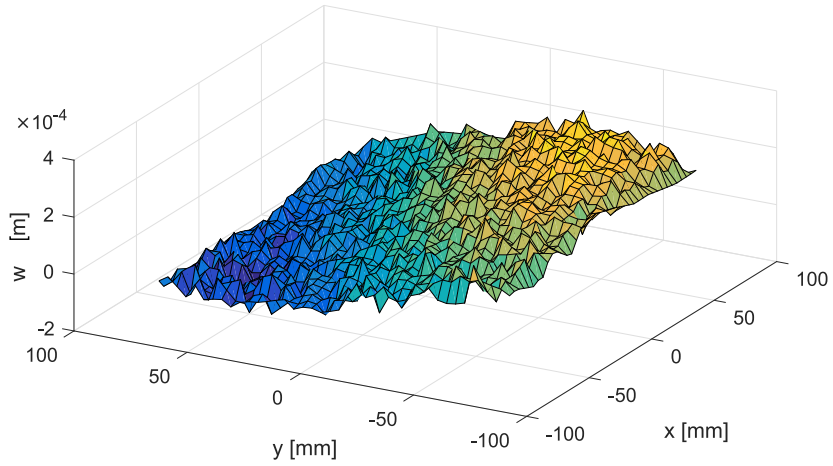

(c)

Fig. 2.11. Experimental setup for displacement measurement by DIC (a), the speckle pattern glued on the vibrating plate of dimensions 180 mm × 180 mm (b) and the displacement field measured at f = 200 Hz (c). The centre of the observed area corresponds to x = 0 mm and y = 0 mm, whereas the excitation point located in the left bottom corner is in the negative values of the coordinates. The maximum and minimum measured values are ± 200 µm.

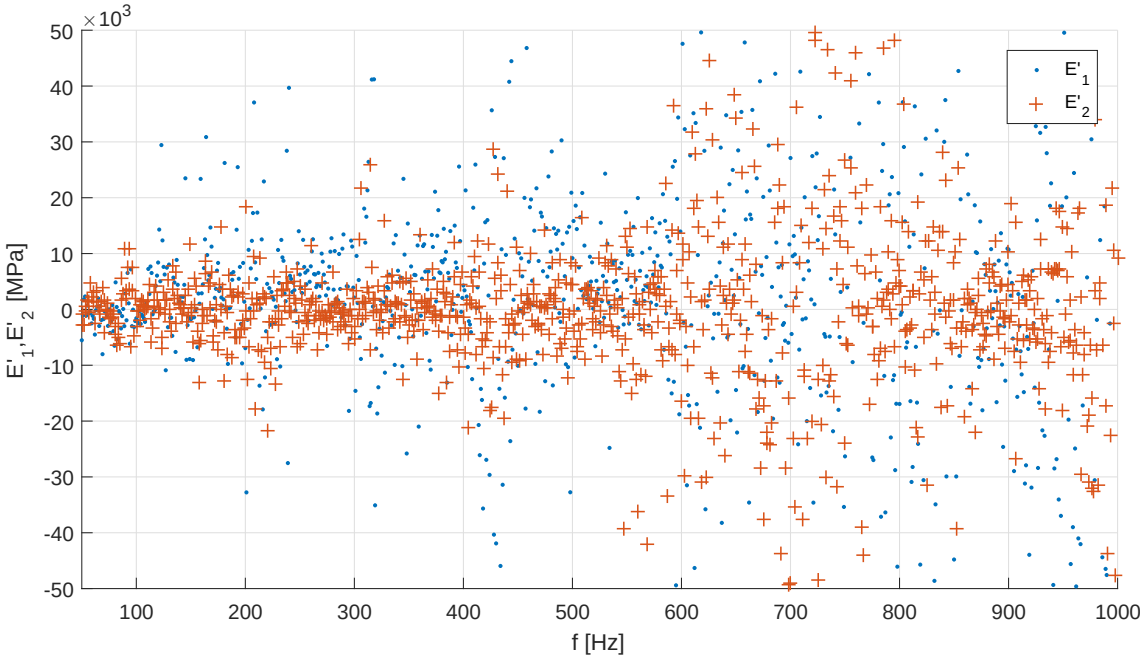

(a) Storage moduli

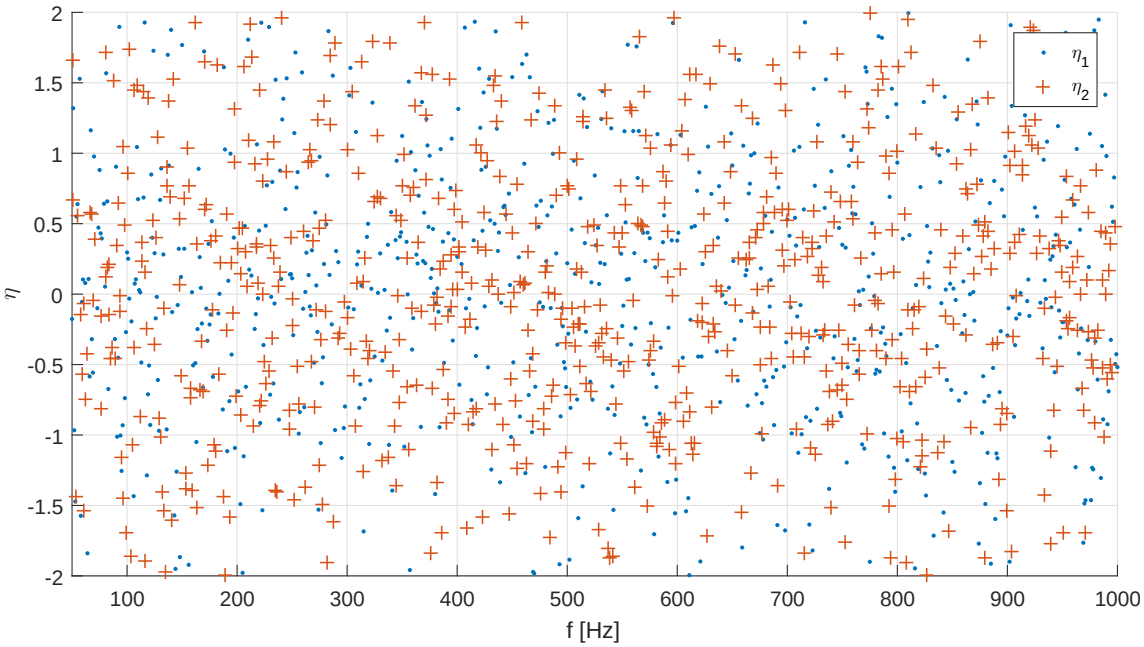

(b) Loss factors

Fig. 2.12. Results obtained from DIC measurements over a range of frequency $f \in [25\,\text{Hz}, 1000\,\text{Hz}]$.

2.5 Displacement measurement by laser Doppler vibrometer

In order to reduce the impact of noise affecting the displacement measurements, another measurement technique i.e. the laser Doppler vibrometer (LDV) system is also employed in this study. The technique is based on the correlation between a laser beam reflected from a surface and another beam taken as reference. Such a correlation is strictly related to the the surface velocity (thus the displacement and acceleration) at the point of incidence of the laser beam. Therefore, in contrast to DIC technique, LDV can only measure the displacement at points on a grid one by one, but it is characterized by a better reliability [128, 129]. This technique is firstly validated on a transversely orthotropic material and then applied to the FF/PA11 composite.

2.5.1 Experimental setup

Three different environments are used for the experimental displacement measurements carried out in this PhD study: two ESTACA laboratories in Saint-Quentin-en-Yvelines and in Laval, as well as the Laboratoire d'Acoustique de l'Université du Mans (LAUM) in Le Mans [1]. For all of these environments, the same configuration (Fig. 2.10) is respected: the plate is suspended by the upper corners to a metallic frame in order to simulate the free-free boundary conditions and a shaker, controlled by an amplifier, excites the plate in a bottom corner. An impedance head placed between the plate and the shaker is also used to measure the force applied to the excitation point. Both the amplifier and the impedance head are connected to the PC which commands the amplifier with the desired signal and acquires the force signal from the impedance head.

The same equipments are used in the ESTACA laboratories in Saint-Quentin-en-Yvelines and Laval (Fig. 2.13(a)):

- a permanent magnet shaker LDS V201 by Brüel & Kjær is placed on a horizontal support and connected to a bottom corner of the plate (Fig. 2.13(b));
- a metallic frame at which the plate is suspended by the two upper corners as shown in Fig. 2.13(c);
- a Polytec PSV-400 scanning vibrometer (Fig. 2.13(c)), situated at a distance of about 1 m, measures the out-of-plane displacements of the vibrating plate on a defined grid of points

[1] The author is grateful to J.M. Genevaux for grant access to the LAUM experimental facilities.

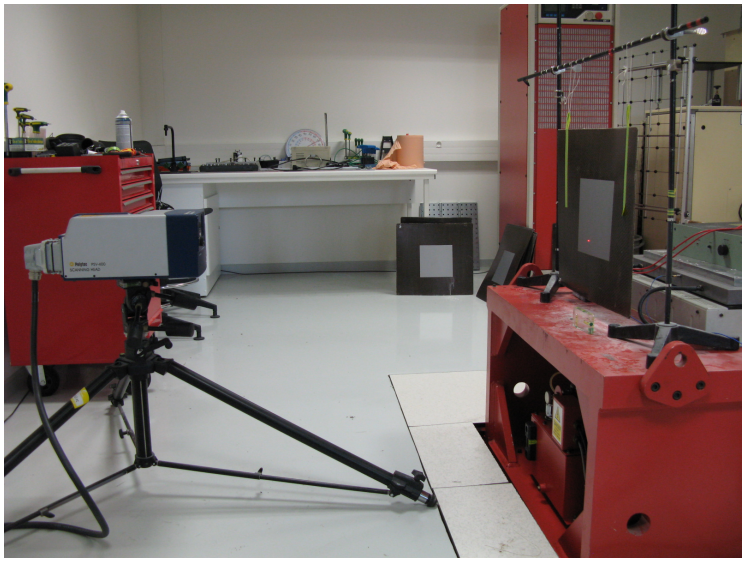

(a) Overview

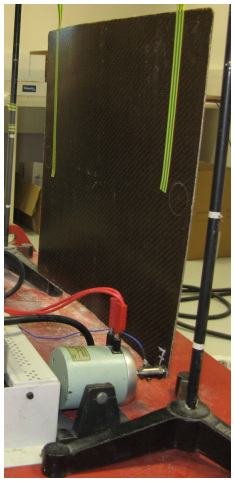

(b) Shaker

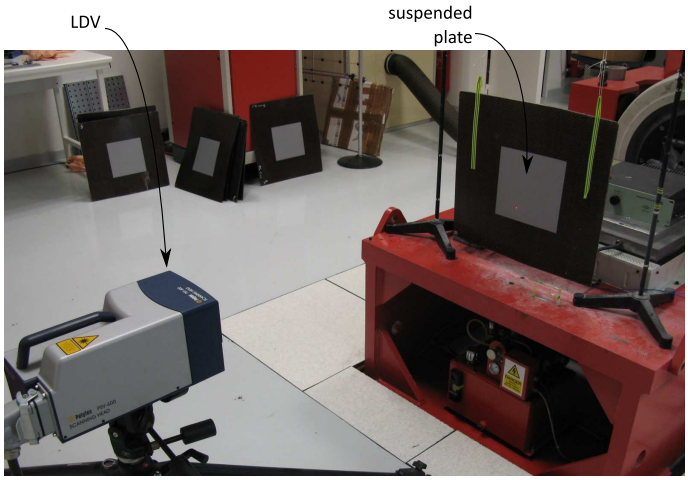

(c) Plate and vibrometer (LDV)

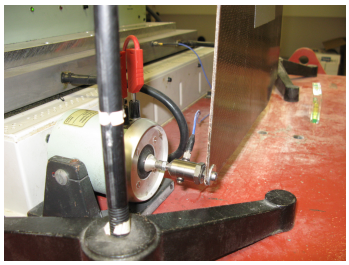

(d) Impedance head

Fig. 2.13. Experimental setup in SQY

(a) (b)

Fig. 2.14. Experimental setup in LAUM (a) and installation of the impedance head between the plate and the shaker (b)

using the vertical direction as the x-direction and the horizontal one as the y-direction. In order to increase the light reflection, an adhesive light reflective paper is glued on the measured area of the plate. Any eventual excess of light in the laser Doppler vibrometer (LDV) sensor, which leads to saturation issues, is adjusted with the application of a layer of metallic paint.

- an impedance head B&K Type 8001 placed between the plate and the shaker (Fig. 2.13(d)).

Tests are also conducted in a third laboratory, the Laboratoire d'Acoustique de l'Université du Mans (LAUM) in Le Mans, using a different shaker for the plate excitation and a different LDV system for the displacement measurements. In this case, the experimental setup employed, shown in Fig. 2.14(a), consists of:

- a metallic structure at which the plate is suspended by the two upper corners;
- a permanent magnet shaker LDS V406 by Brüel & Kjær, placed on an isolation table and driven by an amplifier;
- an impedance head B&K Type 8001 screwed to the plate and connected to the shaker by a metal stem (Fig. 2.14(b));
- a Polytech PSV-500 scanning vibrometer for the displacement field measurements.

2.5.2 Validation on a transversely orthotropic material

In order to validate the dynamic properties identification method on LDV measurements, a transversely orthotropic plate is firstly tested. The test is carried out on a plate obtained by a pre-impregnated SMC S 8010, a sheet moulding compound which consists of glass fibres and a mix of different thermoset polymers. Quasi-static tensile tests in the two principal directions of the rectangular plate are performed and similar values for the Young modulus are obtained, thus highlighting the transversely orthotropic behaviour of the material, with the characteristics reported in Table 2.1 [130].

Property	Value
Young's modulus E [GPa]	15.38
Poisson's ratio ν	0.32
Material density ρ [kg m^{-3}]	1750

Table 2.1: Mechanical characteristics of SMC plate [130].

In order to measure the out-of-plane displacement field of the vibrating plate, measurements are carried out in the LAUM laboratory The plate has dimensions of 460 mm $\times$ 500 mm and a thickness of 2.3 mm. The displacement field is measured over a grid of 41 points $\times$ 41 points covering an area at the centre of the plate of 200 mm $\times$ 200 mm with a spatial resolution of $\Delta_x = \Delta_y = 5$ mm. The excitation, applied in the left bottom corner of the plate, consists of a sinusoidal chirp swept between 25 Hz to 10 000 Hz in 0.04 s. The out-of-plane displacements are measured by the LDV system during the excitation time. In order to average the measures and reduce the noise affecting the experimental data, the measurements are iterated 10 times at each point. Once the 10 measurements are performed at on point, the same procedure is applied at the next one until all the points of the grid are measured. The dynamic properties identification method is then applied to the entire displacement field. For this purpose, the material density, the Poisson's ratios (Table 2.1) as well as the thickness of the plate are used as input data.

Figure 2.15 reports the real part of the flexural stiffness values D_1, D_3 and D_{24} divided by the material density and plate thickness. As observed, the transversely orthotropic behaviour shown by the quasi-static tensile tests, is also noted by the vibratory method. Indeed, the flexural stiffness D_1 and D_3 assume similar values of about 5.45 m^4 s^{-2}. Moreover, the flexural stiffness value $D_{24} = D_2 + D_4$ is quite lower than the others and amounts to 5.05 m^4 s^{-2}. The storage moduli E_1' and E_2' are then directly calculated from the real part of the flexural stiffness values D_1 and D_3

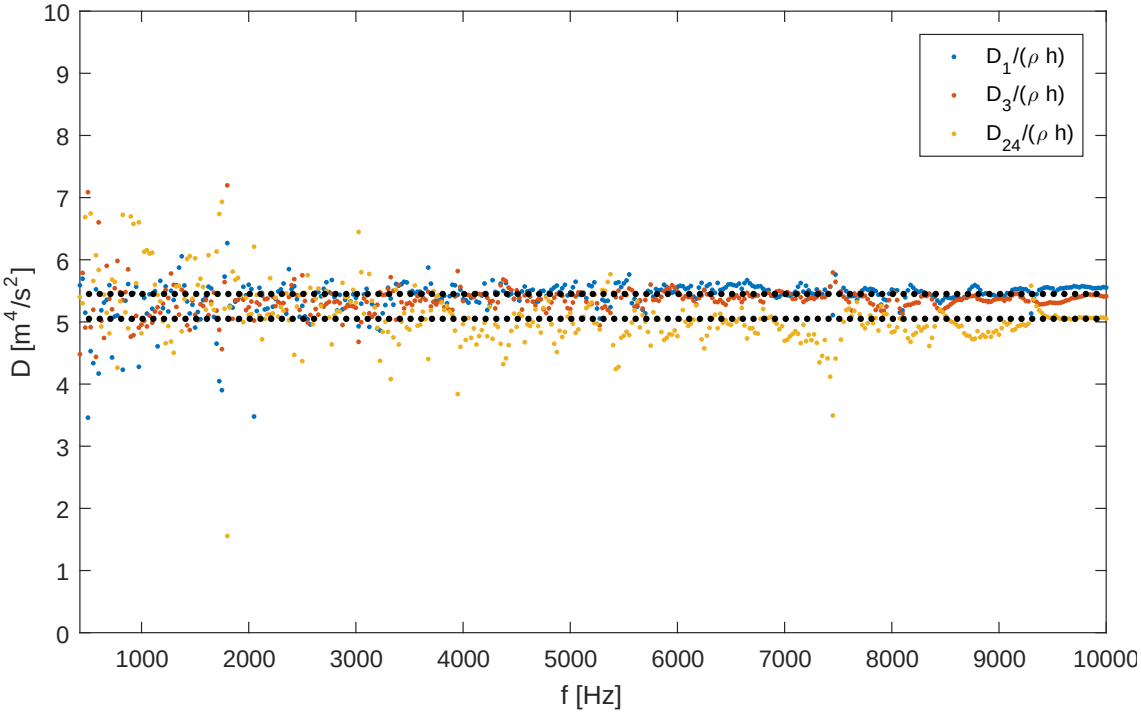

Fig. 2.15. Flexural stiffness values obtained by LDV measurement on the transversely orthotropic material. The mean values are reported with black dotted lines.

respectively. The loss factors η_1 and η_2 are obtained by the ratio between the imaginary part and the real part of the flexural stiffness D_1 and D_3. Similarly, the storage modulus G'_{12} and η_{12} are calculated from the real and imaginary parts of the flexural stiffness D_4 which in turn is obtained by $D_4 = D_{24} - D_2$ (Eq. 2.2).

Figure 2.16 reports the storage moduli and the loss factors in the vertical (1) and horizontal (2) directions of the plate as well as the shear modulus G'_{12} and the relative loss factor η_{12}. A value of the storage modulus in the two directions equal to 16.3 GPa is obtained over the range of frequencies between 25 Hz and 10 000 Hz. This value remains quite constant over the entire range of frequencies. Nevertheless, as already observed in literature, a more important dispersion characterizes the data for frequencies up to 2000 Hz. Moreover, a shear modulus of 2.9 GPa is identified. In Fig. 2.16(b) the identified loss factors are also reported. In this case, the results are widely dispersed for frequencies up to 8000 Hz. Above this value, a loss factor of 0.02 is identified for η_1 but the curves of loss factors η_2 and η_{12} are characterized by large fluctuations which make impossible the effective identification.

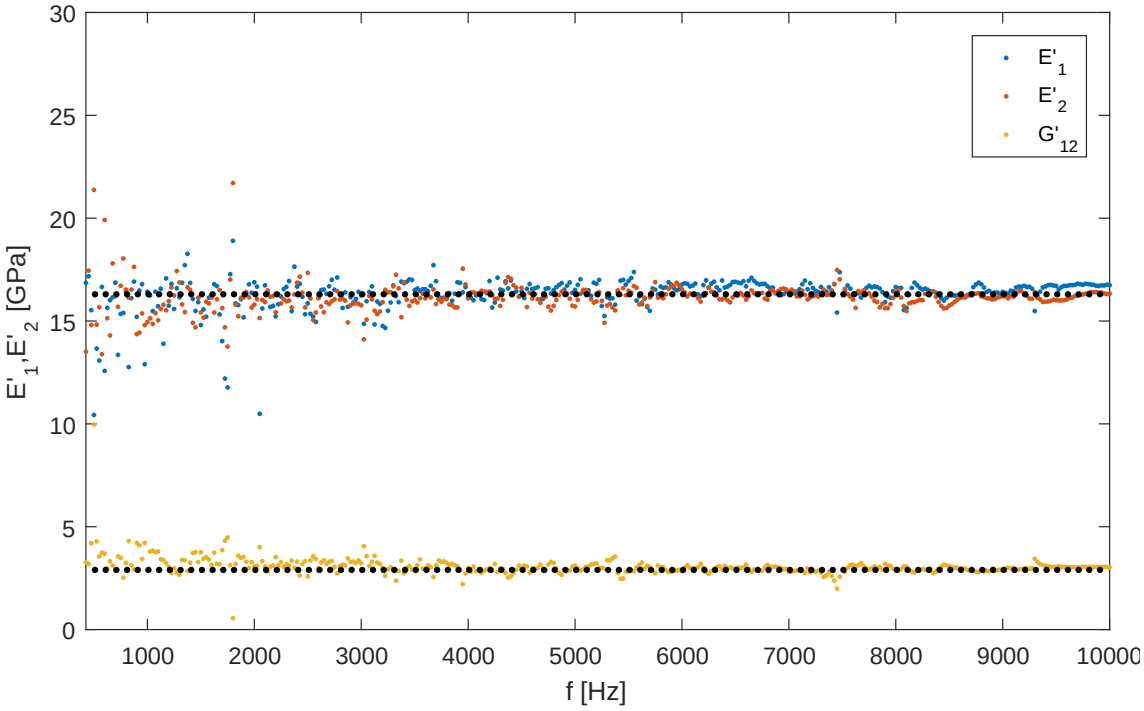

(a) Storage moduli

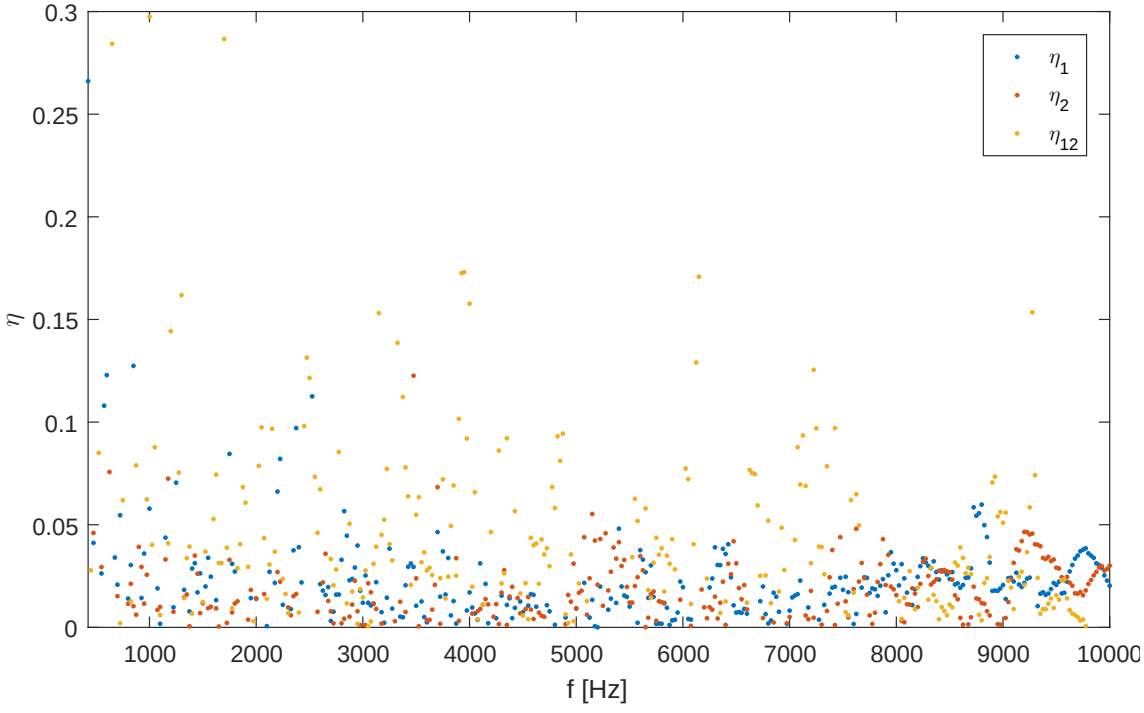

(b) Loss factors

Fig. 2.16. Results obtained on SMC material from LDV displacement field measurements. The dotted lines represent the mean values of the identified storage moduli.

In the wake of such results, the dynamic properties identification method is applied to a FF/PA11 plate using the same excitation configuration and measuring the displacement field by a LDV system. The next section is then addressed to the presentation of such results.

2.5.3 First results on FF/PA11

Once the method as well as the displacement measurement technique and the excitation way are validated as shown in the previous section, the same parameters are applied to characterize the dynamic behaviour of a FF/PA11 plate [88]. The displacement field of a vibrating plate suspended in such a way to have the material fibres parallel to the x-direction (0° configuration), is measured. In this way the identified dynamic properties in x- and y- directions are coincident with those in the material orthotropic directions. The measurements, carried out in the laboratories of Saint-Quentin-en-Yvelines, are conducted over an area of 200 mm × 200 mm on a measurement grid of 41 points × 41 points, resulting in a spatial resolution $\Delta_x = \Delta_y = \Delta = 5$ mm. For each point of the grid, the plate is excited with a sinusoidal chirp between 25 Hz and 10 000 Hz swept in 0.04 s. In order to reduce the noise of measurement, the average values of displacements are calculated performing the frequency chirp 10 times. The displacement magnitude is of the order of a few hundreds of μm at low frequency and of a few μm above 2 kHz (Figs. 2.17(a) and 2.17(b)). The measured displacement field so obtained and converted in the frequency domain is used as input of the dynamic properties identification method.

The real part of the identified flexural stiffness values $D_1/\rho h$, $D_3/\rho h$ and $D_{24}/\rho h = (D_2 + D_4)/\rho h$, solutions of Eq. 2.7, are reported in Fig. 2.18. In this case the anisotropic behaviour of the material is highlighted. Indeed, it is observed that both the flexural stiffness D_3 and D_{24} assume constant values of $2\,\mathrm{m}^4\,\mathrm{s}^{-2}$ all over the frequency range, whereas the flexural stiffness D_1 relative to the fibre direction assumes values much higher. Moreover, this latter presents an evident decreasing trend. Indeed, the D_1 values go from $11\,\mathrm{m}^4\,\mathrm{s}^{-2}$ at 1000 Hz down to $9\,\mathrm{m}^4\,\mathrm{s}^{-2}$ at 10 000 Hz.

Once the flexural stiffness values are identified, the storage moduli E'_1, E'_2 and G'_{12} as well as the loss factors η_1, η_2 and η_{12} can be calculated as done in section 2.5.2. The identified values of storage moduli and loss factors are shown in Fig. 2.19. The identified storage modulus in fibre direction (direction 1) and transverse one (direction 2) as well as the shear storage modulus G'_{12} are significantly different (Fig. 2.19(a)). However, loss factors are not identified with a good

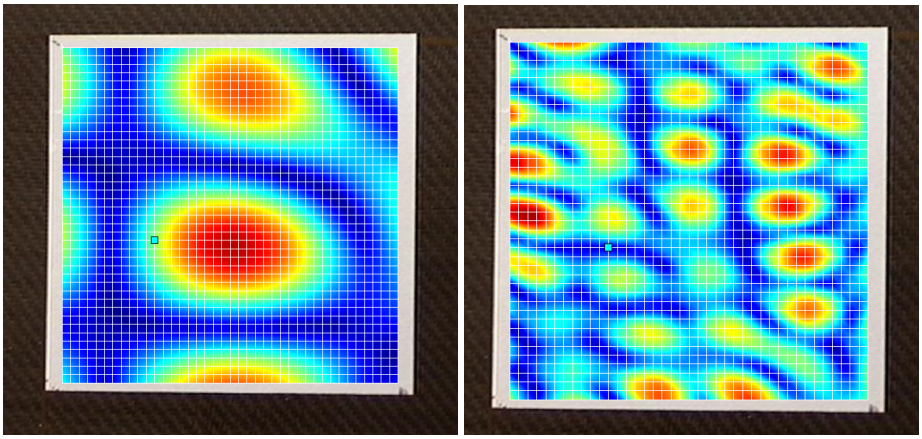

(a) Displacement field at 450 Hz (b) Displacement field at 3750 Hz

Fig. 2.17. Iso-values of the normal displacement at 450 Hz (a) and 3750 Hz (b). The maximum and minimum values (in red and blue respectively) are $\pm$ 200 µm at 450 Hz and $\pm$ 7 µm at 3750 Hz. The measurement area has dimensions of 200 mm$\times$200 mm at the centre of the plate of dimensions 460 mm$\times$500 mm.

accuracy (Fig. 2.19(b)). Indeed, the curves are characterized by fluctuations which could be due to phenomena related to the plate natural frequencies.

2.5.3.1 Storage moduli

The obtained storage modulus values are about 26 GPa in the fibre direction and 5.3 GPa in the transverse one whereas the shear modulus assumes values of 1.3 GPa. As can be observed in Fig. 2.19(a), the longitudinal storage modulus is characterized by a marked decreasing trend already observed in the curve related to the flexural stiffness D_1 (Fig. 2.18), thus leading to a drop off of about 20 % of its value from a frequency of 1000 Hz to 10000 Hz. A quite constant value of the transverse and shear storage moduli all over the range of frequency is instead observed. Furthermore, it is noteworthy that a certain dispersion characterizes the beginning of the curve, for frequencies below 1000 Hz. This issue, already observed in [127] and in [113], could be due to the finite dimensions of the observation area. Indeed, at low frequencies, the corresponding wavelength is large compared to the measurement area. Furthermore, the identified storage modulus in the transverse direction is less affected by this kind of dispersion, in agreement to the fact that the material is less stiff in the transverse direction than in the longitudinal one (see Table 1.5) and, therefore, given the relation of the wavelength $\lambda_f = 2\pi/k_f$ where $k_f = \sqrt[4]{\rho h \omega^2 / D}$ is the wavenumber of a propagative wave and D is the flexural stiffness in fibre or transverse direction, it is then

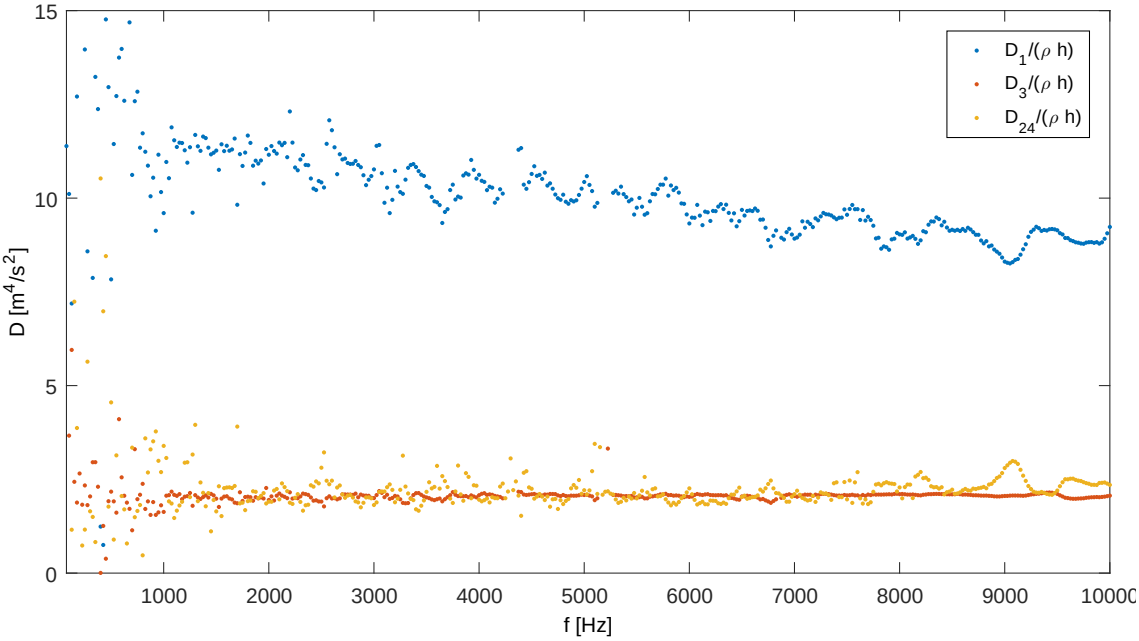

Fig. 2.18. Flexural stiffness values obtained by LDV measurement with a $\Delta_x = \Delta_y = \Delta = 5\,\text{mm}$

smaller in the transverse direction. To identify material dynamic properties at lower frequencies, a wider area should be used. Moreover, because of the difference of the stiffness values between the two directions, a rectangular observation area could be considered. Indeed, a wide dimension is required in the fibre direction to observed large wavelength whereas a smaller dimension could be sufficient in the transverse direction where the wavelength are shorter. The size and the shape of the area of interest are two of several parameters on which a sensitivity analysis is conducted and presented in the next chapter of this PhD work. Hereinafter, the discussion is only addressed on the storage moduli E_1' and E_2' as well as the loss factors η_1 and η_2.

In order to analyse the dispersion relative to the material, 3 plates are chosen for the identification of longitudinal and transverse storage moduli, respectively shown in Figs. 2.20(a) and 2.20(b). It is noted that the decreasing trend characterizing the longitudinal storage modulus curve shown in Fig. 2.19, is observed for all the 3 plates (Fig. 2.20(a)). Moreover, also the dispersion impacting on results for frequencies lower than 2000 Hz is still noticeable. An important dispersion is also observed in Fig.2.20(b) relative to the storage moduli in the transverse direction. Moreover, a slight increasing trend seems to characterize the concerned curves. The results on longitudinal and transverse storage moduli are averaged over the plates at frequencies between 1000 Hz and 10 000 Hz. Assuming a normal distribution of all variability sources impacting the dynamic parameters, the mean and standard deviation of E_1' and E_2' on the 3 plates are calculated. Each

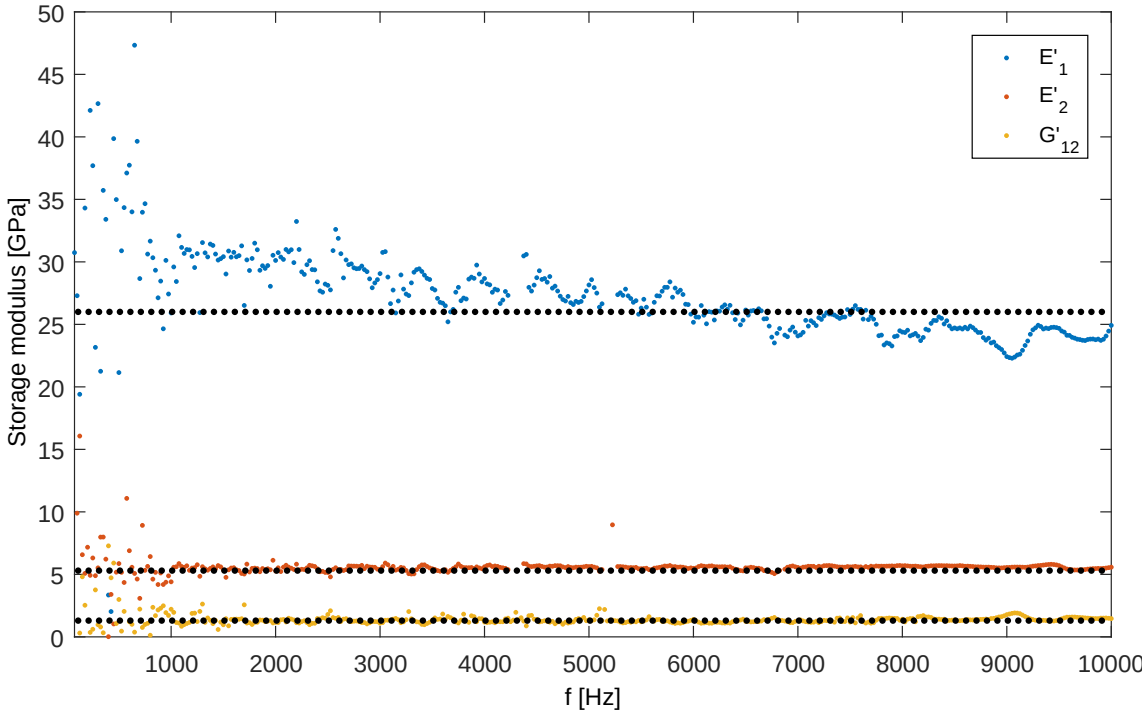

(a) Storage moduli

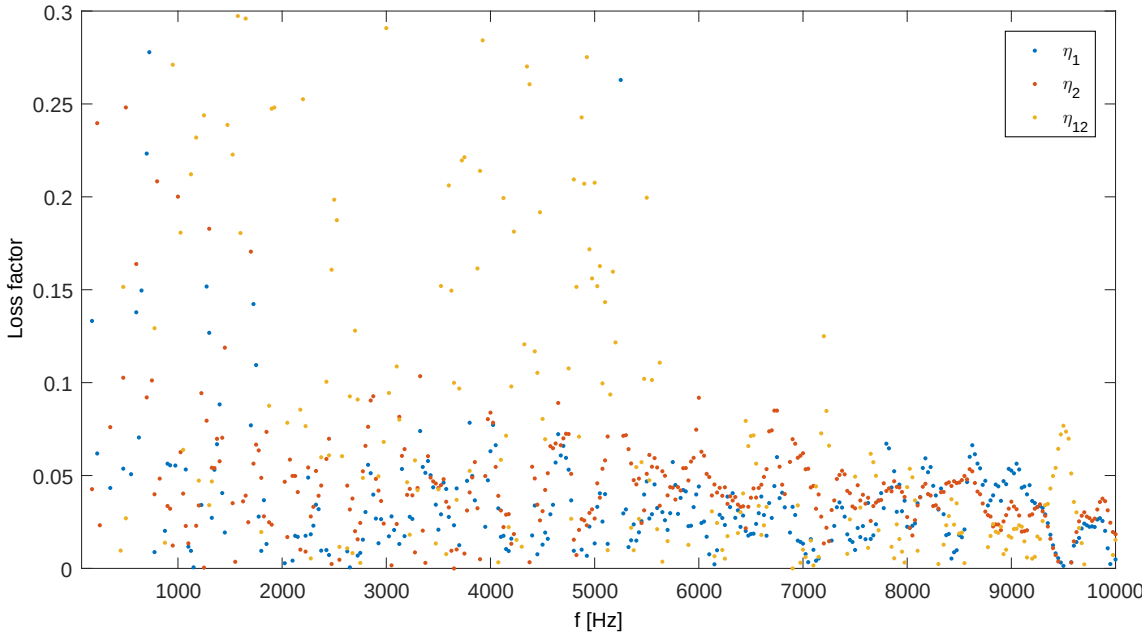

(b) Loss factors

Fig. 2.19. Storage moduli (a) and loss factors (b) obtained by LDV measurement with a $\Delta_x = \Delta_y = \Delta = 5\,\text{mm}$. The dotted lines represent the mean values of the identified storage moduli.

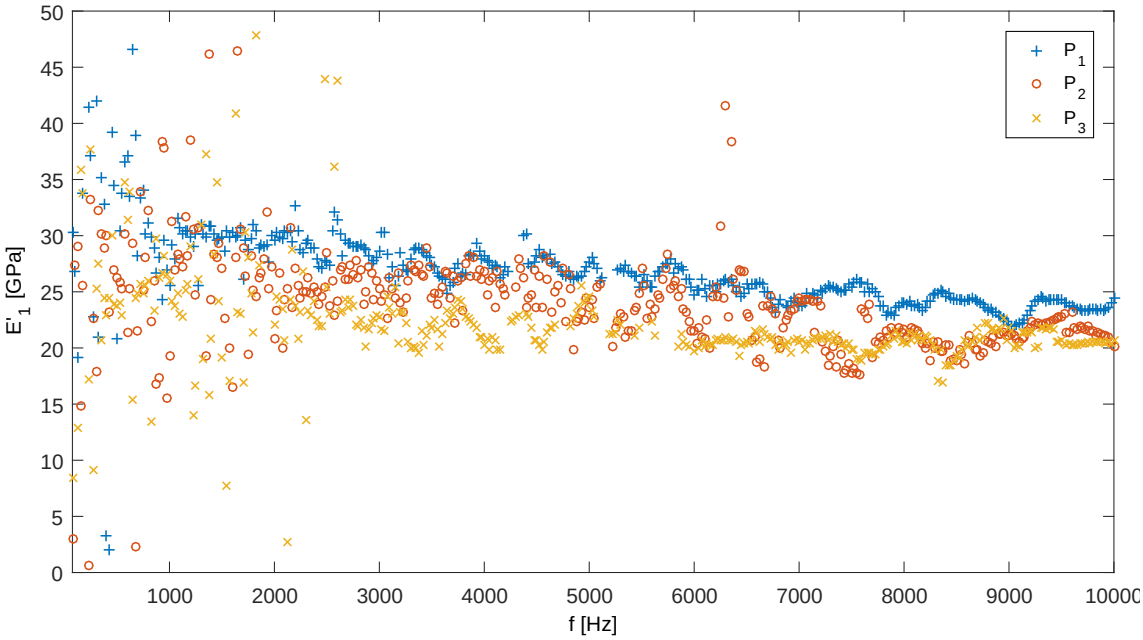

(a) Storage modulus in longitudinal direction.

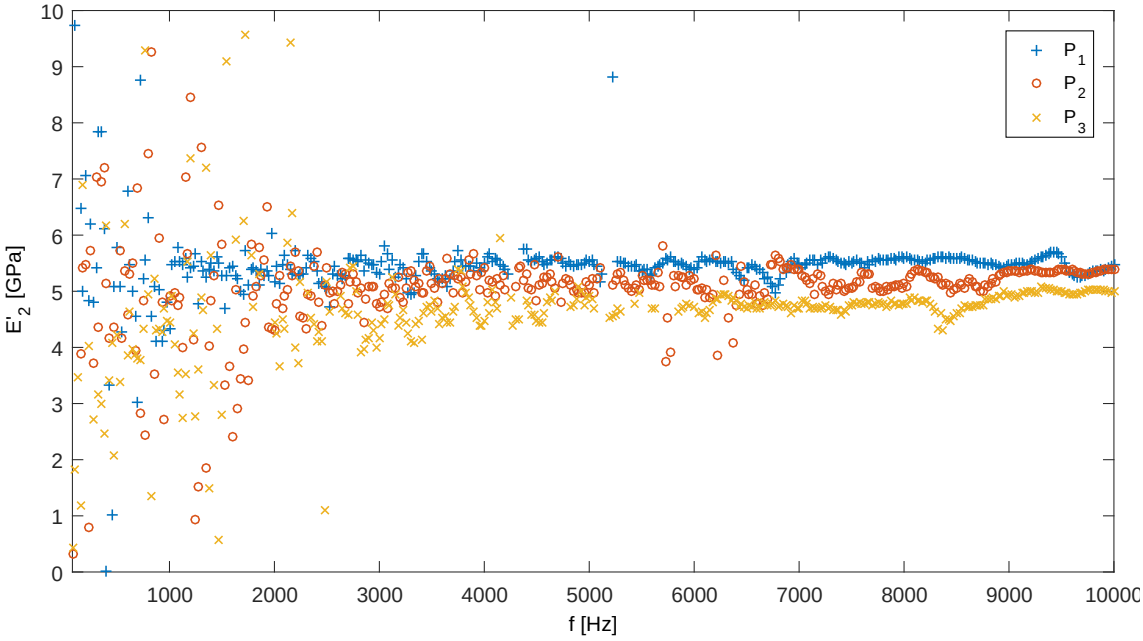

(b) Storage modulus in transverse direction.

Fig. 2.20. Identified storage moduli obtained by vibrometer measurement on the 3 plates.

parameter can be expressed in the form $E_i'(f) = N(\mu, \sigma)$, denoting a normal distribution with a mean μ and a standard deviation σ. Results in frequency domain are shown in Fig. 2.21. It can be observed that a slight decreasing trend of the longitudinal storage modulus (Fig. 2.21(a)) with the frequency and an increasing trend of the transverse one (Fig. 2.21(b)) occur above 4000 Hz. Similar trends are already observed in the results given in the previous works carried out on the inverse method [111, 112]. Therefore, such trends could be related to the method rather than to a real representation of the material behaviour. In particular, the influence of the spatial step Δ between the points of measure is investigated in the next chapter (cf section 3.5). The longitudinal storage modulus decreases from 23 GPa at 2000 Hz to 19 GPa at 10000 Hz (relative decrease of 21 %). The transverse storage modulus values, instead, are identified between 4 GPa and 4.5 GPa (relative increase of 12.5 %). Moreover, a remarkable reduction of the spread occurs with the frequency for both the longitudinal and transverse storage moduli.

2.5.3.2 Loss factor

Mean values of loss factors in longitudinal and transverse directions are shown in Fig. 2.22. Even if the loss factors are identified for each frequency of the domain with mean values of η_1 between 0.02 and 0.15 and η_2 between 0.04 and 0.17, it is difficult to derive a trend. Indeed, as already found in bibliography review [112, 113] and confirmed in the section 3.3 of this work, loss factor is more sensitive to noise than storage modulus and a degradation of the obtained results is observed when data are affected by significant noise level. Actually, the curves are characterized by fluctuations of loss factor mean values for some frequencies. The origin of these fluctuations could be the coupling of the plate vibration with aerodynamic phenomena. In fact, when the excitation frequency is a plate resonance frequency, the air in which the plate is immersed could contribute to increase the damping. In order to confirm this hypothesis, a characterization of the plate frequency-response-function is needed. Such analysis can be performed using the same experimental setup employed for the application of the FAT-based method. Conversely, a slower sinusoidal chirp is needed, which means a duration of excitation longer then 0.04 s, in order to obtain a higher frequency resolution. To state it more explicit, the sinusoidal chirp between 25 Hz and 10000 Hz of a duration of 0.04 s used for the displacement measurements in the FAT-based method application leads to a frequency resolution of 25 Hz. Such a signal is employed in order to avoid the establishment of the steady state conditions and measure the displacement in a transition

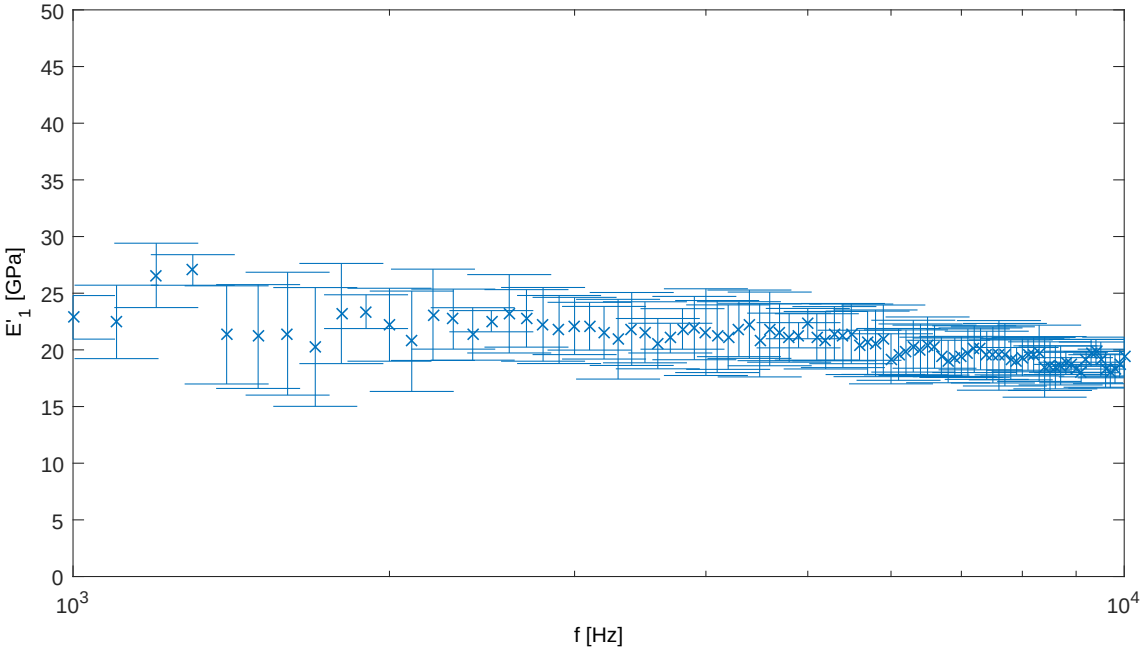

(a) Storage modulus in longitudinal direction.

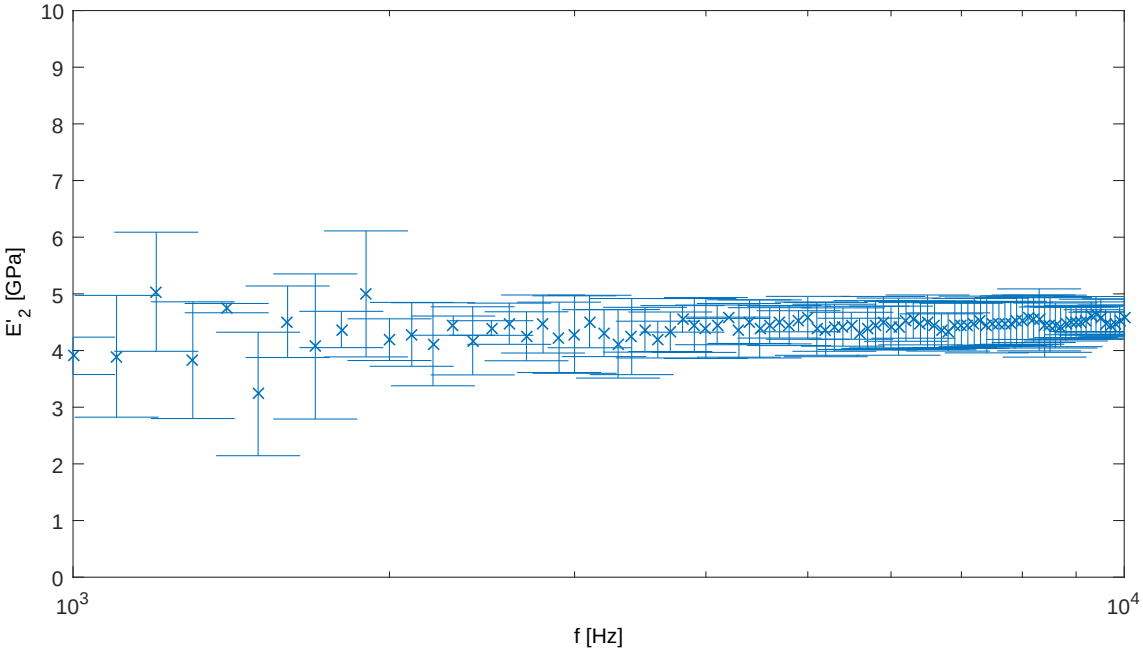

(b) Storage modulus in transverse direction.

Fig. 2.21. Mean and standard deviation of storage moduli obtained on 3 plates by vibrometer with a $\Delta_x = \Delta_y = \Delta = 5\,\text{mm}$.

regime. Conversely, an accurate frequency-response-function requires an higher frequency resolution which can be achieved by a longer duration of excitation. Moreover, observing Fig. 2.22, a wide spread of results occurs for the entire frequency range, confirming a relevant dispersion of the identified loss factor over the 3 tested plate. However, as in the case of the storage moduli, also in this case such a spread decreases with the frequency.

2.5.3.3 Master curve

Dynamic mechanical analysis (DMA) is used to determine the visco-elastic properties of materials. In order to overcome the principal limitation of DMA machines, which are often restricted to low frequencies analysis, the time-temperature superposition principle, according to Williams-Landel-Ferry (WLF) theory [131], is applied. The underlying idea is the direct equivalence between time and temperature influence on the material behaviour. To investigate a frequency domain larger than the frequency fields admissible by the DMA machine, a multi-frequency analysis at different temperatures is performed. For each measurement, the curves of storage modulus E' and the loss factor $\eta = \tan\delta$ are obtained. Then, the time-temperature superposition principle consists of the calculation of the shifting parameters on the basis of which the isothermal curves are shifted toward each other to obtain the storage modulus and loss factor values over a wide range of frequencies at a reference temperature value. The resulting curves of the parameters against the wide frequency range are called master curves.

The tests are conducted by NETZSCH using a NETZSCH-DMA 242 machine. Two specimens of dimensions $50\,\text{mm} \times 10\,\text{mm} \times 2.5\,\text{mm}$ are cut with longitudinal direction parallel and perpendicular to the material fibres, and tested in a 3-point bending configuration. A maximum dynamic force of 9.2 N and a ratio of static force over dynamic one equal to 1.3 are applied to the specimen. A temperature range between $-150\,^{\circ}\text{C}$ et $150\,^{\circ}\text{C}$ is analysed for different values of frequencies between 1 Hz and 10 Hz. The time-temperature superposition is then applied to obtain the so-called master curves for the storage moduli and loss factors.

A direct comparison between storage modulus curves obtained by WLF and those presented in section 2.5.3.1 is shown in Fig. 2.23. A good correlation of results is found for the storage modulus identified in the fibre direction (Fig. 2.23(a)). Indeed, although the decreasing trend obtained by the FAT-based method, the difference between the two curves is limited to 10 % over the frequency range between 2000 Hz and 10 000 Hz. On the contrary, results obtained in the transverse direction

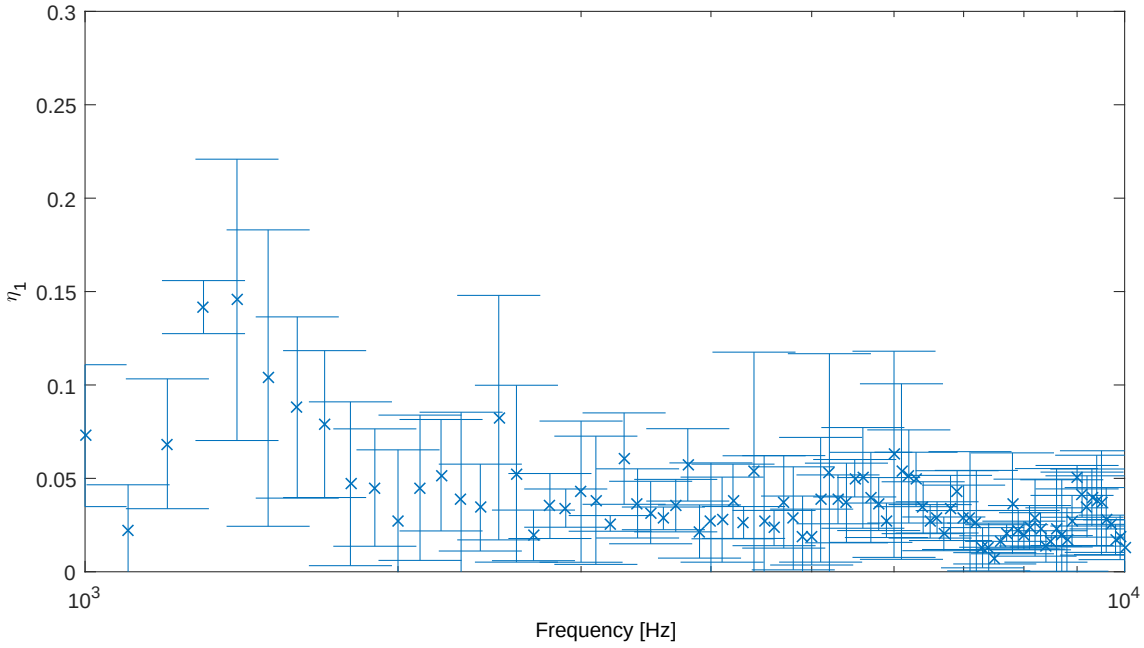

(a) Loss factor in longitudinal direction.

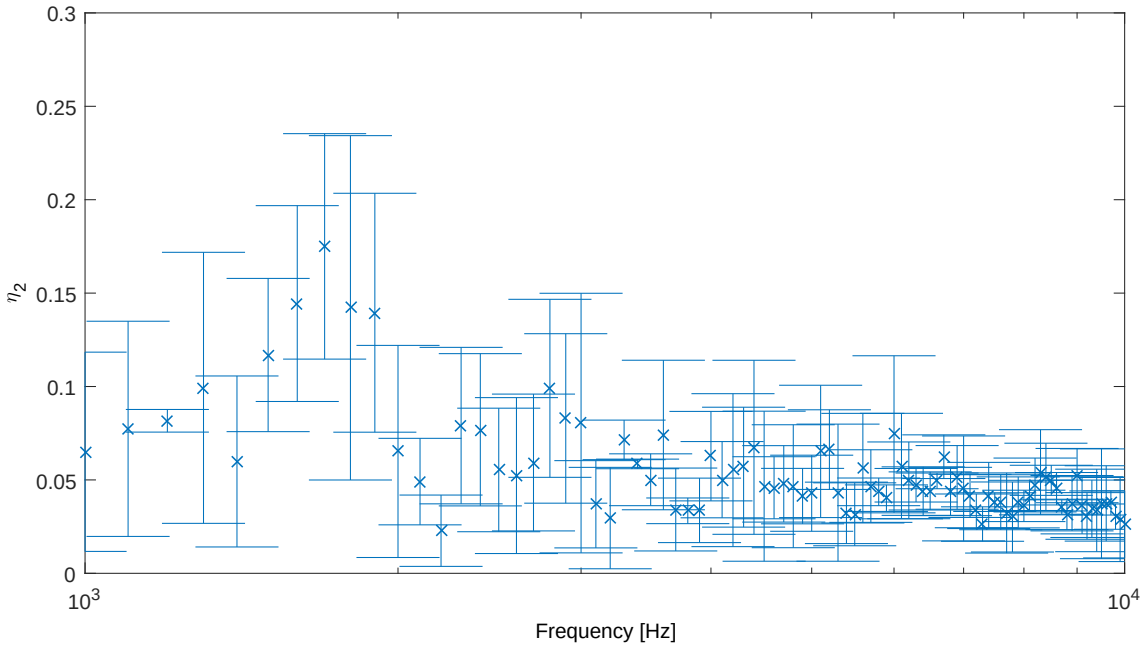

(b) Loss factor in transverse direction.

Fig. 2.22. Mean and standard deviation of loss factors obtained on 3 plates by vibrometer with a $\Delta_x = \Delta_y = 5\,\text{mm}$.

are significantly different (Fig. 2.23(b)). Indeed, in spite of having the same increasing trend, the curves relative to the transverse storage modulus have a constant gap of 35 % over the frequency range. The identified transverse storage modulus by the WLF technique is more similar to the calculated Young modulus by the rule of mixtures (see section 1.2.4). Such a difference could be associated to the DMA specimen dimensions. Indeed, the presence of the flax weft could have a more important impact on the dynamic behaviour of the plate and a limited influence on small specimens as the DMA ones. Fig. 2.24 presents a comparison of the loss factors identified by the FAT-based method and those resulting from the DMA tests. Because of a failure in the application of the time-temperature superposition principle, the DMA test allows to identify the longitudinal loss factor only for frequencies up to 6000 Hz. In order to perform a comparison of results between those obtained by DMA and those obtained by the FAT-based method, an extrapolation of the master curve over the higher frequencies is performed, supposing constant the trend observed between 2000 Hz and 6000 Hz. The extrapolated values are also reported in Fig. 2.24(a) and a good superposition of results can be found also over the frequency range between 6000 Hz and 10 000 Hz. Indeed, values of about 0.02 are found by DMA analysis and by the FAT-based method over this range of frequencies. Furthermore, a good consistence can be observed between loss factor values identified on the transverse direction. Indeed, the same decreasing trend is observed for frequency above 4000 Hz, with values of about 0.04.

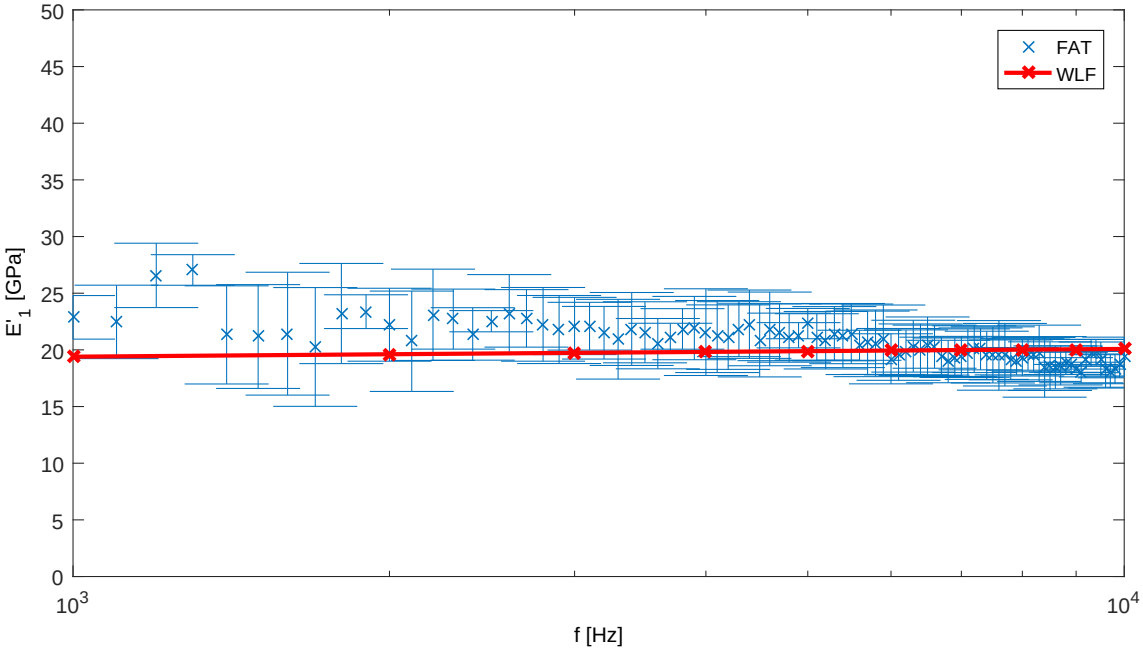

(a) Longitudinal storage modulus

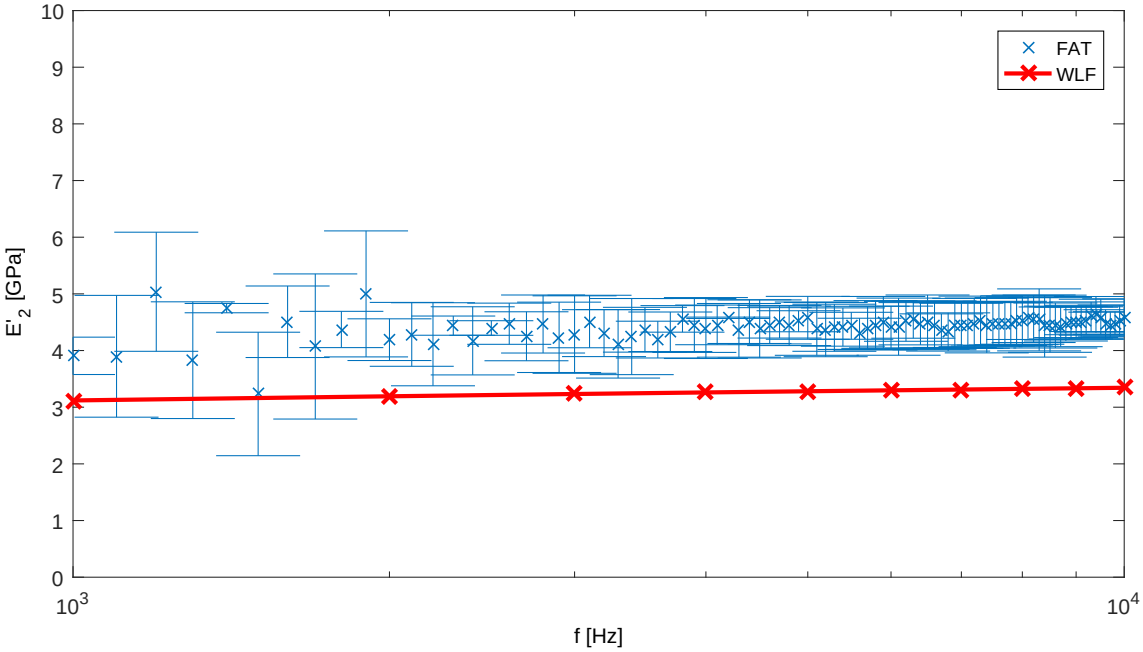

(b) Transverse storage modulus

Fig. 2.23. Comparison of storage moduli identified by the FAT-based method and the WLF principle.

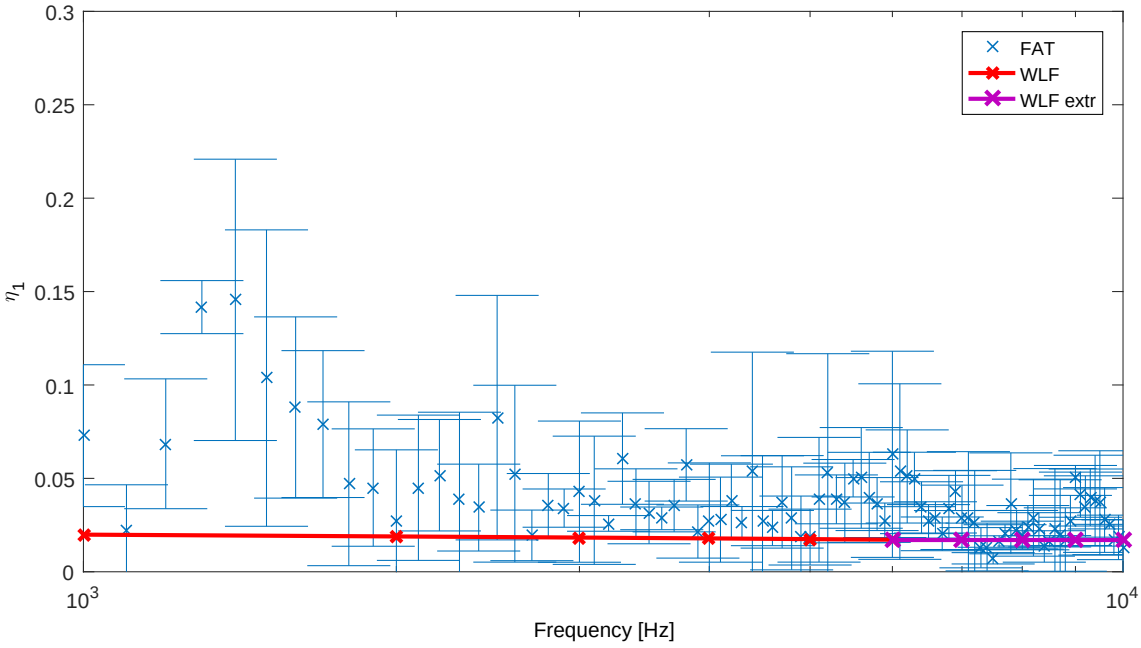

(a) Loss factor in longitudinal direction.

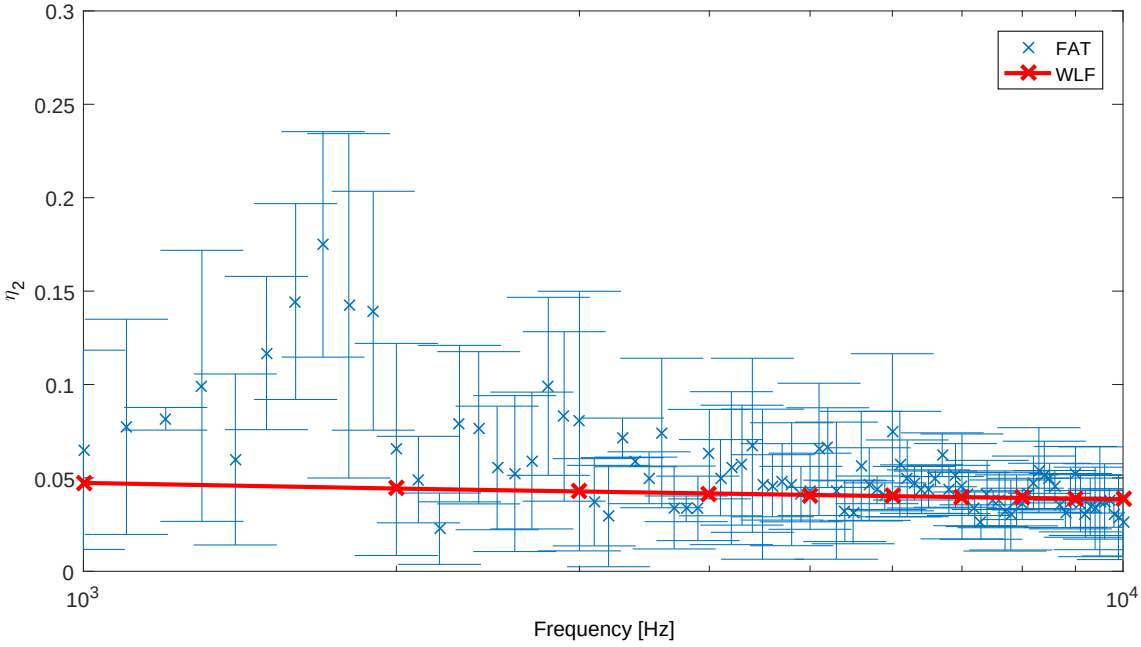

(b) Loss factor in transverse direction.

Fig. 2.24. Comparison of loss factors identified by the FAT-based method and the WLF principle. In violet the extrapolated values.

2.6 Conclusions

This chapter is firstly addressed to a general presentation of the FAT-based method for the dynamic properties identification. The theory underlying the method is presented. In a first stage, digital image correlation, which has the great advantage that the entire field of displacement can be measured at the same time, is applied as measurement technique for the out-of-plane displacement field of a FF/PA11 composite plate. For this purpose, two excitation ways are investigated: the first one is a sinusoidal chirp between 50 Hz and 1000 Hz swept in 1 s and the second one is a sinusoidal chirp between 25 Hz and 10 000 Hz swept in 0.3 s. Nevertheless, the noise affecting the measurement data leads to an important dispersion of the identified parameters, making their identification impossible.

Measurements are then carried out with a laser Doppler vibrometer. In order to validate the method and the measurement technique, the out-of-plane displacement field of a sheet moulding compound composite plate is firstly analysed. In this case a sinusoidal chirp between 25 Hz and 10 000 Hz swept in 0.04 s is used to excite the plate. The measured displacement field as well as the plate thickness and the material density are used as input data of the properties identification method. Results are in agreement with data available in literature about this material, confirming the transversely orthotropic behaviour. The storage modulus calculated in the main directions of the plate is equal to 16 GPa over the entire frequency domain whereas the shear modulus amounts to 2.9 GPa. The results on loss factors are affected by a relevant dispersion for frequencies up to 10 000 Hz. Indeed, as already observed in literature, the loss factor is more affected by measurement noise. The same configuration of excitation and measurement technique are then used to characterize the dynamic behaviour of the flax fibre reinforced PA11. A number of 3 plates are tested and results are compared to characterize the material variability. A significant dispersion is obtained for frequencies below 1000 Hz. Moreover, a decreasing trend of the longitudinal storage modulus is noteworthy, with values going from 23 GPa down to 19 GPa for frequencies between 2000 Hz and 10 000 Hz. A slight increasing trend is instead found for the transverse storage modulus, whose values are between 4 GPa and 4.5 GPa. The curves related to the identified loss factors are affected, as in the case of SMC composite material, by a more important dispersion. Nonetheless, such a dispersion decreases with the frequency for both longitudinal and transverse loss factors. In order to validate such results, a dynamic mechanical analysis is performed on two specimens cut in the directions parallel and perpendicular to the material fibre direction. The

time-temperature superposition principle is applied, according to the WLF theory, to output the storage moduli and loss factors over a wide range of frequencies. The longitudinal storage modulus resulting from the FAT-based method is in line with that obtained by the DMA analysis. On the contrary, the comparison of the identified transverse storage moduli is not satisfying. A discrepancy of 35 % is in fact notable all over the frequency range. Such discrepancy could be due to the dimension of the specimens. Indeed, the weft which characterizes the flax fabric could have a minor impact on a specimens of small dimensions. Even if the WLF curve related to the longitudinal loss factor is identified only for frequencies up to 6000 Hz, a good comparison of loss factor in both longitudinal and transverse directions is obtained.

3

Sensitivity analysis

Contents

3.1 Introduction

In the previous chapter the storage moduli and loss factors of the FF/PA11 are identified on a frequency range between 25 Hz and 10 000 Hz. It is observed that a significant dispersion characterize the results over frequencies below 1000 Hz. Moreover the storage modulus in fibre direction presents a decreasing trend with the frequency, whereas an increasing trend characterizes the storage modulus curve in transverse direction. To better understand such results, a repeatability and reproducibility analysis of the FAT-based method applied to displacement fields measured by Laser Doppler Vibrometer (LDV), is first carried out in this chapter. The repeatability analysis consists of performing measurements on the same specimen, maintaining unchanged the measurement conditions and studying the correlation between the results. The reproducibility analysis, conversely, consists of evaluating the correlation between data resulting from measurements conducted under different conditions.

Moreover, in order to perform a sensitivity analysis of the FAT-based method presented in chapter 2 for the dynamic properties identification, six parameters are taken into account: the noise impacting the measurement data, the filter parameter, the spatial resolution Δ, the size, shape and location on the plane of the area of interest (AOI), corresponding to the area over which the displacement field is measured. An analytical displacement field with or without an artificial noise, is used to investigate the influence of the noise on the FAT-based method results. The low-pass filter applied to the measured data has an important role for the noise reduction and the selection procedure of the filter parameter is therefore investigated. The sensitivity analysis is then addressed to the spatial resolution Δ, defined as the distance between two adjacent points of the measurement grid. Two ways are available to modify this parameter: either experimentally, by defining this distance at the step of the creation of the measurement grid, or numerically, by multiplication of the experimental spatial resolution selecting only one out of two, three, four, etc. points on each row and column of the measurement grid. In this study, two values for the experimental spatial resolution are chosen: 1 mm and 5 mm. The displacement field measured on the fine grid ($\Delta = 1$ mm) is then used to numerically modify the spatial resolution up to $\Delta = 10$ mm. The other parameter analysed in this study is the size of the area of interest, corresponding to the area covered by the abovementioned measurement grid. In a first step, a squared area of interest is considered with the edge dimension varying among 50 mm, 100 mm, 200 mm and 300 mm. Furthermore, an area of dimensions 390 mm $\times$ 330 mm is also considered. A further analysis is

performed on a rectangular area of interest, where the largest dimension is parallel to the fibre direction: tests are performed on an area of dimensions 300 mm × 100 mm. At last, an analysis on the influence of boundary conditions is carried out, considering areas near the edges of the plate.

A total of seven plates, named P1, P2, P3, P4, P5, P6, P7, are tested in three different laboratories: ESTACA'Lab at Saint-Quentin-en-Yvelines (SQY), ESTACA'Lab at Laval (LAV) and Laboratoire d'Acoustique de l'Université du Mans (LAUM). The experimental setup related to each laboratory is detailed in chapter 2. In Table 3.1, the area of interest dimensions as well as the experimental spatial resolution are presented for each configuration. A name is used to include information about the dimensions of the area of interest in x- and y-directions and the value of the spatial resolution. For example, configuration T-300x100-1 corresponds to the displacement measurements performed over an area of dimensions 300 mm in x-direction and 100 mm in y-direction, with a spatial resolution of 1 mm. The presence of the letter D at the end of the name indicates that the measurement grid is not at the centre of the plate but in a location near the boundary conditions. Moreover, the measurement time of each test is also reported. Such a time represents the duration of the measure, at which the calibration time must be added for the calculation of the experimental time. To summarize all the tests performed, Table 3.2 reports for each plate the

Configuration	AOI size [mm^2]	Δ [mm]	Measurement time [min]
T-200x200-1	200 x 200	1	269
T-200x200-5	200 x 200	5	11
T-50x50-5	50 x 50	5	1
T-100x100-5	100 x 100	5	3
T-300x300-5	300 x 300	5	25
T-390x330-5	390 x 330	5	35
T-300x100-5	300 x 100	5	9
T-200x100-5-D	200 x 100	5	6
T-100x100-5-D	100 x 100	5	3

Table 3.1: LDV tests specifications for each test configuration.

laboratory in which the test is performed, as well as the orientation angle and test configuration, the number of tests and the time period. The test conditions are detailed in section 2.5.3.

Plate	Laboratory	Orientation angle	Configuration	Number of tests	Time period
P1	SQY	0°	T-200x200-5	1	July 2017
P2	SQY	0°	T-200x200-5	7	
P3	SQY	0°	T-200x200-5	1	
P4	SQY	90°	T-200x200-5	7	
P5	SQY	90°	T-200x200-5	1	
P6	SQY	90°	T-200x200-5	1	
P7	SQY	90°	T-200x200-5	1	
	LAUM	0°, 90°	T-200x200-5	1	January 2019
	LAV	0°	All configurations listed in Table 3.1	1 for each	

Table 3.2: Summary of the tests conducted for each plate.

3.2 Repeatability and reproducibility of the method

To study the robustness of the method, a repeatability and a reproducibility analysis are performed. The repeatability analysis allows to study the grade of correlation between measurements conducted on the same specimen, keeping unchanged the conditions of measurement (laboratory, instruments, operator...). The reproducibility analysis is performed to identify the grade of correlation between measurements conducted changing one or more conditions of measurement. The displacements are measured by the LDV system on a measurement grid which consists of 1681 points arranged on 41 rows and 41 columns at a distance of 5 mm each other, corresponding to a measured area of dimensions 200 mm $\times$ 200 mm (Test T-200x200-5 in Table 3.1). The displacement field so measured is used as input to the parameter identification method to obtain the storage moduli E_1' and E_2' as well as the loss factors η_1 and η_2 in longitudinal (on fibre) and transverse directions. Given the difficulties to derive a trend of the loss factor from a single test, as shown in the previous chapter, only the storage moduli are presented in the following analysis.

3.2.1 Repeatability

The repeatability analysis is conducted to study the error that could occur performing the same test on the same plate several times. Thus, recalling the experimental procedure, for each repeatability test the plate is set up on the metallic frame, the shaker is fixed at the bottom corner, the displacement field is measured by the LDV, and then the plate is removed from the frame before performing another test. These operations are repeated 7 times for the plates P2 and P4. The

dynamic properties identification method is applied for each measurement thus obtained. For each plate, the longitudinal and transverse moduli are then averaged and the standard deviation is calculated for each frequency. Figs. 3.1(a) and 3.1(b) show the mean values and standard deviation (represented by a vertical line) of respectively the longitudinal and transverse moduli obtained for the repeatability analysis for plate P2, whereas Figs. 3.1(c) and 3.1(d) present the results obtained for plate P4. The longitudinal storage modulus mean values decrease with the frequency for both plates P2 (Figs. 3.1(a)) and P4 (Fig. 3.1(c)) and assumes values between 28 GPa and 18 GPa for plate P2 and 24 GPa and 18 GPa over a frequency range between 2000 Hz and 10 000 Hz. It can be observed that, for frequencies lower than 2000 Hz, the standard deviation assumes greater values than for higher frequencies, which confirms that a strong dispersion characterizes the results below 2000 Hz. A slight increasing trend of the transverse storage modulus E_2' is observed for both plates P2 and P4 (Figs. 3.1(b) and 3.1(d)). Values of the storage modulus in transverse direction for frequencies between 2000 Hz and 10 000 Hz range between 5 GPa and 6 GPa for the plate P2 and between 4 GPa and 5 GPa for the plate P4. Also in the case of transverse storage moduli, the standard deviation assumes larger values for frequencies lower than 2000 Hz. Moreover, a noteworthy reduction of the standard deviation occurs with the increasing frequencies in the case of transverse storage moduli. An average standard deviation of 1.5 GPa is observed on the longitudinal storage modulus over a frequency range between 2000 Hz and 10 000 Hz, whereas it assumes a value of 0.3 GPa in transverse direction. It can be then concluded that an error of approximately 8 % of the storage modulus mean value over the longitudinal direction and 6 % over the transverse one, may be associated to repeatability errors.

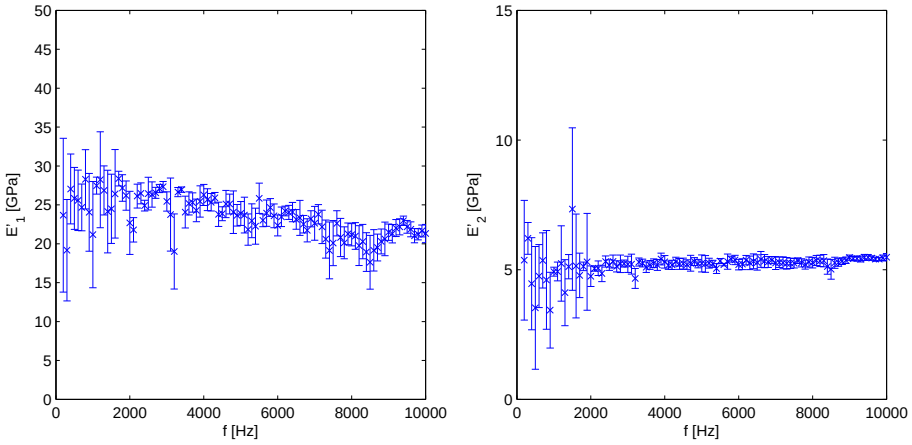

(a) Longitudinal storage modulus (b) Transverse storage modulus

(c) Longitudinal storage modulus (d) Transverse storage modulus

Fig. 3.1. Mean value and standard deviation of the longitudinal and transverse moduli identified over 7 tests performed in SQY on the plates P2 ((a)(b)) and P4 ((c)(d)).

3.2.2 Reproducibility

In order to verify the reproducibility of the identification method, several parameters are changed: the plate orientation, the environmental conditions, the measurement and excitation equipments.

Tests on two different plate orientations are conducted in January 2019 at LAUM, using the experimental setup described in section 2.5.1. T-200x200-5 test is performed on the plate P7 in two different configurations: the plate is firstly suspended with an orientation of 0°, which means that the fibres are parallel to the x-direction of the global frame, and excited in the bottom right corner (Fig. 3.2(a)). Subsequently the plate is rotated by 90° and, keeping the relative position of the excitation point constant in the plate because of the screwing presence, it is excited in the lower left corner (Fig. 3.2(b)). In this case, the dynamic properties calculated in y-direction are relative to the fibre direction (direction 1) and those obtained in x-direction are relative to the transverse direction (direction 2). Storage modulus values in longitudinal and transverse direction

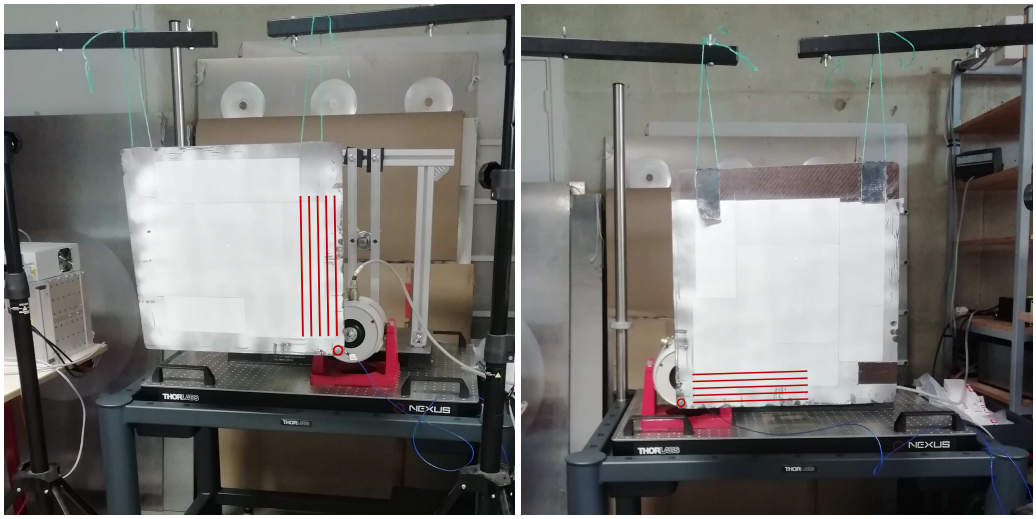

(a) 0° (b) 90°

Fig. 3.2. Two orientation angles tested on the same plate. The fibre orientations and the excitation point are highlighted.

obtained for both configurations of the plate are compared in Fig. 3.3. It can be observed that there is no significant difference between the curves, which leads to assume a good reproducibility of the method with regard to different orientations. In other words, such results confirm that the orientation angle has not an influence on the identified dynamic properties.

Secondly, the influence of environmental conditions and experimental equipments is analysed

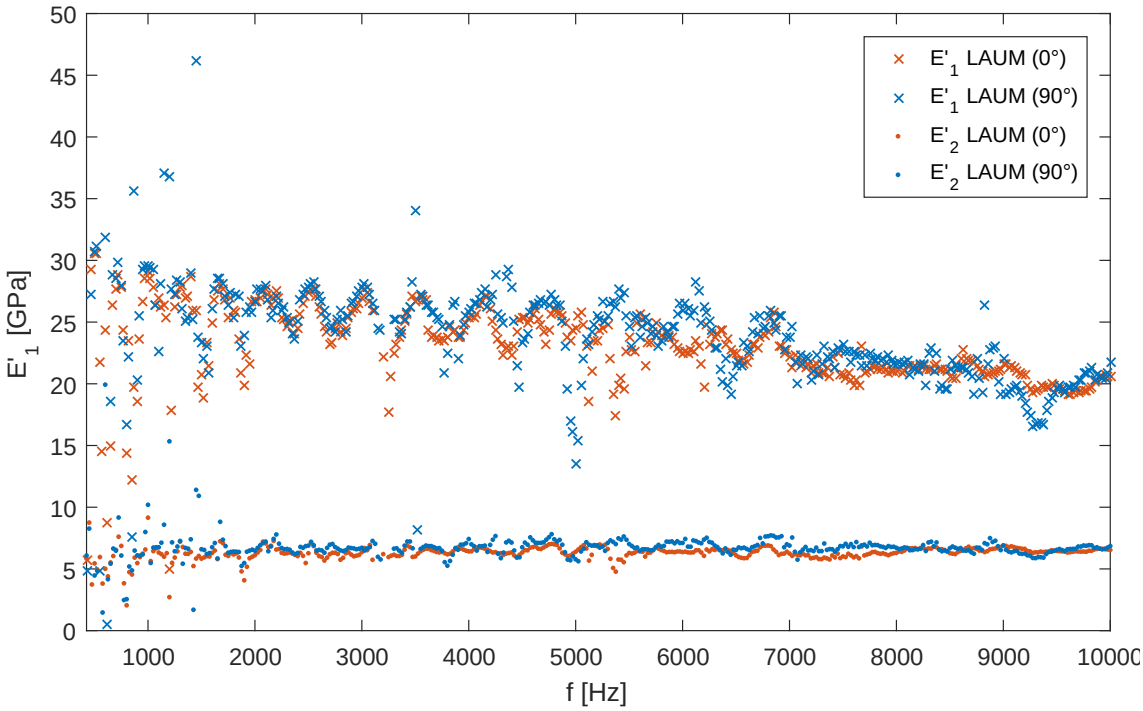

Fig. 3.3. Comparison of results obtained from the displacement fields measured in LAUM (with two orientation angles) and in LAV (at 0°)

by a comparison of results obtained performing the T-200x200-5 test on the plate P7 in different laboratories. The experimental equipments used in each laboratory is detailed in section 2.5.1. Therefore, the dynamic properties obtained by displacement measurements carried out at LAUM, are compared with those resulting by measurements performed in LAV and SQY. As reported in Table 3.2, the measurement campaigns are performed in LAV and LAUM during the month of January 2019, whereas the test in SQY is performed in July 2017. The comparison of results on storage moduli are shown in Fig. 3.4. As can be noted, a good superposition is obtained for the longitudinal storage modulus identified by the different tests (Fig. 3.4(a)). Indeed, the slight discrepancy between the identified values can be associated to the repeatability errors, being lower than 2 GPa. Nevertheless, an important discrepancy can be observed between results related to the transverse direction (Fig. 3.4(b)). Indeed, although the curves obtained by tests performed in LAV and LAUM are quite well superposed, an important gap is observed for the results obtained in SQY. The identified transverse storage modulus values obtained during the campaign carried out in SQY are indeed 1.2 GPa lower than those obtained in LAUM and LAV. Such a gap corresponding to the 30 % of the transverse modulus mean value can be associated to a hardening of the PA11 polymer. Indeed, during an intervening period of more than one year, phenomena related to the ageing could

occur. This assumption is confirmed by the quasi-static tensile tests. Indeed, as shown in chapter 1, an increase of 36 % of the transverse Young's modulus between the data of quasi-static tensile test obtained in June 2017 and those obtained in February 2019.

In order to characterize the material variability, tests on different plates are performed in July 2017, in SQY, keeping unchanged the excitation and measurement equipments. The test configuration is T-200x200-5 (cf. Table 3.1) and plates P1, P2, P3 have the fibres aligned to the x-direction (orientation angle 0°) whereas plates P4, P5, P6 and P7 have fibres aligned in the y-direction (orientation angle 90°) The identified longitudinal and transverse storage moduli are reported respectively in Figs. 3.5(a) and 3.5(b) for plate P1, P2, P3, P4, P5, P6 and P7. All the curves relative to the longitudinal storage modulus E_1' are in a range of values between 30 GPa and 20 GPa and are characterized by a downward trend of about 0.1 % (0.001 GPa$\,$Hz^{-1}) with the increased frequencies. Similarly, the transverse storage modulus E_2' curves are in a limited range of values close to 5 GPa and present a rather constant trend with the frequency. A distinction can not be made on the basis of the testing orientation angle on all the plates, neither for the longitudinal storage modulus nor for the transverse storage modulus. Such a result confirm that the dynamic properties identification method is not dependent of the plate orientation. Nevertheless, observing Fig. 3.5(a) and 3.5(b) it is noted that two groups of plates can be distinguished. Indeed, P1, P2 and P7 have similar values of storage moduli and slightly higher than those related to the other plates. Such discrepancy could be associated to the material variability.

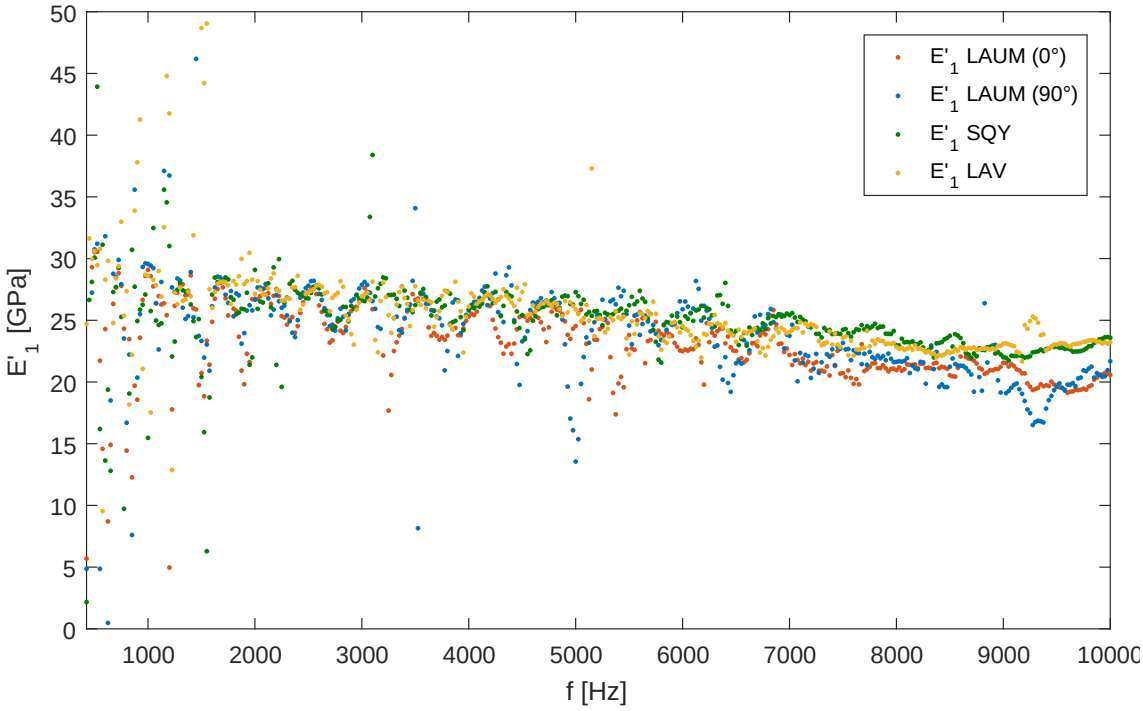

(a) Longitudinal modulus

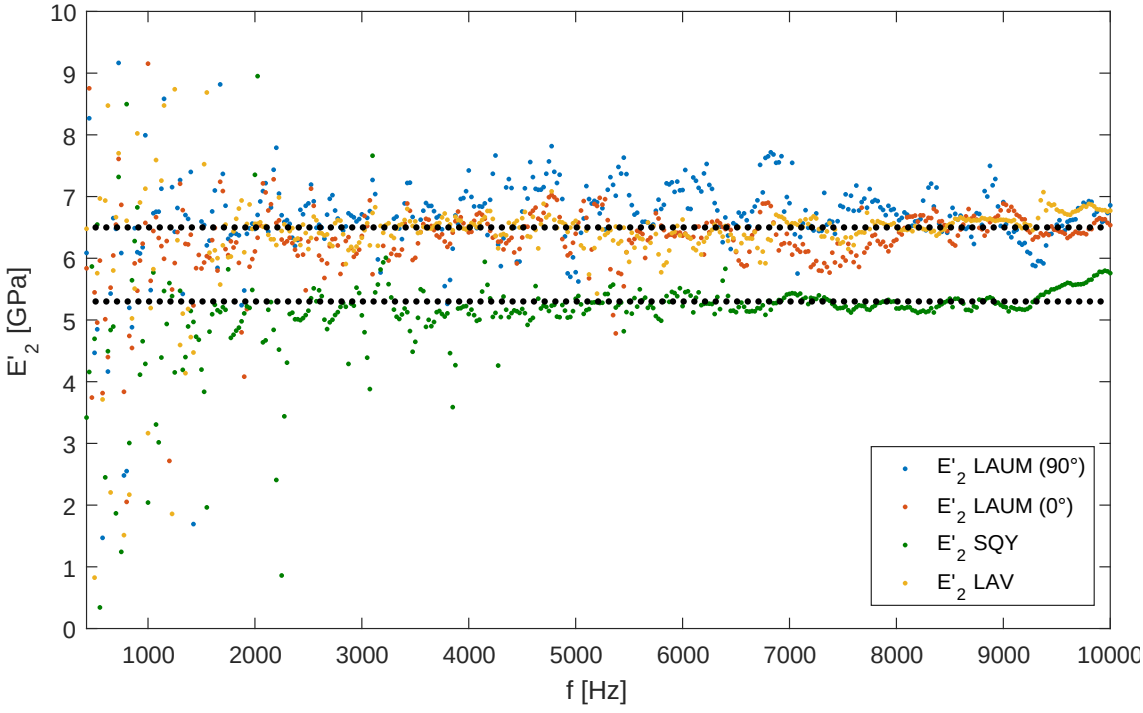

(b) Transverse modulus

Fig. 3.4. Storage modulus values obtained from the T-200x200-5 tests performed in LAV, in SQY and LAUM laboratories on plate P7. Mean values are reported with dotted black lines.

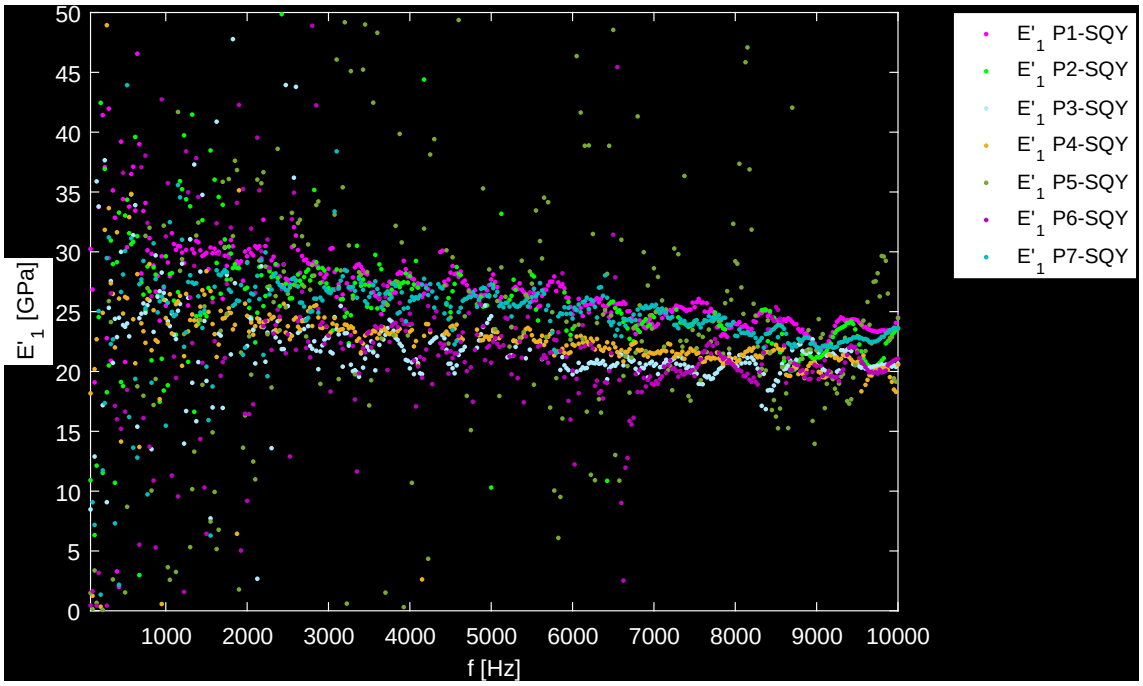

(a) Longitudinal modulus

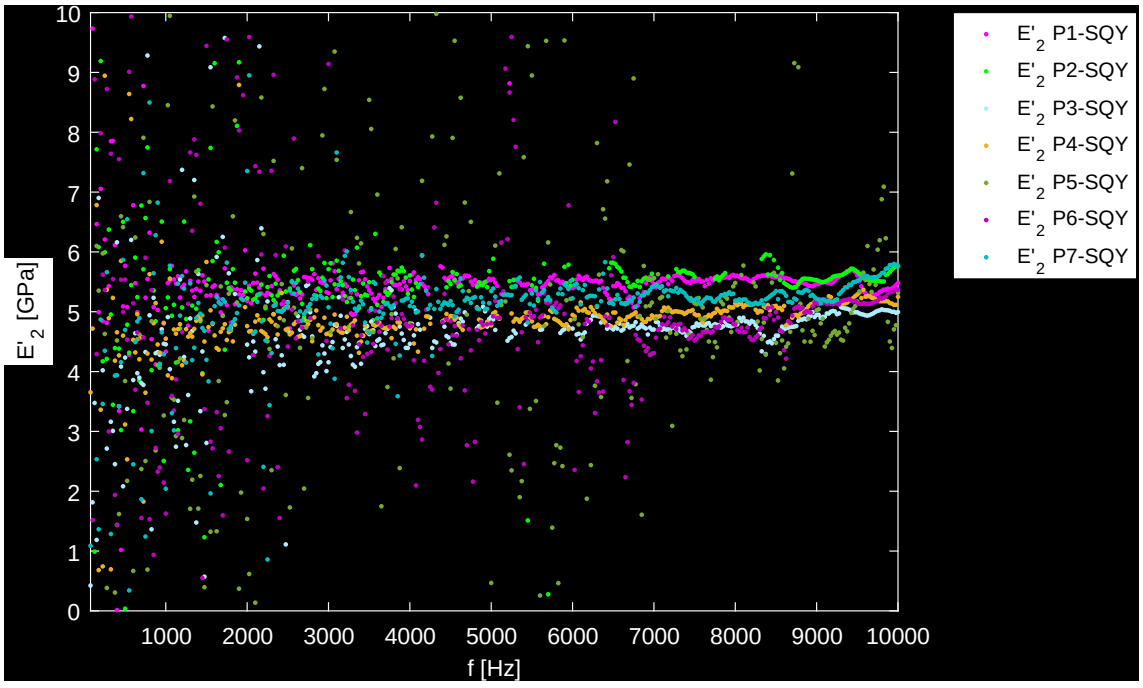

(b) Transverse modulus

Fig. 3.5. Longitudinal (a) and transverse (b) storage moduli identified on 7 plates with different orientation in T-200x200-5 configuration (Tests carried out in SQY).

3.3 Noise influence on parameter identification

In order to verify the influence of the noise affecting the displacement measurements, a study on several levels of noise applied to an analytical displacement field is carried out. For this purpose, a plate supported on its edges is considered, as the analytical expressions of the vibration modes are available for such boundary conditions. Taking into account the local equation of motion of a thin orthotropic plate (Eq. 2.1) and assuming that the plate is excited by a concentrated force F_0 applied AT the point (x_0,y_0), a modal analysis leads to the analytical solution presented in Eq. 3.1 [111].

$$w(x,y,\omega) = \sum_{m=1}^{M}\sum_{n=1}^{N} \frac{4F_0}{L_a L_b \rho h} \frac{\Phi_{mn}(x,y)\Phi_{mn}(x_0,y_0)}{(\omega_{m,n}^2 - \omega^2)} \tag{3.1}$$

where M and N are chosen in such a way as to cover the entire range of frequencies of interest and Φ_{mn} are the modal shapes of a supported plate and $\omega_{m,n}$ the natural frequencies, defined respectively by Eqs. 3.2 and 3.3.

$$\Phi_{mn}(x,y) = \sin\left(\frac{m\pi x}{L_a}\right)\sin\left(\frac{n\pi y}{L_b}\right) \tag{3.2}$$

$$\omega_{m,n} = \pi^2 \sqrt{\frac{1}{\rho h}\left(D_1\left(\frac{m}{L_a}\right)^4 + (D_2+D_4)\left(\frac{mn}{L_a L_b}\right)^2 + D_3\left(\frac{n}{L_b}\right)^4\right)} \tag{3.3}$$

The analytical displacement field calculation is performed for a plate of dimensions L_a = 460 mm and L_b = 500 mm, thickness h = 2.5 mm and material density ρ = 1220 kg m^{-3} over a range of frequencies between 25 Hz and 10 000 Hz. The input storage moduli ($E'_{1,ref}$ and $E'_{2,ref}$) and loss factors ($\eta_{1,ref}$ and $\eta_{2,ref}$) for both fibre and transverse directions are given in Table 3.3 whereas the spatial resolution Δ is chosen equal to 5 mm. Only the displacement field in the centre of the plate over an area of dimensions 200 mm × 200 mm is considered for the identification. In order

Property	Value
$E'_{1,ref}$	25 GPa
$E'_{2,ref}$	5 GPa
$\eta_{1,ref}$	0.03
$\eta_{2,ref}$	0.04

Table 3.3: Input material parameters for the calculation of the analytical displacement field.

to simulate the noise affecting the displacement measurement, a random component, expressed in

Eq. 3.4, is added to the analytical displacement field defined in Eq. 3.1.

$$w_{noisy}(x,y,\omega) = w(x,y,\omega) + \Delta_A(x,y,\omega)e^{j\Delta_\phi(x,y,\omega)} \tag{3.4}$$

where the component Δ_A simulates uncertainties on the amplitude of the displacement measurement and is chosen from a Gaussian distribution with mean zero and standard deviation in such a way that the desired signal-to-noise ratio (SNR) is obtained, and Δ_ϕ acts as uncertainties on the phase of the displacement field and is chosen from a uniform distribution between 0 rad and 2π rad. The abovementioned signal-to-noise ratio is defined by Eq. 3.5.

$$SNR = 20log_{10}\frac{\sum|w(x,y,\omega)|^2}{\sum|w_{noisy}(x,y,\omega) - w(x,y,\omega)|^2} \tag{3.5}$$

It is noteworthy from Eq. 3.5 that lower values of SNR correspond to higher uncertainty values.

In order to study the influence of the noise affecting the displacement measurement on the results of the FAT-based method, three displacement fields used to obtain storage moduli and loss factors are compared: an analytical displacement without noise and two others affected by noise corresponding to SNR of 50 dB and 5 dB. The resulting curves are presented in Figs. 3.6, 3.7 and 3.8 for respectively non noisy data, data affected by a SNR of 50 dB and data affected by a SNR of 5 dB. As can be observed in Fig. 3.6, the storage modulus and loss factor values are identified over the range of frequencies between 25 Hz and 10 000 Hz and correspond to the values used as input: 25 GPa and 5 GPa for the storage moduli and 0.03 and 0.04 for the loss factors in the fibre and transverse directions respectively. However, a slight increasing trend of the storage moduli with the frequency is observed. Such a trend is already observed in literature results on analytical displacement field [111, 112]. Storage moduli and loss factors are also identified by the FAT-based method using a noisy displacement field characterized by a SNR of 50 dB (Fig. 3.7). However, the effect of the noise can clearly be observed at frequencies below 3000 Hz for which an important dispersion affects results and makes the parameter identification not possible. At frequencies higher than 3000 Hz, storage moduli are well identified even if the curves are characterized by fluctuations. Such fluctuations characterize the evolution of loss factors. In particular the loss factor values in the transverse direction are very similar to those used as input whereas an important discrepancy between the input values and the identified ones is evident for data related to the longitudinal direction. In Fig. 3.8, the results obtained by the identification method from

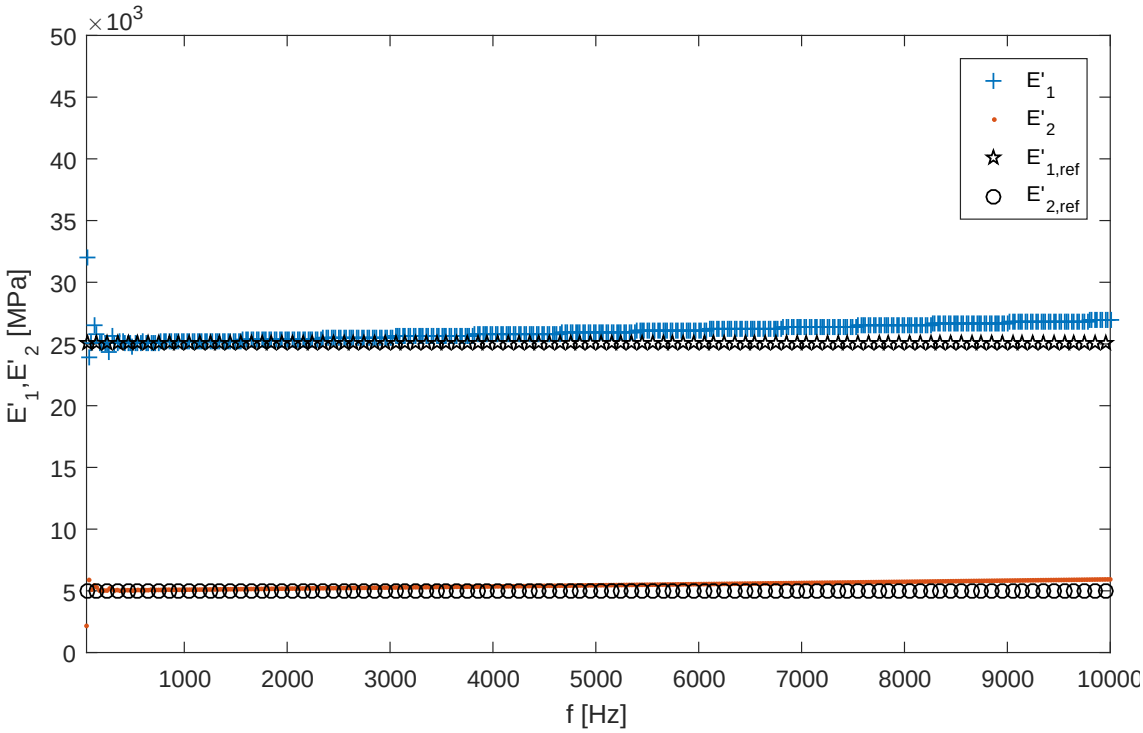

(a) Storage moduli

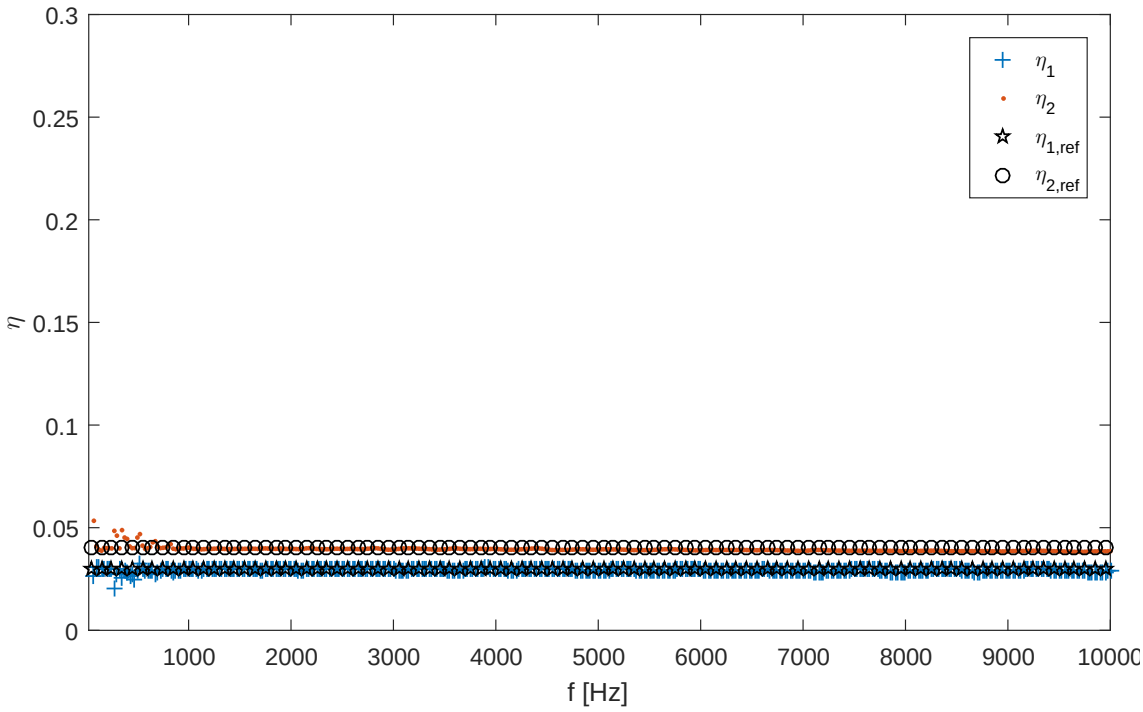

(b) Loss factors

Fig. 3.6. Identified results using an analytical displacement field without noise.

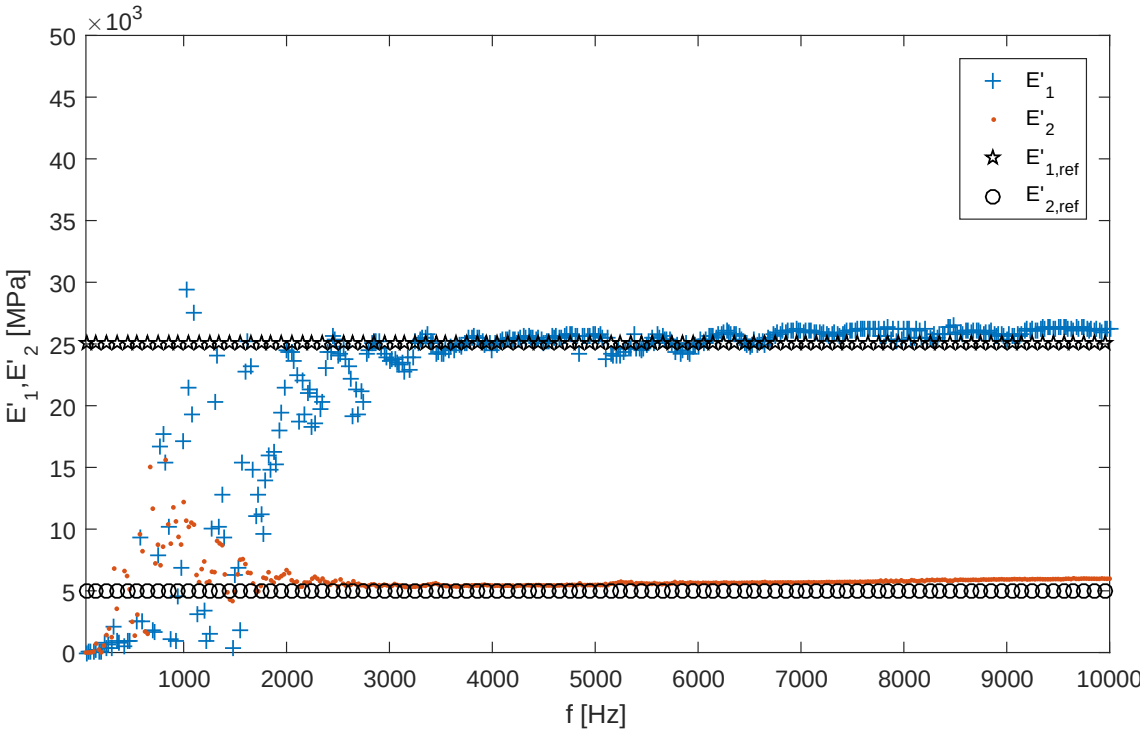

(a) Storage moduli

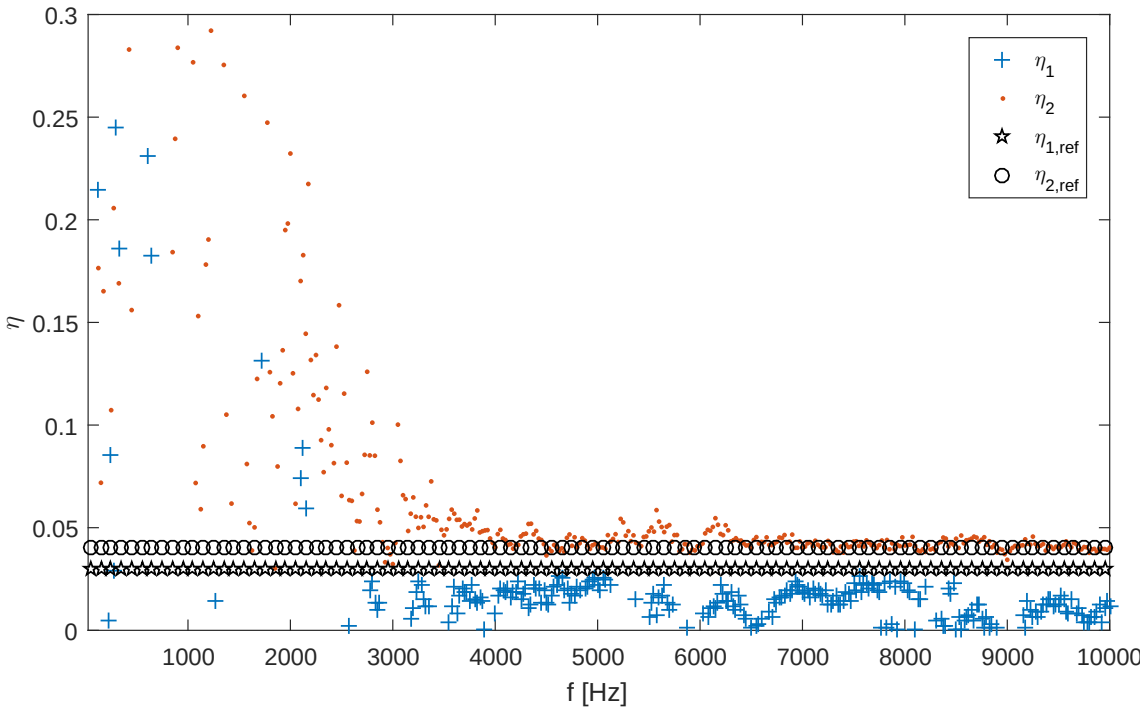

(b) Loss factors

Fig. 3.7. Identified results using an analytical displacement field, SNR=50 dB.

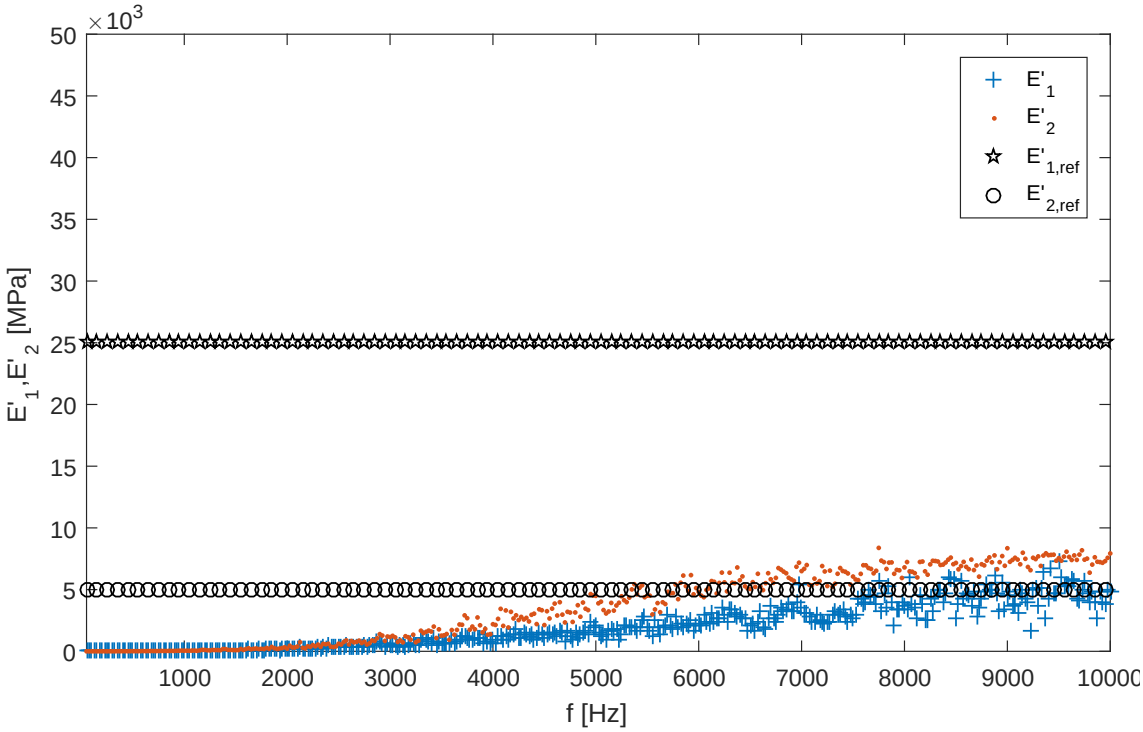

(a) Storage moduli

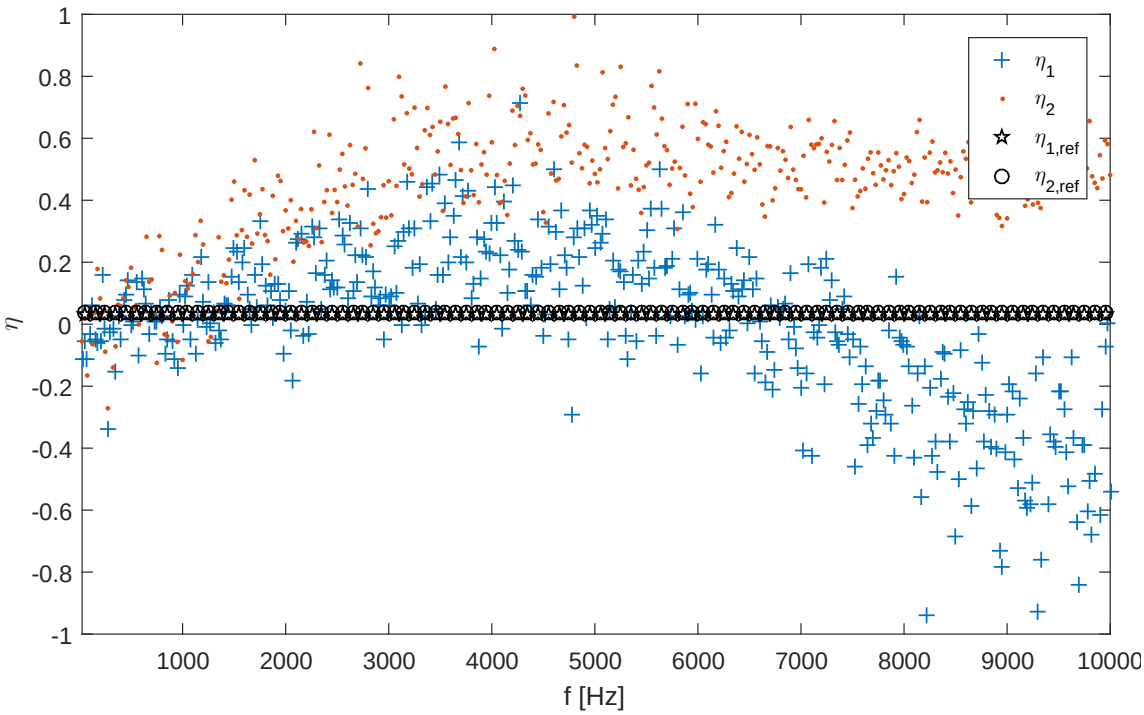

(b) Loss factors

Fig. 3.8. Identified results using an analytical displacement field, SNR = 5 dB.

the analytical displacement field affected by noise such as the SNR is 5 dB, are presented. It can be observed that neither storage moduli nor loss factors can be identified in this case. These observations lead to affirm that an important level of noise on the displacement field measurements, corresponding to a low value of SNR, could affect the FAT-based method results. A good selection of the filter is then important. For this purpose, section 3.4 addresses an analysis of the filter parameter selection. However, even if the displacement field is not affected by noise, an increasing trend of the identified storage moduli is observed. Such observation is the focus of the analysis presented in the following sections.

3.4 Choice of the optimum filter parameter

A further crucial step in the dynamic properties identification technique is the application of the low-pass filter. The effect of the parameter k_c can be observed in Fig. 3.9 as proposed in [111]. Here, the real part of the displacement field $w_{i,j}$ obtained by the T-200x200-5 test on the plate P7 is plotted against the two partial derivatives $\delta^{4x}_{i,j}$ and $\delta^{4y}_{i,j}$ for a frequency f = 5450 Hz (cf Eq. 2.7). According to Eq. 2.7, a linear relationship links the displacement field and its derivatives, so the points should lie on a straight line for each frequency. It can be observed that for small values of k_c (e.g. $k_c = 20\,\mathrm{m}^{-1}$), the filter removes too many points, making the dynamic properties difficult to identify. As k_c gradually increases, the points are aligned on a straight line, i.e. for $k_c = 40\,\mathrm{m}^{-1}$. A further increase of k_c leads to a lost of the filter effectiveness. In fact, for values of k_c higher then $100\,\mathrm{m}^{-1}$ a strong dispersion can be noted. This analysis depends on the frequency and therefore, k_c should also depend on the frequency. Based on similar plots, a selection of the optimal value of k_c can be made, leading to a dependence of $k_c(f)$. Then, k_c values related to the entire frequency range are interpolated. Results of the manual selection of k_c are shown in Fig. 3.10 for $\Delta = 5\,\mathrm{mm}$. As introduced in section 2.3.3, an automatic selection of the parameter k_c can be made. A criterion based on the residuals values $\mathfrak{R}$ is presented in [111] and implemented in the algorithm shown in section 2.3.4. Indeed, solutions of Eq. 2.7 are calculated for different values of k_c iterated over a range between $10\,\mathrm{m}^{-1}$ and $200\,\mathrm{m}^{-1}$, and for each solution the residuals are also evaluated. The derivative of the residuals $\mathfrak{R}$, i.e. D($\mathfrak{R}$), with respect to k_c is then calculated. As seen in Fig. 3.9, the optimal k_c is the maximum value for which a linear relation between the displacement field and its partial derivatives could be assumed. When this assumption can no longer be considered

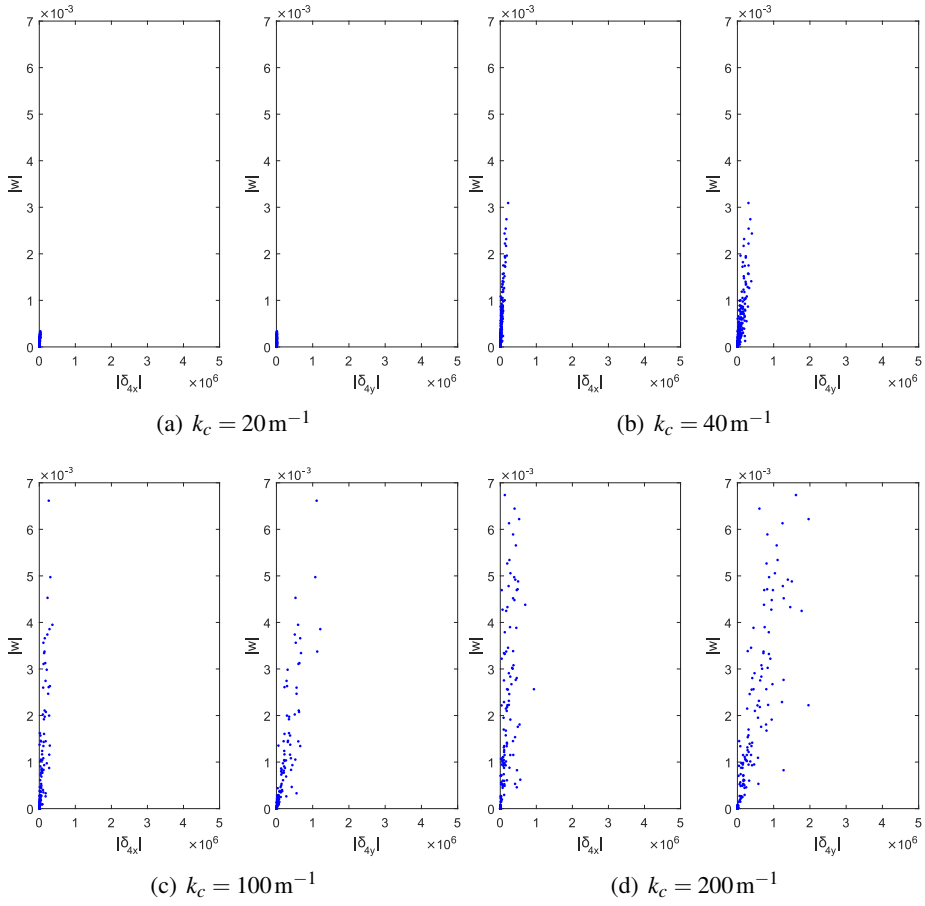

(a) $k_c = 20\,\mathrm{m}^{-1}$ (b) $k_c = 40\,\mathrm{m}^{-1}$

(c) $k_c = 100\,\mathrm{m}^{-1}$ (d) $k_c = 200\,\mathrm{m}^{-1}$

Fig. 3.9. Displacement field $w_{i,j}$ against partial derivatives δ^{4x} and δ^{4y} for different values of k_c, f = 5450 Hz.

valid, the residuals related to the solution increase rapidly up to a maximum. Therefore, the derivative D($\Re$) follows an increasing trend when $\Re$ grows and then drops when $\Re$ reaches the maximum. The value of k_c automatically selected by the algorithm is the one corresponding to a threshold defined as a percentage of the maximum value of D($\Re$). For a comparison with results obtained by a manual selection of the optimum k_c, the curves obtained by an automatic selection are also shown in Fig. 3.10. As it is noticeable in Fig. 3.10(a) the identified storage moduli in fibre and transverse direction obtained by an automatic selection of the filter parameter are comparable with those resulting from the manual selection of such a parameter. Nevertheless, it can be observed that especially for frequency higher than 7500 Hz a slight discrepancy occurs in the case of longitudinal moduli E_1'. Moreover, a comparison of the k_c filter parameter values can be observed in Fig. 3.10(b). The k_c values manually selected are reported with a $\circ$ marker. Such values are interpolated over the entire frequency range obtaining the curve represented with a

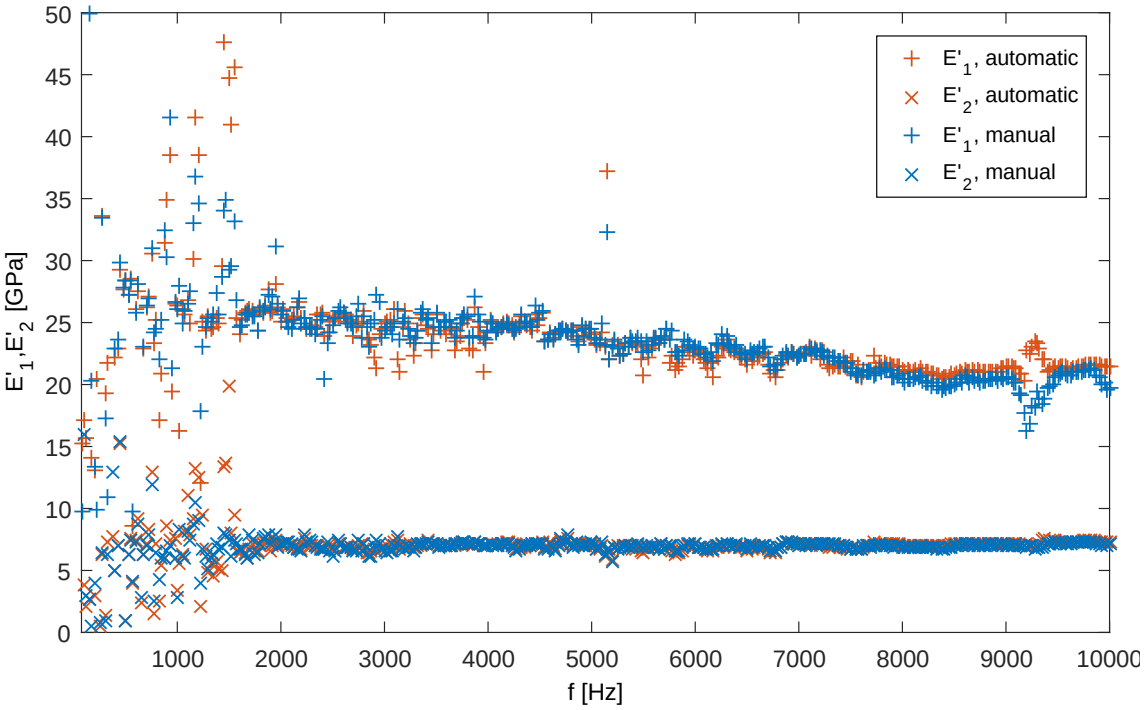

(a) Identified storage moduli by manual selection of k_c, $\Delta = 5\,\text{mm}$

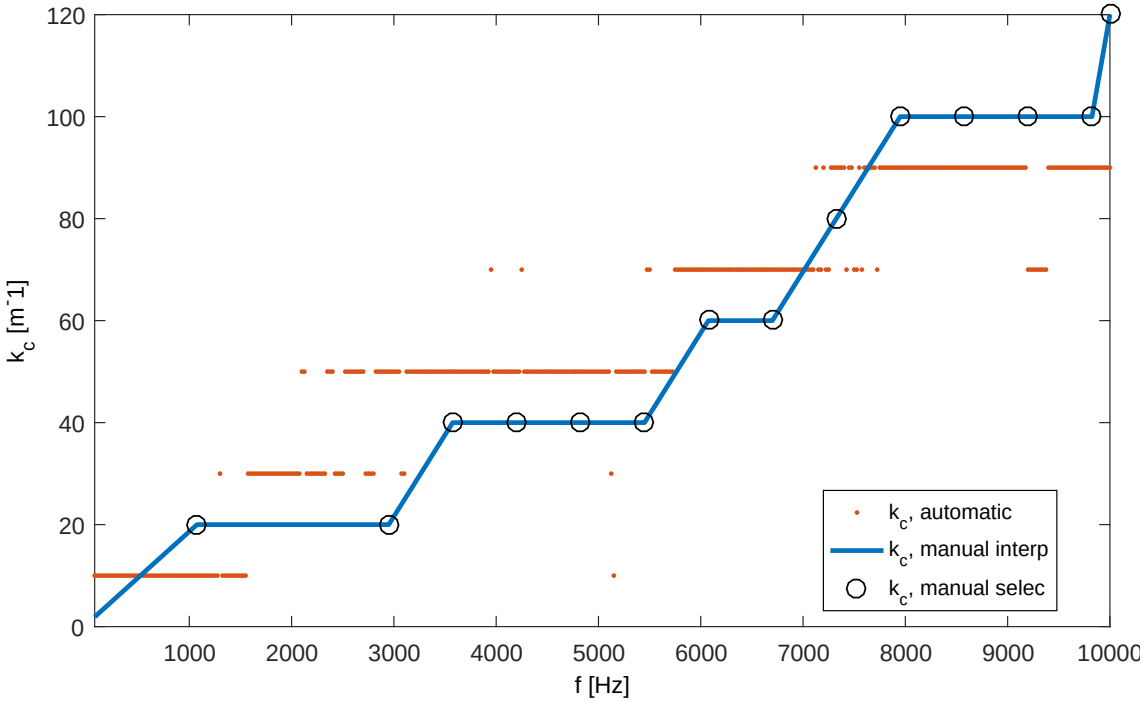

(b) Selected values of k_c (○), interpolated values over the entire range of frequencies (blue line) and k_c values resulting by the automatic selection (orange)

Fig. 3.10. Results of the manual selection of k_c for displacement field with a spatial resolution of 5 mm.

blue line. It can be observed that a gap between the interpolated k_c values and those automatically selected by the algorithm represented by the orange dotted line, appears all over the frequency range. Nevertheless, the obtained storage moduli E_1' and E_2' observed in Fig. 3.10(a) are quite comparable.

3.5 Influence of spatial resolution

An increasing trend of the storage moduli with the frequency also in case of non noisy displacement field is highlighted in Fig. 3.6. Moreover, similar trends have also been noted in previous studies for the identification of material dynamic properties by the FAT-based method using analytical and experimental data. In particular, an increasing trend of the storage modulus with the frequency is found in [111] while a decreasing trend of the flexural stiffness is noticeable in [112]. In order to understand the cause of such trends, a study on the spatial resolution used in the displacement measurements is carried out.

3.5.1 Analytical study

A displacement field analytically obtained by Eq. 3.1 and not affected by noise is firstly used. The input parameters are the same as the ones used in section 3.3, whereas the spatial resolution Δ is chosen equal to 3 mm as a reference value. To verify the influence of the spatial resolution on the identified storage moduli, results of the FAT-based method using analytical displacement field with Δ equal to 3 mm, 6 mm and 9 mm, are respectively shown in Fig. 3.11. As can be observed, an increasing trend occurs with the increase of the value of Δ. Such trend could be related to a wrong sampling of the signal, e.g. spatial aliasing which occurs at high frequency. Indeed, at high frequencies, the plate vibration wavelength is small. Thus, as it is noticeable in Fig. 3.12 where a theoretical non noisy signal is plotted with a red curve, if the spatial resolution Δ represented by the distance between two points is too large, the measured signal, in black, has a wavelength larger then that of the real signal. Moreover, for equivalent frequency, larger wavelengths are associated to material with a higher stiffness. It is important to highlight that such results are obtained on a non noisy displacement field. Indeed, in order to avoid spatial aliasing in case of non noisy data, small values of Δ are always preferable. Moreover, this leads to a better approximation of the derivatives. However, when using noisy data, the increase of the spatial resolution could also act

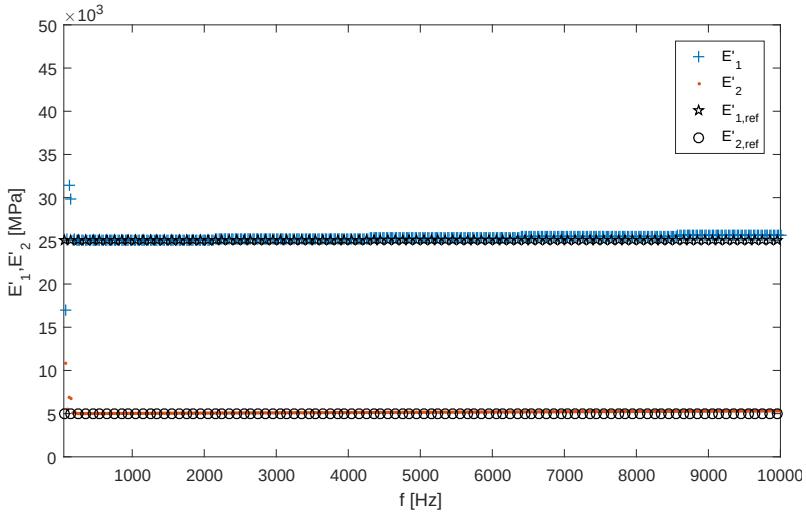

(a) $\Delta = 3\,\text{mm}$

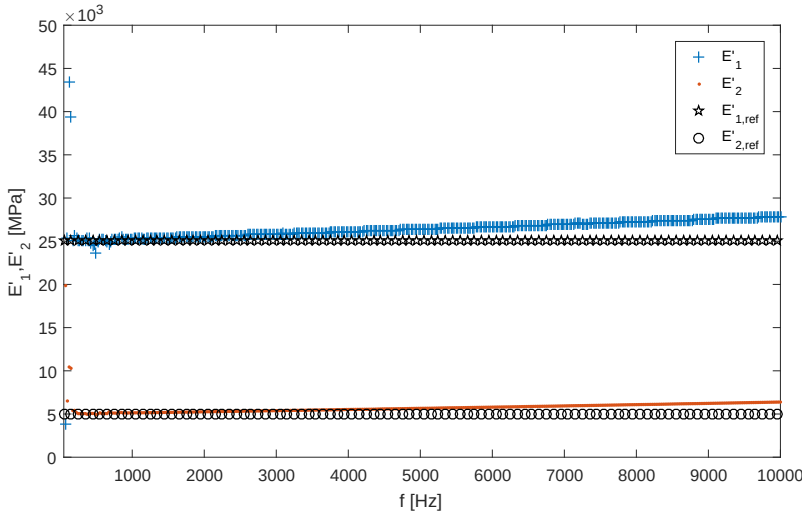

(b) $\Delta = 6\,\text{mm}$

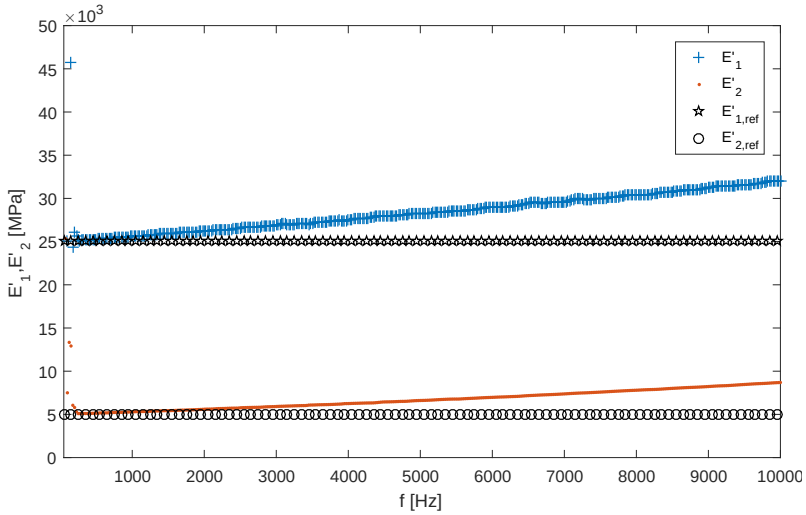

(c) $\Delta = 9\,\text{mm}$

Fig. 3.11. Storage moduli identified using an analytical displacement field, for different values of Δ.

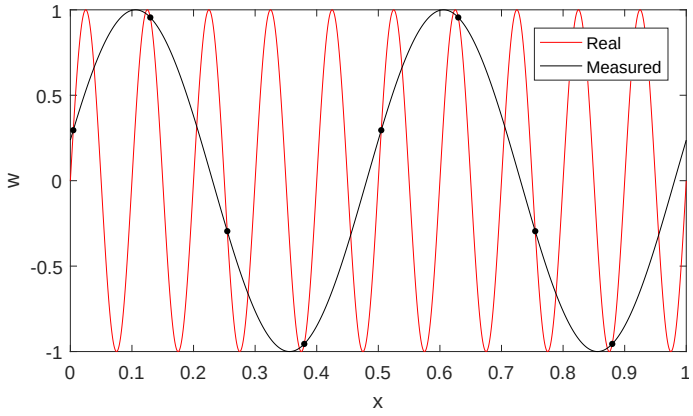

Fig. 3.12. Spatial aliasing leads to measured signals with a wavelength larger then the real one. Dimensions are normalized.

as a low pass filter and too small values of Δ lead to an amplification of the noise in the calculation of the partial derivatives.

An optimum spatial resolution needs therefore to be found. The optimum step value has to be large enough to improve the effect of a low-pass filter but has to meet the sampling requirement of at least 5 points each wave.

3.5.2 Experimental variation

In order to take into account the noise impacting on measured data, an experimental investigation is carried out on the influence of the spatial resolution Δ. Such a parameter is fixed during the definition of the measurement grid on the area of interest (Fig. 2.7). Indeed, for a given area over which the measurement is performed, it is possible to choose the number of points in both x- and y-directions. In this study, two values of the experimental spatial resolution are chosen, i.e. 1 mm and 5 mm. Two different tests are then conducted measuring the out-of-plane displacements on the same area of interest having dimensions 200 mm $\times$ 200 mm at the centre of the vibrating plate. A number of 1481 points is firstly chosen leading to a spatial resolution of 5 mm (corresponding to the test T-200x200-5). A number of 40401 points is then chosen to perform the test T-200x200-1 with an experimental spatial resolution of 1 mm. It is worth noting that such a test leads to a relevant increase of the test duration, which goes from about 11 min to almost 5 h (cf Table 3.1). The comparison of the obtained results on the longitudinal and transverse storage moduli is presented in Fig. 3.13. As it can be noted, the identified storage modulus in the longitudinal direction is more

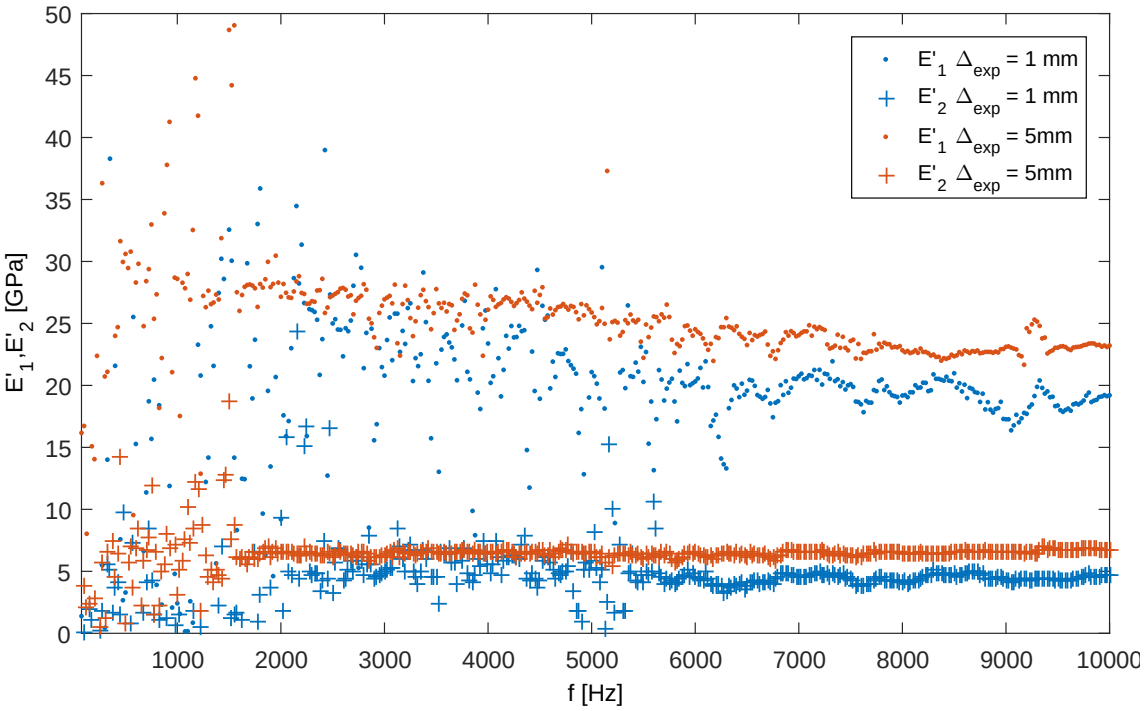

Fig. 3.13. Comparison of results obtained from T-200x200-1 and T-200x200-5 tests.

dispersed in case of T-200x200-1 test than in case of T-200x200-5 test, especially for frequencies below 6000 Hz. Such a dispersion is less pronounced for frequencies above 6000 Hz. Discrepancies between the longitudinal storage moduli identified from the two tests could be associated to the noise on the measurement, being lower than 3 GPa over the entire frequency range. On the contrary, the transverse storage modulus identified from the T-200x200-1 displacement field seems to be underestimated compared to that obtained by the displacement field measured in the T-200x200-5 test. Such discrepancies highlight the importance of the parameter Δ which could lead to an error of 30 % on the identified values.

3.5.3 Numerical variation

In the previous section, it is shown how the choice of the experimental spatial resolution Δ could impact on the results. In this section, results obtained using different values of Δ are presented. In order to avoid performing a large number of tests with different experimental spatial resolutions, the displacement field obtained from the test T-200x200-1 is used and Δ is changed considering only one in two, three, four, five.. points on each row and column of the measurement grid. With the purpose of validating this approach, a first comparison is made between the results obtained

using the experimental displacement field measured in the T-200x200-5 test with $\Delta_{exp} = 5\,\text{mm}$ and those ensued from the T-200x200-1 measurements from which only one out of five points is selected for the calculation in such a way to have a $\Delta_{num} = 5\,\text{mm}$. It can be observed in Fig. 3.14 that a good superposition of both the longitudinal and transverse storage modulus curves emerges. Indeed, the slight discrepancies which can be observed in particular for the longitudinal storage

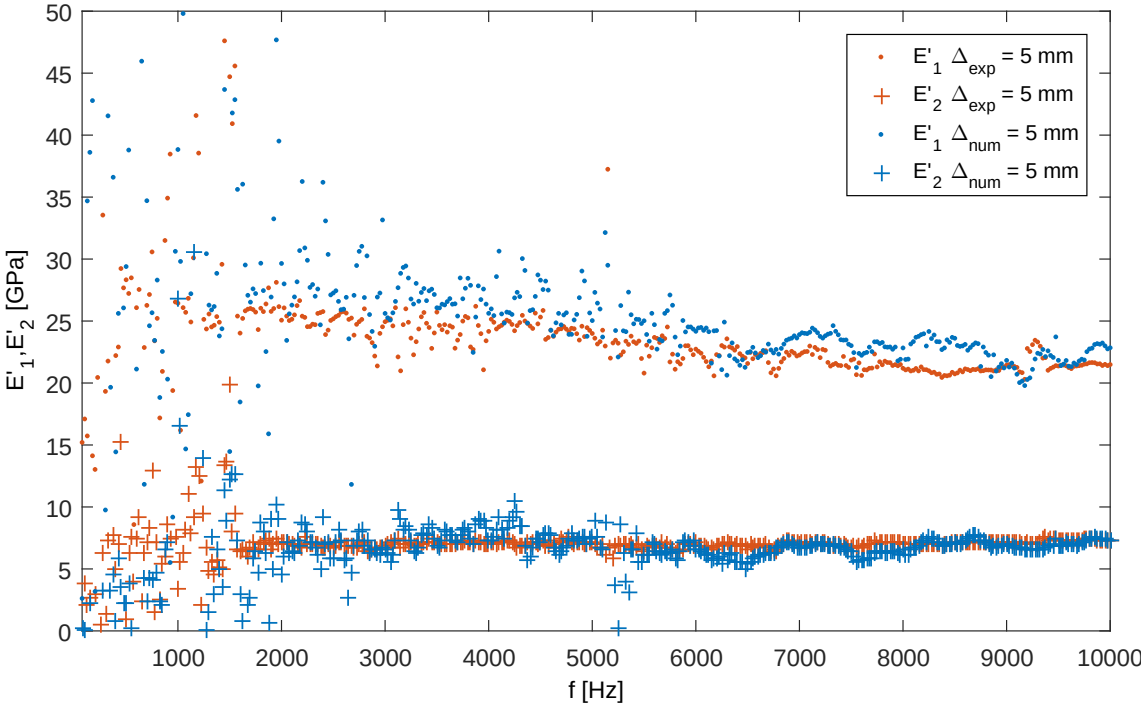

Fig. 3.14. Comparison of results obtained from T-200x200-5 and T-200x200-1 selecting a numerical spatial resolution of 5 mm.

modulus E'_1, could be related to the repeatability errors. Therefore, it can be concluded that the calculation of the dynamic properties choosing the value of Δ by the numerical approach, leads to a good approximation of results that could be obtained measuring the displacement field with the same value of spatial resolution.

In order to study the influence of the spatial resolution on the identified parameters, calculations are performed from the T-200x200-1 displacement field selecting, by the numerical approach explained above, the value of Δ. Results corresponding to spatial resolution values from 1 mm to 5 mm, are presented in Fig. 3.15. It is noteworthy that an increase of both longitudinal (Fig. 3.15(a)) and transverse (Fig. 3.15(b)) storage moduli is obtained following the increase of the spatial resolution Δ. Such an increase of the storage moduli is nevertheless not strictly proportional to the increase of the spatial resolution Δ. Moreover, a reduction of the dispersion is

observed for values of Δ higher than 1 mm. Observing Fig. 3.15(a), it can be noted that the curves corresponding to $\Delta = 2\,\text{mm}$, 3 mm, 4 mm and 5 mm lie in a limited range of values having a gap of 2 GPa. Similarly, the transverse storage modulus curves (Fig. 3.15(b)) for the same Δ values lie in a limited range with a discrepancy of 1 GPa. Higher values of Δ (7 mm and 10 mm) are used to obtain results reported in Fig. 3.16 and compared to those obtained using a Δ of 1 mm and 5 mm. It is observed that the decreasing trend observable with the frequency in the case of longitudinal storage modulus (Fig. 3.16(a)) using smaller spatial resolution, becomes an increasing trend when using $\Delta = 10\,\text{mm}$. It is noteworthy that the discrepancy of the identified parameters increases with the frequency. Moreover, as noted in Fig. 3.16(b), the influence of higher values of Δ seems more exacerbated for the transverse storage modulus. Such results lead to conclude that the spatial resolution Δ has a different impact depending on the frequency as well as the magnitude of the storage moduli.

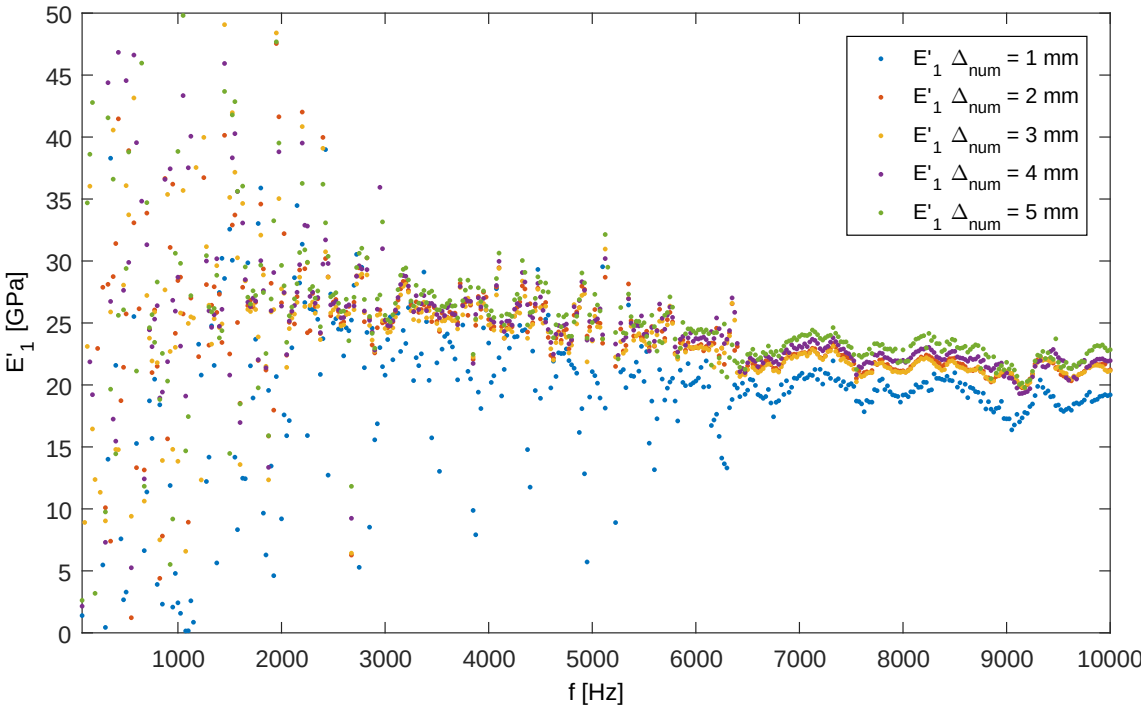

(a) Longitudinal storage modulus

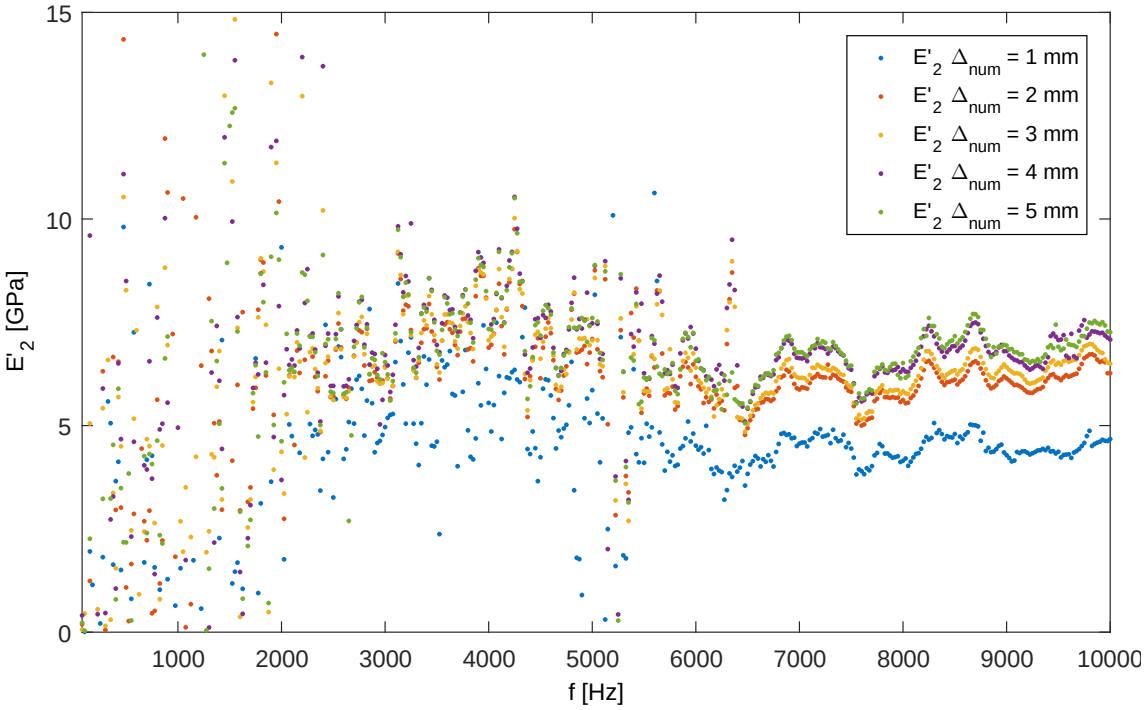

(b) Transverse storage modulus

Fig. 3.15. Longitudinal and transverse storage moduli identified from T-200x200-1 measurements using a Δ_{num} =1 mm, 2 mm, 3 mm, 4 mm and 5 mm.

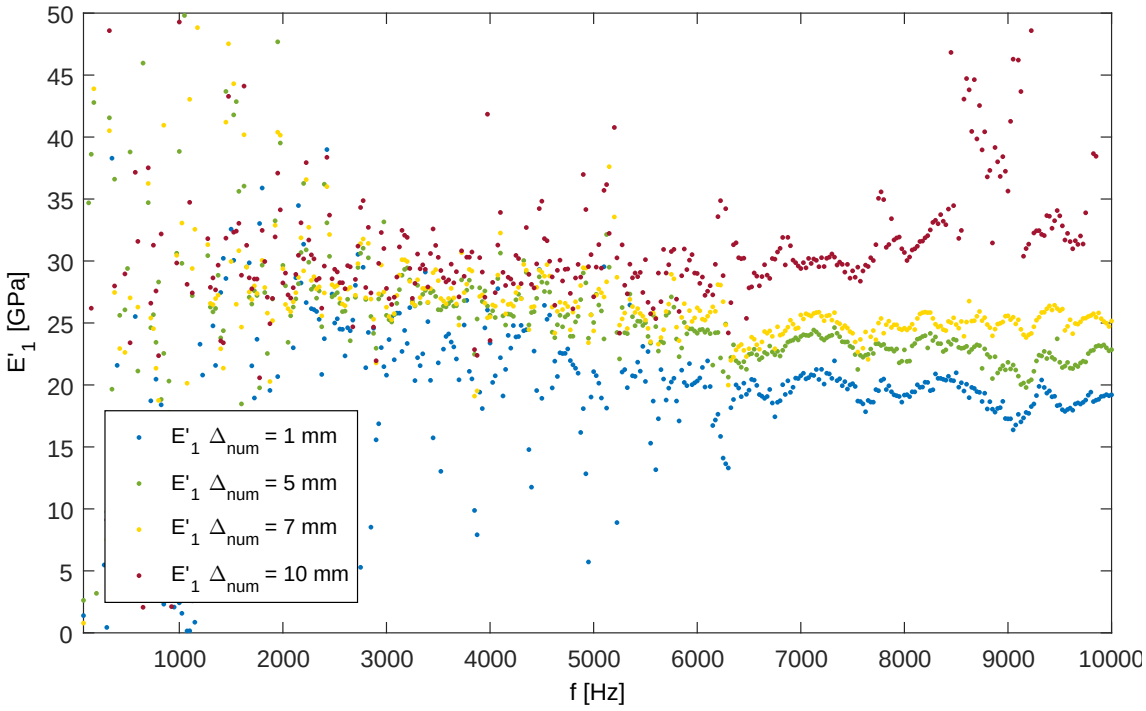

(a) Longitudinal storage modulus

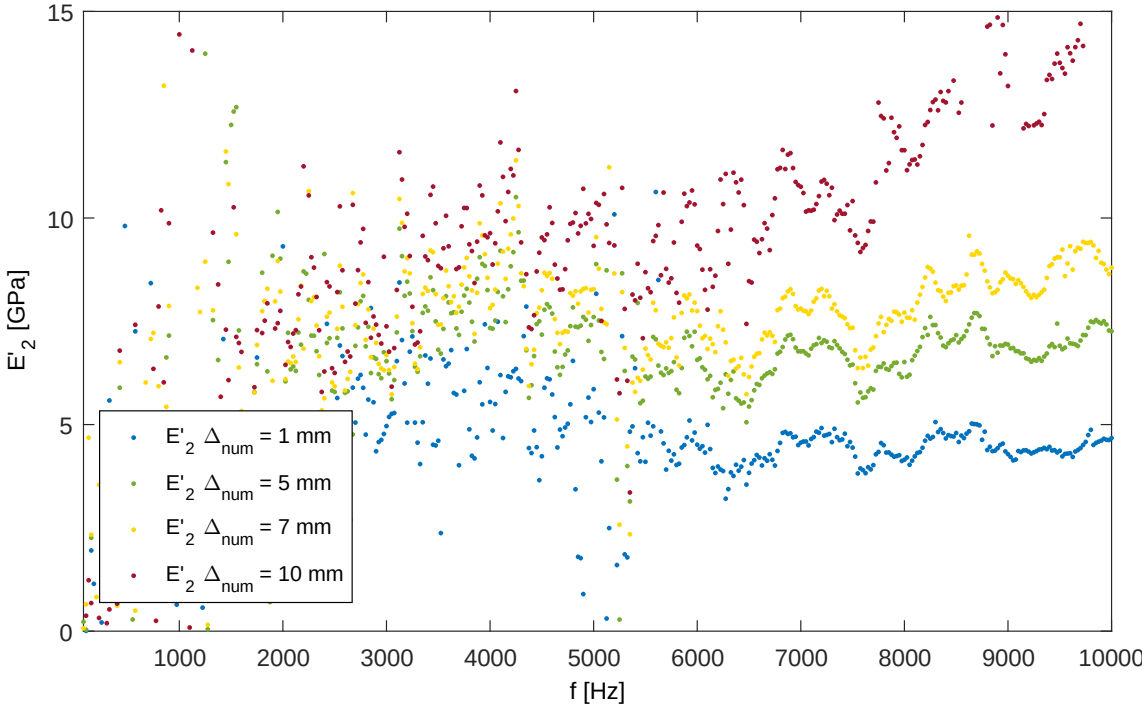

(b) Transverse storage modulus

Fig. 3.16. Longitudinal and transverse storage moduli identified from T-200x200-1 measurements using a Δ_{num} =1 mm, 5 mm, 7 mm and 10 mm.

3.5.4 Analytical study on λ/Δ ratio

As concluded in section 3.5.1 and in the wake of the results presented above, the formulation of a criterion for the optimum value of Δ to choose for the dynamic properties identification method is mandatory. Such a criterion should include information on the frequency, the corresponding wavelength (thus the storage modulus) as well as the spatial resolution. A parameter which relates the frequency with the storage modulus is the wavelength λ, corresponding to the length of the wave propagating in the plate at a given frequency (Fig. 3.17). Therefore, the criterion to be for-

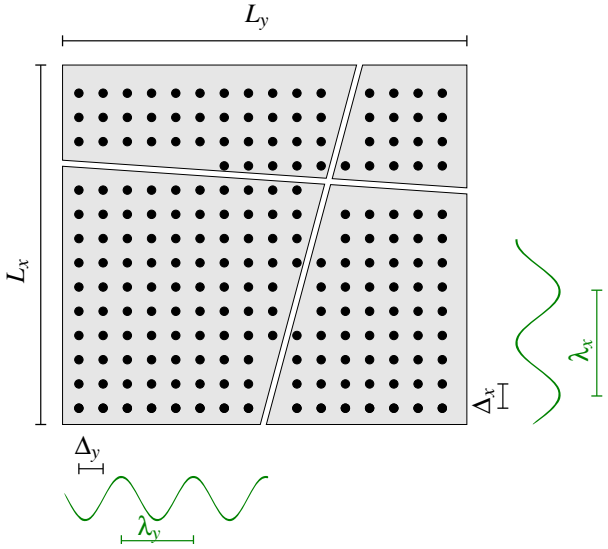

Fig. 3.17. Representation of the wavelength in the longitudinal (i.e λ_x) and transverse (i.e. λ_y) directions. The AOI dimensions L_x and L_y as well as the spatial resolution Δ_x and Δ_y are also reported.

mulated is based on the ratio of the wavelength λ related to a direction and the spatial resolution Δ, corresponding to the same direction, i.e. λ/Δ. Indeed, such a ratio represents a valid indicator as it gives the number of measured points over one wavelength. A number of 5 points on a wavelength is generally considered a good compromise to describe a signal. It must nevertheless be considered that, in the present study, the dynamic properties identification method makes use of the fourth order derivatives of the measured displacement field. Such derivatives, calculated with the finite difference method, could be incorrectly approximated if a too large spatial resolution is used. A numerical analysis is carried out to study the influence of the λ/Δ ratio on the approximation of the fourth order derivative. An analytical function (Eq. 3.6), shown in Fig. 3.18(a), is chosen in such a way to have the exact solution of its derivative (Eq. 3.7). Such a derivative is then approximated from the discretized original function using the same finite difference method

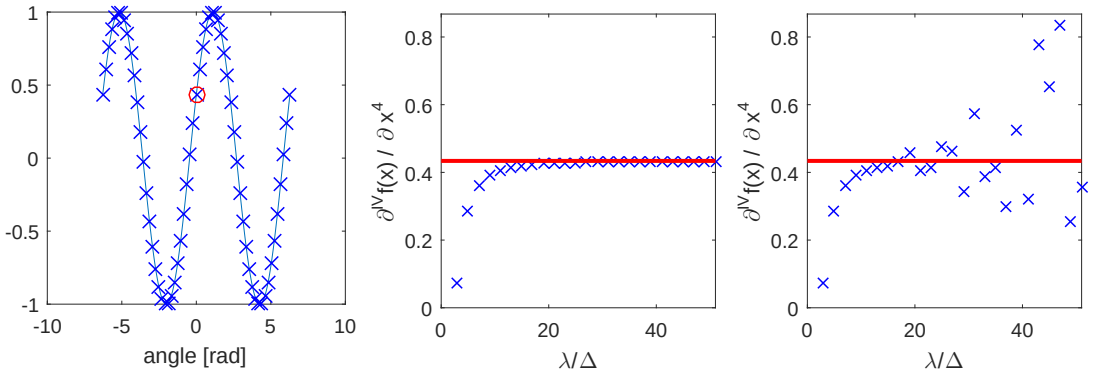

(a) Non noisy function (b) Non noisy derivative (c) Noisy derivative

Fig. 3.18. Effect of Δ on the derivative approximation of an analytical function. The analytical function (a) is discretized and the derivative approximation at the point i indicated by a red circle, are shown in (b) in case of absence of noise and in (c) in case of noisy data. The red line represents the analytical value of derivative at the point i.

reported in section 2.3.2, for different λ/Δ ratios between 5 and 50 (Eq. 3.8).

$$f(x) = \sin\left(x + \frac{\pi}{7}\right) \tag{3.6}$$

$$f^4(x) = \sin\left(x + \frac{\pi}{7}\right) \tag{3.7}$$

$$\delta^{4x}(i) = \frac{f(i+2\Delta) - 4f(i+\Delta) + 6f(i) - 4f(i-\Delta) + f(i-2\Delta)}{\Delta^4} \tag{3.8}$$

where i represents a generic point of the discretized x.

As shown in Fig. 3.18(b), the higher λ/Δ, the better the derivative approximation in case of non noisy functions. It is noteworthy that a good approximation of the derivative is made with λ/Δ higher than 7 with an error lower than 20 %. Such a conclusion is nevertheless valid only for non noisy data. Indeed, the presence of noise could lead to an amplification of the error on the derivative approximation. Therefore, an upper boundary value of λ/Δ ratio must be set since Δ constitutes itself a low-pass filter. For this purpose, some noise is introduced to the analytical function adding a random signal (*rand*) whose amplitude χ is chosen in such a way as to be in agreement with a defined SNR (Eq. 3.9). A SNR value equal to 50 is used to perform this analytical study, in the wake of observations reported in section 3.3 which confirm that the FAT-based method still leads to acceptable results when the displacement field is affected by such a level of noise. The forth order derivative of the analytical function is then approximated by the

finite difference method for different λ/Δ ratios.

$$f_{noisy}(x) = \sin\left(x + \frac{\pi}{7}\right) + \chi rand(-1;1) \tag{3.9}$$

As shown in Fig. 3.18(c), the error of the derivative approximation calculated on the discretized noisy function, increases with the λ/Δ ratio when this latter exceeds a threshold. The desired upper boundary value of λ/Δ, represented by such a threshold, is then fixed equal to 30, corresponding to the value at which the error between the analytical derivative and the approximated one is lower than 20 %. Moreover, it turns out that an increase of the noise level, which means a decrease of the SNR value, leads to a reduction of such boundary value.

3.5.5 Improved method

On the basis of the analysis carried out in the previous section, the dynamic properties for different values of Δ are calculated. For each Δ, the identified storage moduli in both longitudinal and transverse directions are used to estimate the λ/Δ ratios. Fig. 3.19 presents the identified storage moduli (in the upper graph) and the relative λ/Δ ratios (in the lower graph) over the range of frequencies between 25 Hz and 10 000 Hz obtained from the displacement field measured in the T-200x200-1 test and using a value of Δ_{num} from 1 mm to 10 mm. The threshold values of $\lambda/\Delta = 7$ and $\lambda/\Delta = 30$ are also reported in the graph. It is observed that for each value of Δ, the ratio λ/Δ decreases with the frequency. Indeed, according to the relations of λ and k_f reported in Eqs. 2.3 and 2.4, the higher the frequency, the smaller the wavelength. It emerges that values of spatial resolution between 2 mm and 6 mm meet the conditions for the optimal approximation of the fourth order derivatives in the considered frequency range. In addition, it should also be noted that for such values of Δ, the discrepancy on the identified storage modulus at high frequency is minimised.

A similar conclusion could be formulated observing Fig. 3.20 relative to the transverse storage modulus. Here, the values of Δ between 2 mm and 5 mm meet the boundary values on the λ/Δ ratio. Also in this case, these values of Δ lead to the minimisation of the discrepancy on the identified properties. It should be noted that smaller values of Δ are allowed in the transverse direction compared to the values allowed in the longitudinal direction.

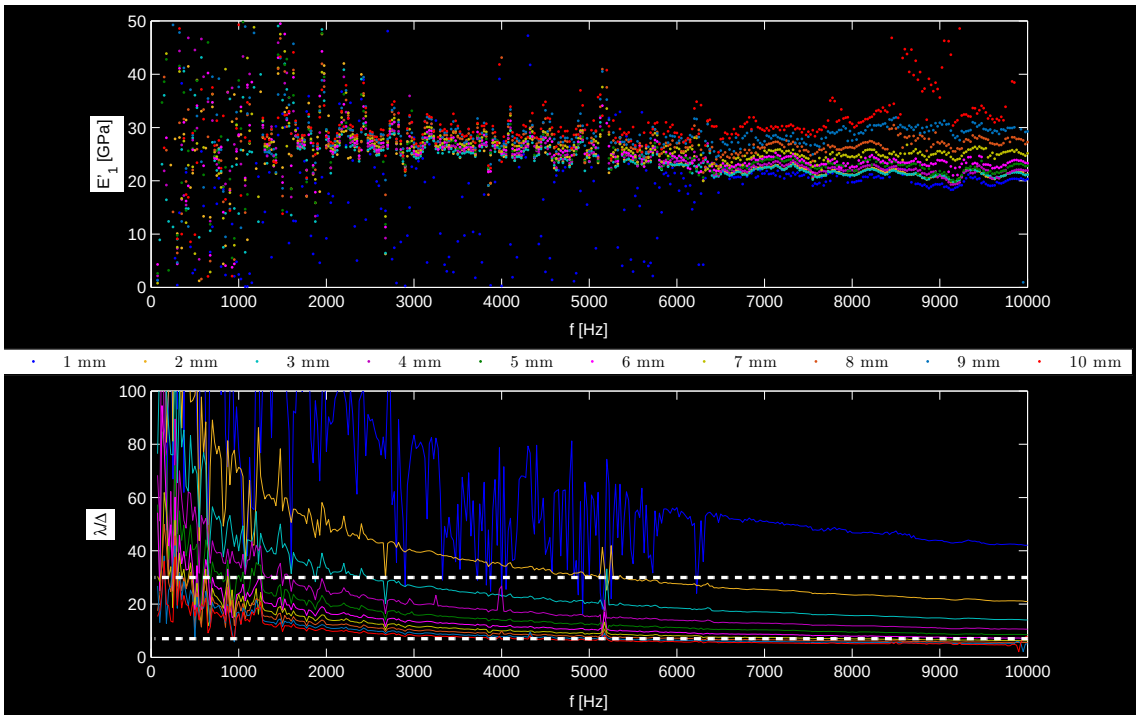

Fig. 3.19. Influence of Δ and λ/Δ ratios for the storage modulus E_1'. The threshold values of λ/Δ = 7 and $\lambda/\Delta = 30$ are also reported with white dotted lines.

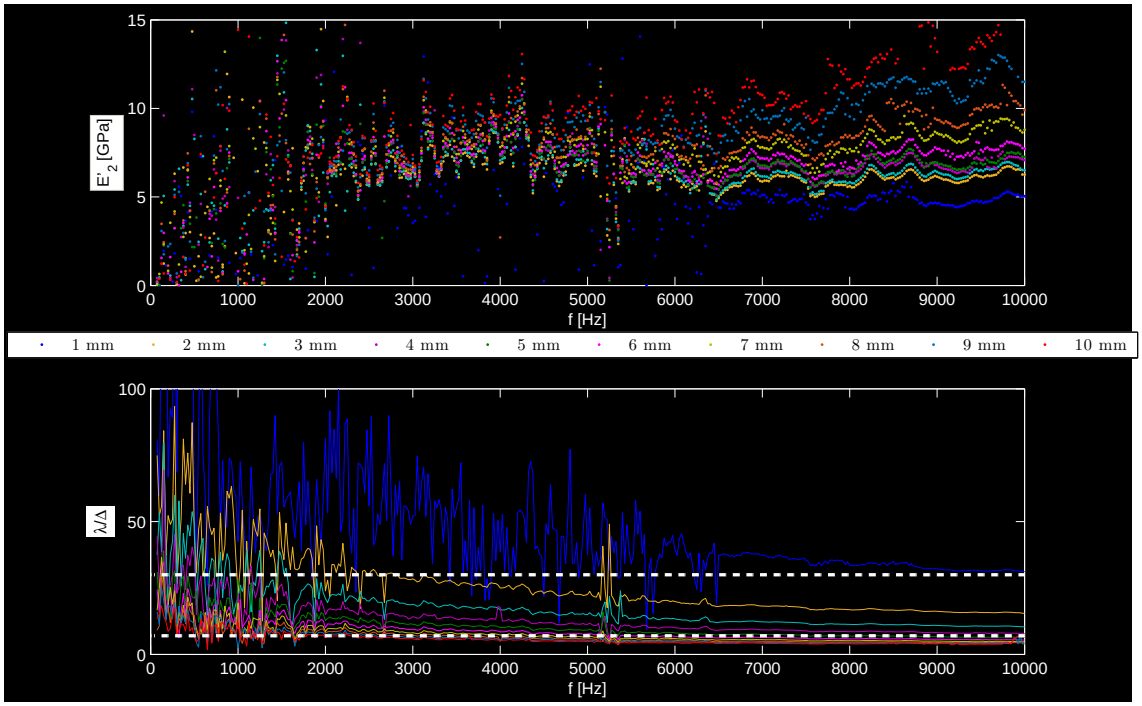

Fig. 3.20. Influence of Δ and λ/Δ ratios for the storage modulus E_2'. The threshold values of $\lambda/\Delta = 7$ and $\lambda/\Delta = 30$ are also reported with white dotted lines.

This is due to the different order of magnitude of the storage modulus in the two directions. Indeed, a lower storage modulus value leads to a shorter wavelength and, according to the limitation on the λ/Δ ratio, a smaller maximum value of Δ is allowed. It can further be noted that the optimal choice of Δ allows to reduce discrepancy over the high values of frequency and has not an important impact on the middle range of frequency (between 3000 Hz and 5000 Hz). However, over the low frequencies up to 3000 Hz results appear highly dispersed. The reduction of the discrepancy observed for results corresponding to a λ/Δ ratio between 7 and 30 confirms that the optimal spatial resolution for the dynamic property calculation should meet such threshold values.

Once the upper and lower boundary values of λ/Δ are selected, a reference value of λ may be defined to fix, subsequently, the value of Δ to use in the dynamic properties calculation. For this purpose, two ways are viable: an approximation of λ starting from a first calculation of dynamic properties performed using a small value of Δ, i.e. 1 mm, or the calculation of λ_1 and λ_2 starting from results obtained in quasi-static tensile tests. This latter method is applied here. Therefore, the algorithm used for the dynamic property identification method presented in section 2.3.4, is modify as follow:

1: E_1, E_2 $\leftarrow$ the longitudinal and transverse Young moduli are obtained by quasi-static tensile tests
2: **for** $f \in [f_{min}, f_{max}]$ **do**
3: $\lambda_1, \lambda_2 \leftarrow$ calculate the wavelength values at frequency f from Eqs. 2.3 and 2.4
4: Δ_1, $\Delta_2 \leftarrow$ calculate the spatial resolution values at frequency f in longitudinal and transverse direction in agreement with the chosen λ/Δ ratio
5: $\bar{w}(\Delta_{1,2}) \leftarrow$ get displacement field at frequency f using a numerically modified spatial resolution
6: $\nabla \leftarrow$ calculate the partial derivatives from Eq. 2.9
7: **for** $k_c \in [k_c^{min}, k_c^{max}]$ **do**
8: $\bar{w}$,$\nabla \leftarrow$ apply to each field the window and the filter using a cut-off wavenumber k_c
9: $\bar{D} \leftarrow$ calculate the least squares solution
10: $\mathfrak{R} \leftarrow$ calculate the residual sum of squares from Eq. 2.8 for each k_c
11: **end for**
12: D($\mathfrak{R}$) $\leftarrow$ calculate the derivatives in k_c of the least squares solutions
13: $k_c^{opt} \leftarrow$ choose the optimum k_c as in section 2.3.3

14: $D_{sel} \leftarrow$ select the solution D related to k_c^{opt} and frequency f

15: E_1', E_2', η_1, η_2, G_{12}', $\eta_{12} \leftarrow$ calculate storage moduli and loss factors for each D_{sel} and frequency f

16: **end for**

The longitudinal and transverse Young moduli obtained in the quasi-static tensile tests carried out on the material of study and presented in chapter 1 (longitudinal Young's modulus $E_1 = 26.6\,\text{GPa}$ and transverse Young's modulus $E_2 = 4.6\,\text{GPa}$), are used to calculate λ_1 and λ_2 respectively in longitudinal and transverse directions by Eqs. 2.3 and 2.4. The resulting wavelength values are reported in Table 3.4 for some frequencies. The values of Δ can then be calculated for longitudinal and transverse direction as a function of frequency, fixing a λ/Δ ratio meeting the lower and upper threshold values. The values of the spatial resolution against the frequency

$f[Hz]$	$\lambda_1[m]$	$\lambda_2[m]$
500	0.207	0.133
1000	0.146	0.094
2000	0.104	0.067
3000	0.085	0.055
5000	0.065	0.042
6500	0.057	0.037
8000	0.052	0.033
10000	0.046	0.028

Table 3.4: Variation of λ_1 and λ_2 with the frequency, calculated using the quasi-static tensile test results.

obtained in the longitudinal and transverse direction using a λ/Δ ratio equal to 7 are reported in Fig. 3.21 for frequencies between 2000 Hz and 10000 Hz. It is observed that, as attended, the spatial resolution Δ_1 in longitudinal direction is higher than Δ_2 in transverse direction, all over the frequency range. Values between 15 mm and 7 mm are calculated for Δ_1 whereas Δ_2 ranges between 9 mm and 4 mm. Such values are then used in the dynamic property identification method to numerically modify the spatial resolution from the T-200x200-1 test results. The identified longitudinal and transverse storage moduli obtained by the presented method are shown in Fig. 3.22. A comparison with curves related to results obtained from a constant spatial resolution is also reported. It is noteworthy in Fig. 3.22(a) that the longitudinal storage modulus is identified all over the observed frequency range. A value of 26 GPa is identified over the frequency range between 2000 Hz and 5500 Hz, whereas it drops down to 21 GPa for frequencies above 5500 Hz. More-

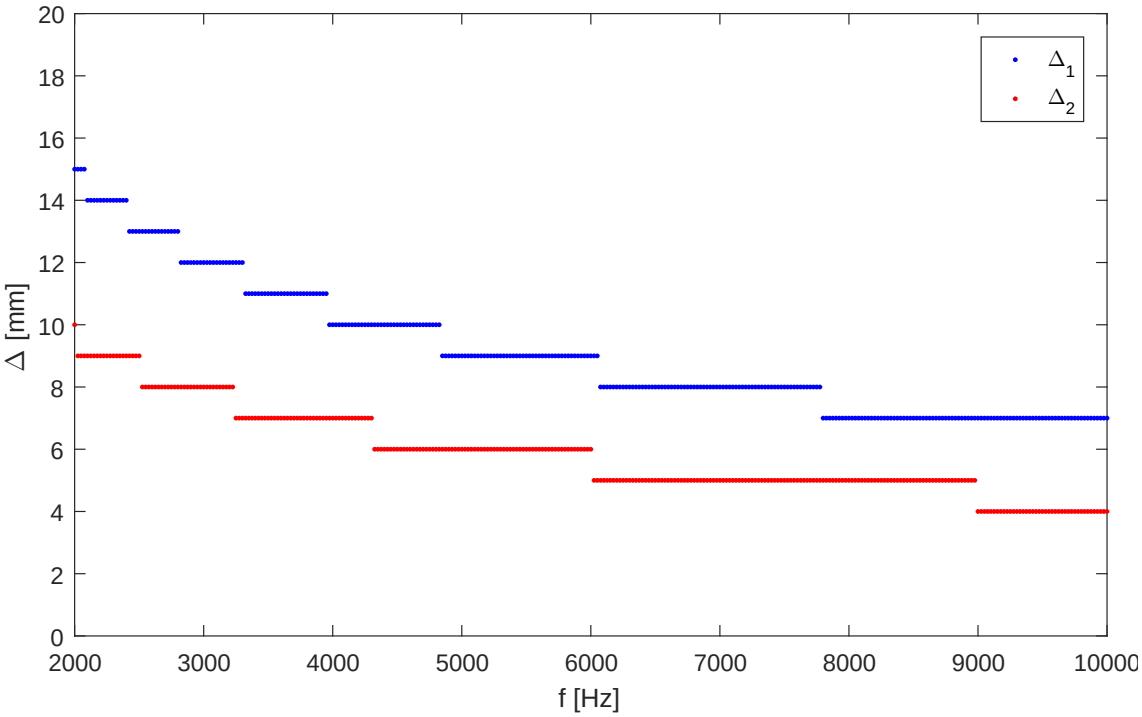

Fig. 3.21. Optimal spatial resolution values for $\lambda/\Delta = 7$.

over, also in the case of the transverse storage modulus, the frequency range can be divided in two sections. Indeed, as shown in Fig. 3.22(b) the transverse storage modulus values are equal to 6.5 GPa over frequencies between 2000 Hz and 5000 Hz, whereas they are equal to 5.5 GPa above 5000 Hz. Moreover, it can be observed that, even though results at high frequencies are characterized by fluctuations, they are less affected by dispersion. Conversely, a significant dispersion is present in results at frequency below 5000 Hz. The focus in the next section of this document is concentrated on this latter issue. Considering that a value of Δ = 5 mm seems to satisfy the optimal conditions presented in this section for both the longitudinal and transverse directions over a frequency range between 1000 Hz and 10 000 Hz, only this value of spatial resolution will be used in the following analysis.

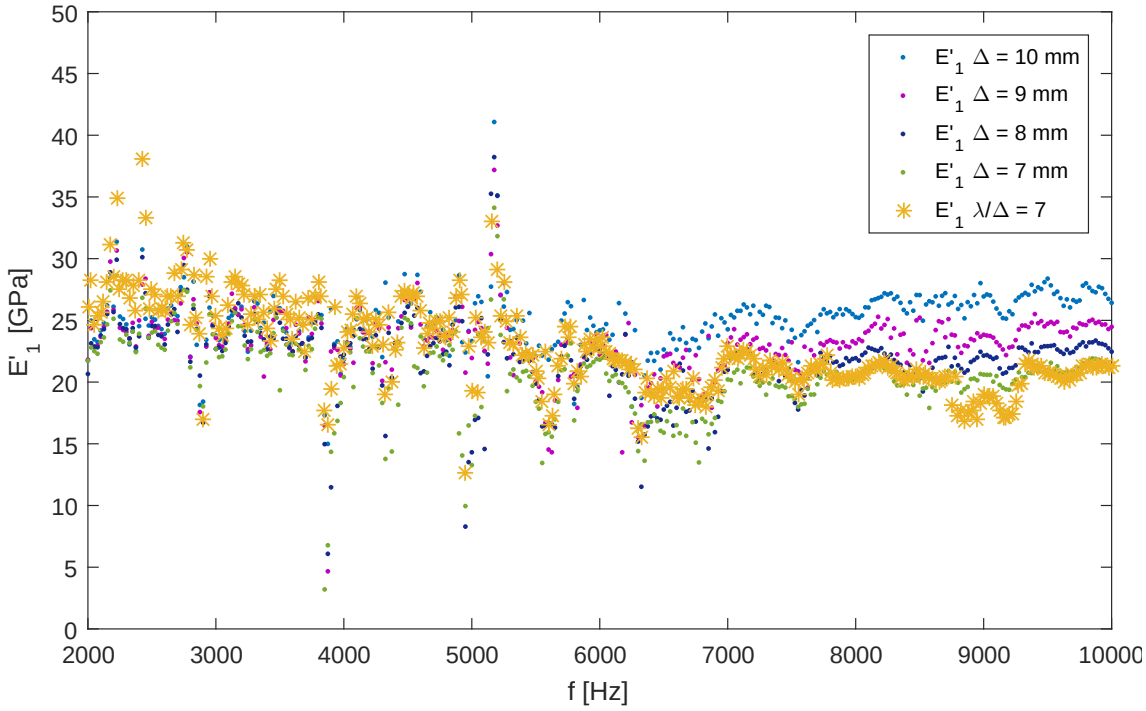

(a) Longitudinal modulus

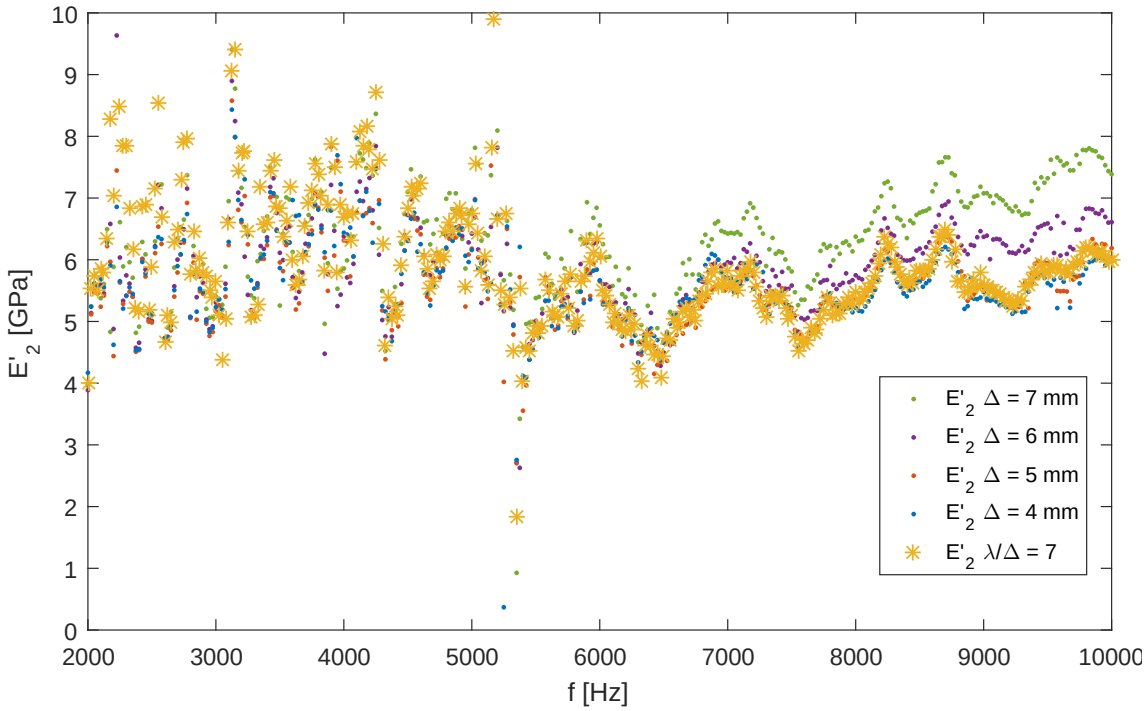

(b) Transverse modulus

Fig. 3.22. Storage moduli identified by the improved method, with λ/Δ ratio equal to 7

3.6 Influence of the area of interest size

In order to study the cause of the dispersion which characterizes results of the identification method over frequencies up to 5000 Hz, an analysis on the dimensions of the measured area is carried out in this section. Tests on different area of interest (AOI) sizes are performed on the same plate and respecting the same excitation parameters. For this purpose, the displacement field is measured at the centre of the plate, over an area of 50 mm × 50 mm, 100 mm × 100 mm, 300 mm × 300 mm and 390 mm × 330 mm. Results obtained by the identification method from the different displacement fields are compared with those obtained from the displacement field measured over an area of 200 mm × 200 mm used in the previous section. It should be noted that all the areas of interest presented have a square geometry, except in the case of the largest area of dimensions 390 mm × 330 mm for which, because of a limitation due to the measurement system, a restriction on the width dimension is required.

A reduction of the area on which the displacement field is measured, is adopted in a first step. For this purpose, T-50x50-5 and T-100x100-5 tests are performed measuring the out-of-plane displacements at the centre of the vibrating plate on an area of respectively 50 mm × 50 mm and 100 mm × 100 mm. The so measured displacement fields are used as input of the identification method to calculate the material dynamic properties. The comparison of results with those obtained using the displacement field measured in the T-200x200-5 test is presented in Fig. 3.23. A decrease of the AOI size leads to an increase of the dispersion affecting the results. Indeed, neither the longitudinal storage modulus (Fig. 3.23(a)) nor the transverse storage modulus (Fig. 3.23(b)) can be identified using the results obtained for the T-50x50-5. Moreover, a reduction of the dispersion occurs for results obtained using the displacement field of T-100x100-5 test. In particular, observing the T-100x100-5 curves, it can be noted that such a dispersion seems to decrease with the frequency. Moreover, the identified values of the longitudinal storage modulus E_1' over the frequencies above 8000 Hz, as well as the transverse storage modulus E_2' over the frequencies above 6500 Hz, lie in a very limited range. A further increase of the AOI size, in the case of T-200x200-5, leads to a noteworthy reduction of dispersion affecting the storage moduli in both the longitudinal and transverse direction over a large frequency range. The longitudinal and transverse storage moduli can be estimated between 2000 Hz and 10000 Hz. For frequencies below 2000 Hz the results are noticeably dispersed as already commented in the previous section. As noted, the dispersion on the storage moduli seems to decrease with the frequency. Therefore, a further increase

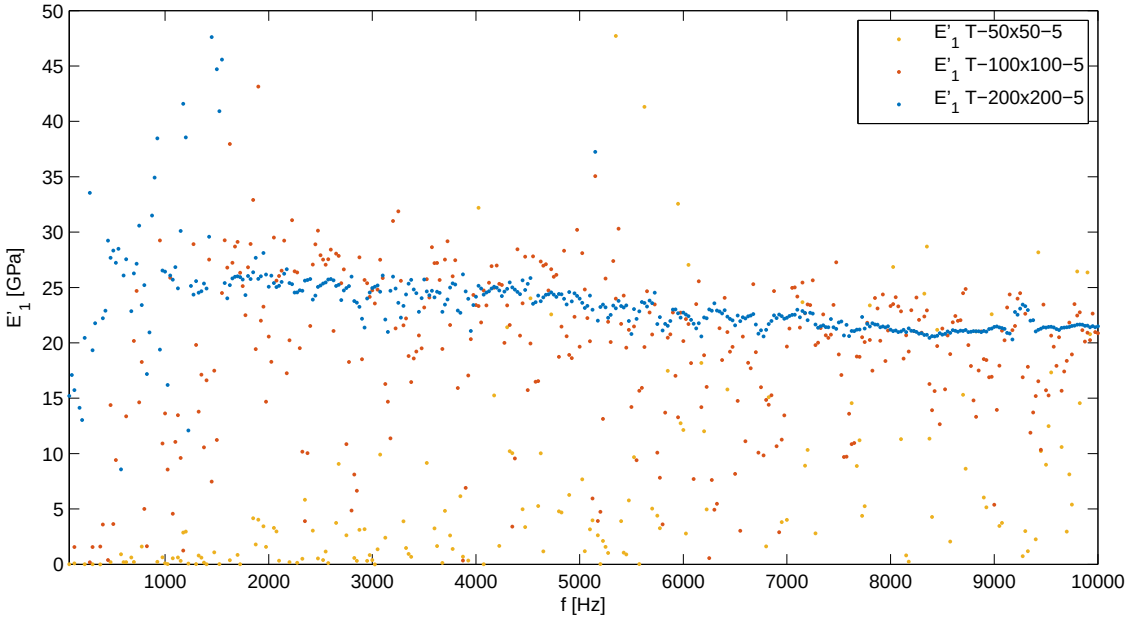

(a) Longitudinal modulus

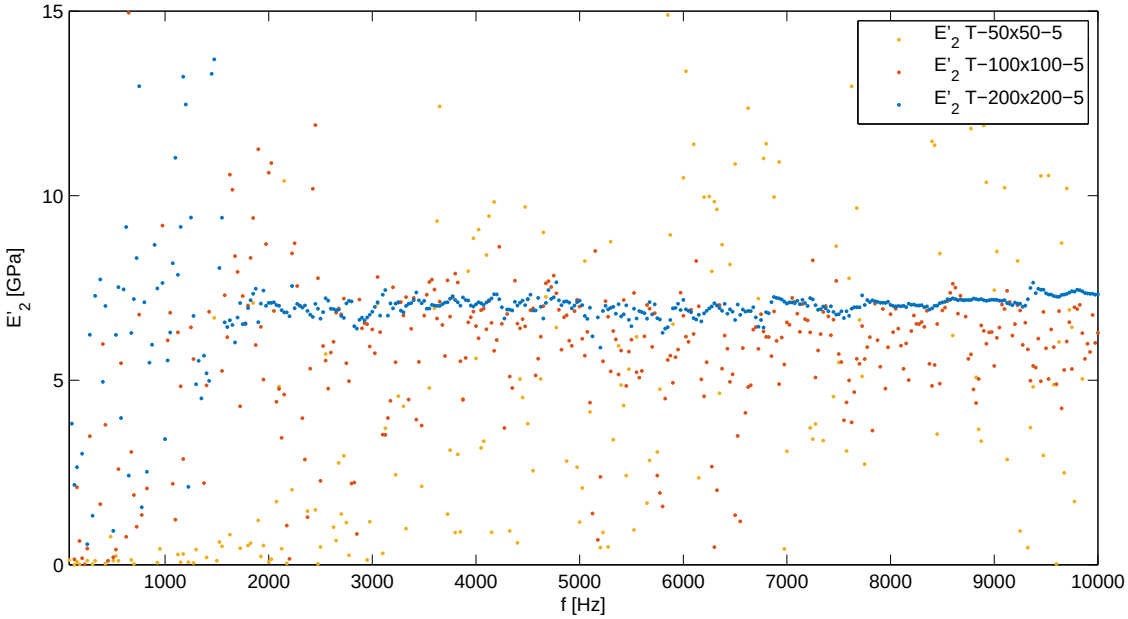

(b) Transverse modulus

Fig. 3.23. Comparison of storage moduli obtained with the displacement field measured in T-50x50-5, T-100x100-5 and T-200x200-5 tests.

of the measured area size could lead to less dispersed results over the low frequencies.

In a second step, an increase of the AOI dimensions is pursued. Storage modulus values resulting from the displacement fields measured on areas of 300 mm × 300 mm and 390 mm × 330 mm are compared with those obtained measuring a displacement field on an area of 200 mm × 200 mm in Fig. 3.24. A reduction of the dispersion affecting the results is actually observed with the increase of the AOI size. Indeed, the red curve corresponding to the T-300x300-5 test presents more limited spread than the blue curve corresponding to the T-200x200-5 test. Moreover, observing the transverse storage modulus obtained from the T-300x300-5 test in Fig. 3.24(b), an important dispersion occurs only below 1000 Hz and it is quite reduced between 1000 Hz and 2000 Hz. Nevertheless, some fluctuations of the storage modulus values are observed on both the longitudinal and transverse directions. Such fluctuations could be related to the plate dynamics or to the experimental setup (table resonances, plate fixations or shaker screwing to the plate), but no further investigations are carried out in this study for their understanding. The further increase of the AOI size does not lead to a noteworthy improvement of results. Moreover this latter test seems to result in overestimated storage modulus values. The gap is nevertheless limited and can be associated to repeatability errors due to the removal and the re-installation of the plate occurring before the execution of this test. The improvement of the results obtained with the increase of the AOI size is also observed in the identification of the loss factors. Until now, no results have been presented on the loss factor because the high dispersion which impacts the results makes their identification difficult. However, as observed in Fig. 3.25, the T-300x300-5 and T-390x330-5 tests allow to determine the values of η_1 and η_2 over the range of frequencies between 2000 Hz and 10 000 Hz. Indeed, contrary to T-200x200-5 which gives highly dispersed values of loss factors, the T-300x300-5 and T-390x330-5 tests result in a loss factor mean value equal to 0.01 and 0.03 respectively for the longitudinal and transverse directions between 1000 Hz and 6000 Hz. However, an increasing trend is observed for the two loss factors over frequencies above 6000 Hz. This trend may be related to aero-dynamic phenomena due to the interaction of the vibrating plate with the air. The understanding of these phenomena are not nevertheless taken into account in this study.

Such an improvement of the results quality related to the increase of the AOI size can be associated to the ratio between the AOI dimensions (L) and the wavelength of the vibration in the corresponding direction (λ) (cf. Fig. 3.17). Indeed, it is observed in Fig. 3.23 that the reduction of

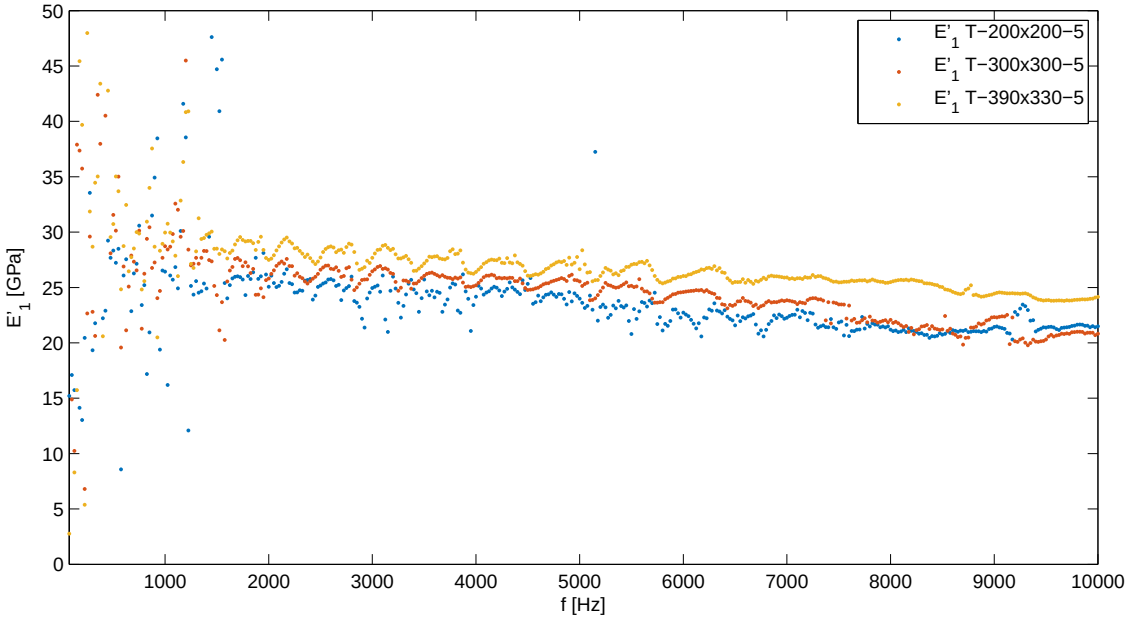

(a) Longitudinal modulus

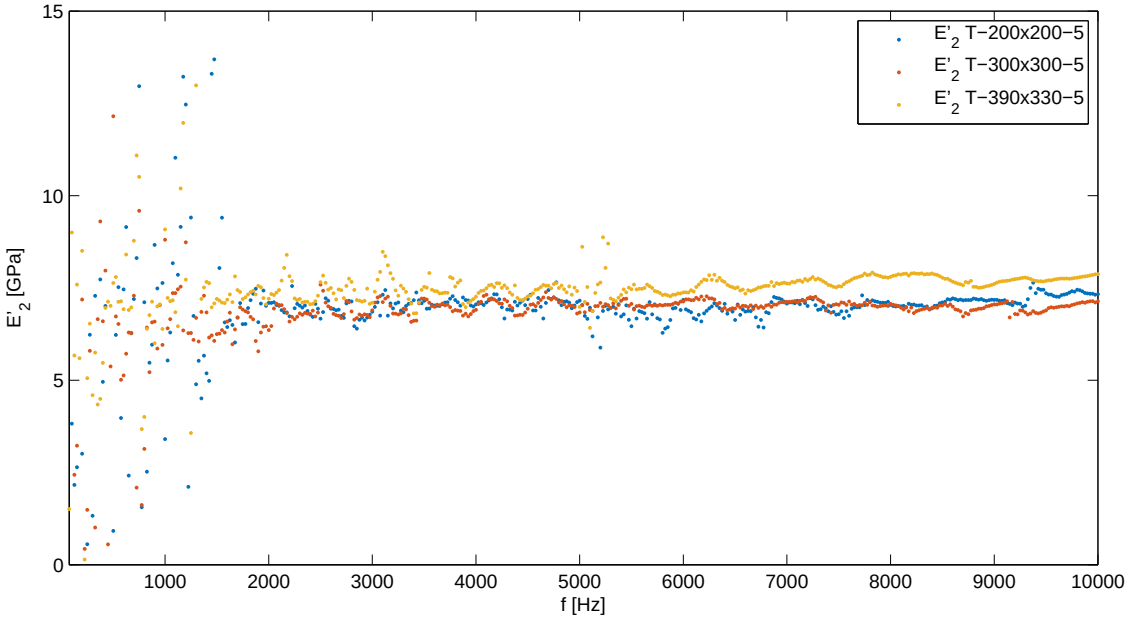

(b) Transverse modulus

Fig. 3.24. Comparison of storage moduli obtained with the displacement field measured in T-200x200-5, T-300x300-5 and T-390x330-5 tests.

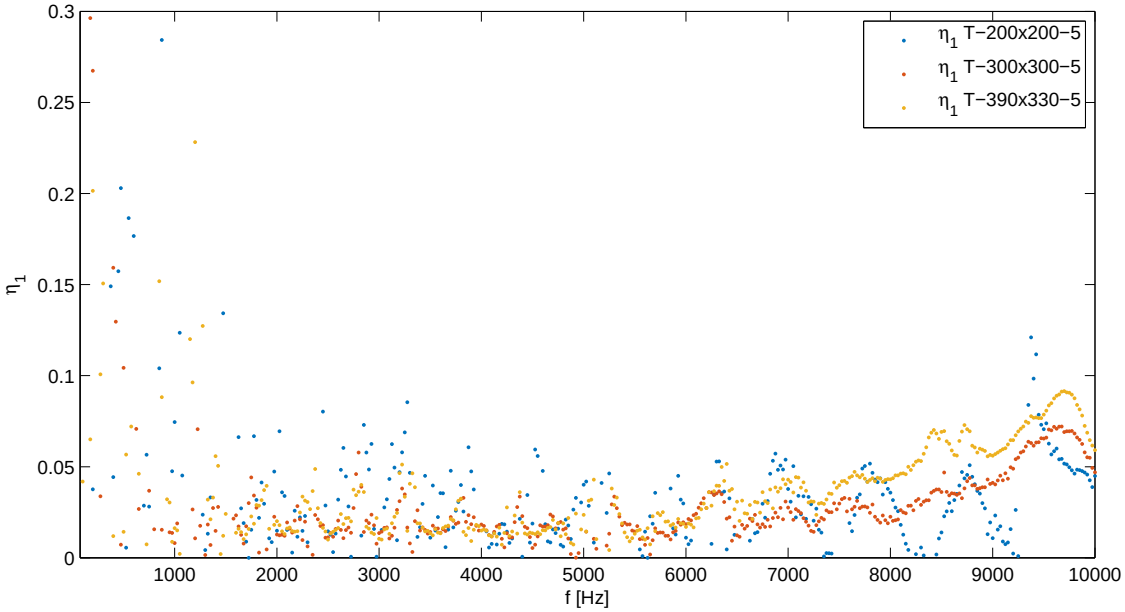

(a) Longitudinal loss factor η_1

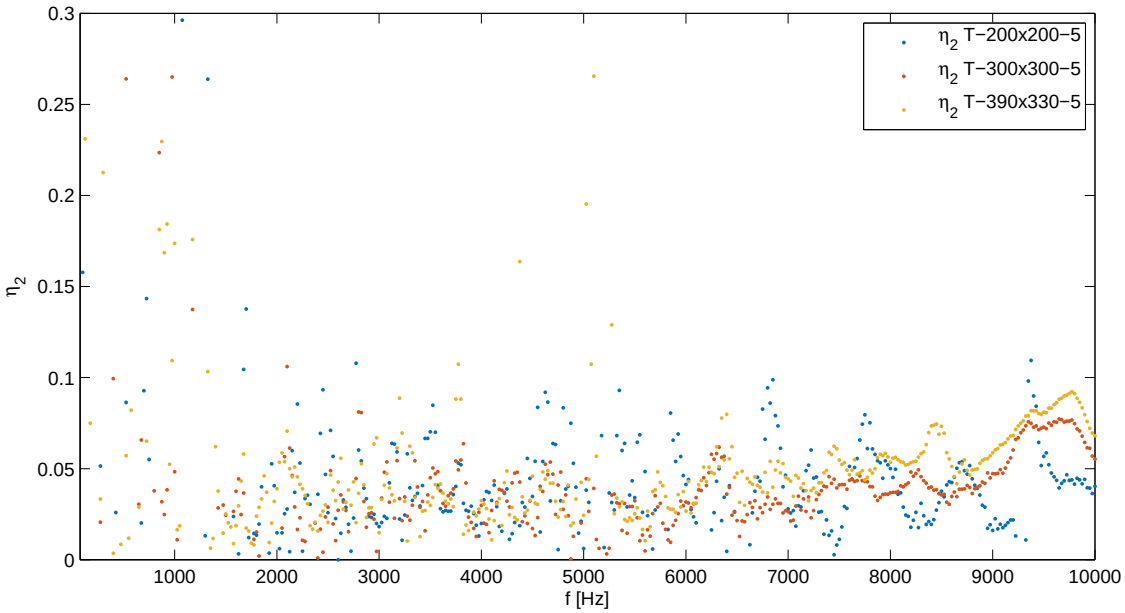

(b) Transverse loss factor η_2

Fig. 3.25. Comparison of loss factors obtained with the displacement field measured in T-200x200-5, T-300x300-5 and T-390x330-5 tests.

dispersion noted for T-100x100-5 curves, occurs at frequencies above 8000 Hz for the longitudinal modulus and above 6500 Hz for the transverse one. According to the wavelength values reported in Table 3.4, at such frequencies, the calculated wavelength in longitudinal and transverse directions are respectively $\lambda_1(8000\,\text{Hz}) = 52\,\text{mm}$ and $\lambda_2(6500\,\text{Hz}) = 37\,\text{mm}$, corresponding to $L/\lambda_1 = 1.92$ and $L/\lambda_2 = 2.70$. Furthermore, observing T-200x200-5 curves, the impact of dispersion on the identified moduli is less relevant for frequencies above 2000 Hz, for which the wavelength values are $\lambda_1 = 120\,\text{mm}$ and $\lambda_2 = 67\,\text{mm}$. The respectively L/λ ratios are 1.67 and 2.98. On the bases of such observations, a L/λ ratio of at least 2 is then suggested. It is obvious that such ratio can not be fixed a priori if the material Young's moduli are not know. If the Young's modulus values are known, the AOI dimensions can be adjusted to respect the specifications on L/λ ratio on the principal material directions. Such an expedient can allow to reduce the execution time of tests. For this reason, the next section of this study concerns an analysis on an AOI rectangular shape, which dimensions depends on the identified Young's moduli on both longitudinal and transverse directions.

3.7 Influence of the shape of the area of interest

As reported at the end of the previous section, in order to achieve a significant reduction of the experimental time, tests may be carried out on an area of interest having a rectangular shape. Indeed, the dimensions of the measured area could be reduced in both longitudinal and transverse directions respecting the minimal size necessary in agreement of the considered frequency range. Therefore, the dimensions of the area of interest should be chosen in such a way to observe at least two wavelengths in each direction over the frequency range of interest. For this purpose, results obtained using a displacement field measured over an AOI of dimensions that are in agreement with the values of longitudinal and transverse Young's moduli, are presented in this section. The AOI dimensions in x- and y- directions, chosen on the base of the calculated wavelength values reported in Table 3.4, are then respectively 300 mm and 100 mm. In Fig. 3.26, the obtained longitudinal and transverse moduli are compared to those calculated from the displacement field measured over an area of dimensions 300 mm $\times$ 300 mm in the T-300x300-5 test. As observed in Fig. 3.26(a), the identified longitudinal moduli are in line for both tests. Indeed, no relevant differences can be noted over the frequency range between 1500 Hz and 7500 Hz. Moreover, discrepancies observed at frequencies above 7500 Hz are limited to 3 GPa and could be related to reproducibility errors. Similarly, in the case of transverse storage moduli (Fig. 3.26(b)), a good superposition of the curves is observed for frequencies up to 7500 Hz, nevertheless above this value of frequency, a slight difference is also noteworthy in the case of transverse storage moduli. Such a discrepancy is however lower then 1 GPa and, also in this case, can be related to the reproducibility issues. It can be concluded that the prior knowledge of the Young's modulus values in both the longitudinal and transverse directions can allow to choose a minimal area of interest which dimensions are selected in such a way to observe at least two wavelength over the frequency range of interest. Such an expedient allows to considerably reduce the measurement time. Indeed, in T-300x300-5 test, a number of 3721 points are scanned, whereas with T-300x100-5 the displacement measurements are performed on only 1281 points, leading to a reduction of 70 % of the experimental time.

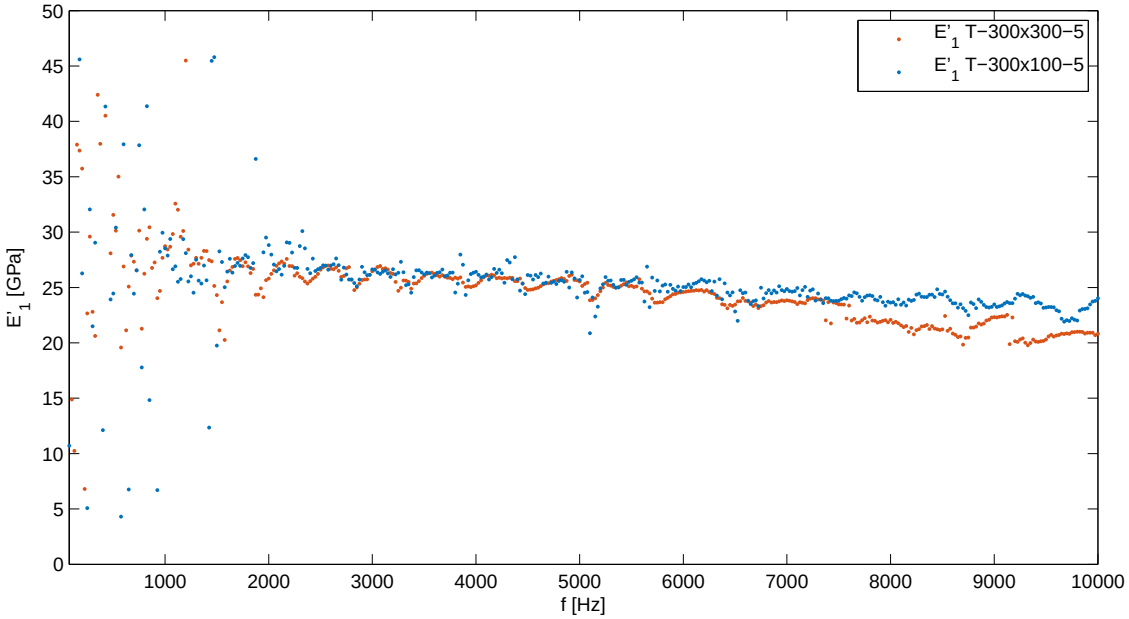

(a) Longitudinal modulus

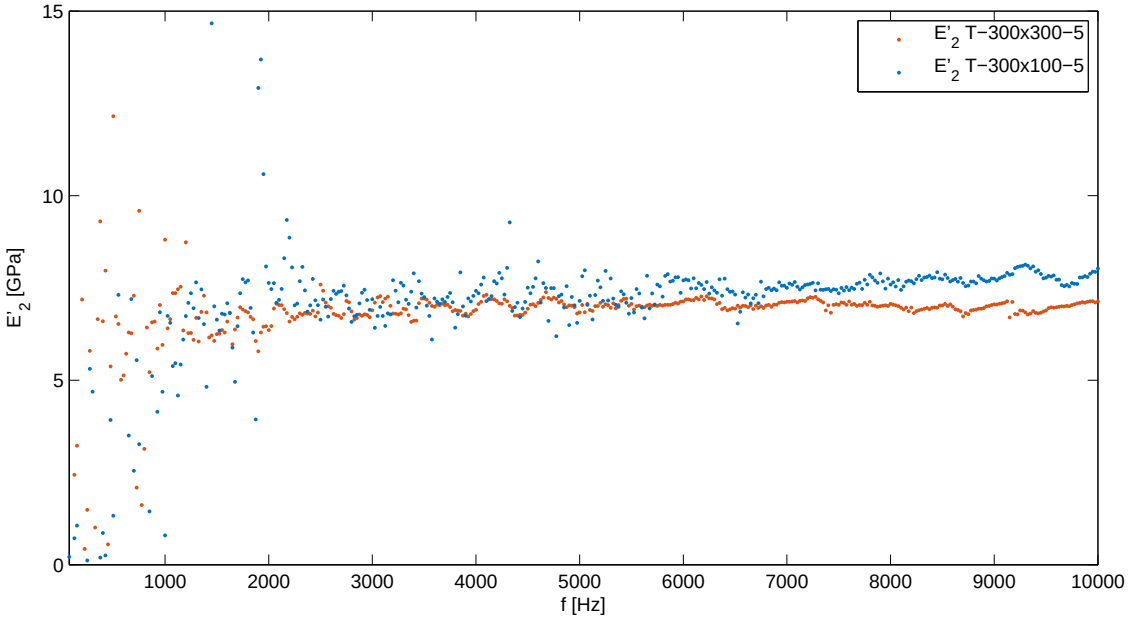

(b) Transverse modulus

Fig. 3.26. Comparison of longitudinal (a) and transverse (b) storage moduli, obtained from T-300x100-5 and T-300x300-5 tests.

3.8 Influence of the boundary conditions

The last parameter taken into account in the sensitivity analysis carried out in this study is the location of the measured area in the plate plane. All the tests presented so far are actually performed on areas of interest placed at the centre of the plate. The boundary conditions could although have an impact on the identified parameters. Indeed, the assumption for which the force involved in the plate equation of motion is negligible in the area of interest, which constitutes the basis for the application of the identification method, could not be respected. For this purpose, two further tests, T-200x100-5-D on a rectangular area and T-100x100-5-D on a square area, are performed at different locations. In particular, as shown in Fig. 3.27, the rectangular area of dimensions 200 mm $\times$ 100 mm (the purple area enclosed in the dashed line) is measured at the centre of the left-half of the plate, whereas the square area of dimensions 100 mm $\times$ 100 mm is located at the centre of the right-bottom quarter of the plate (green area in Fig. 3.27).

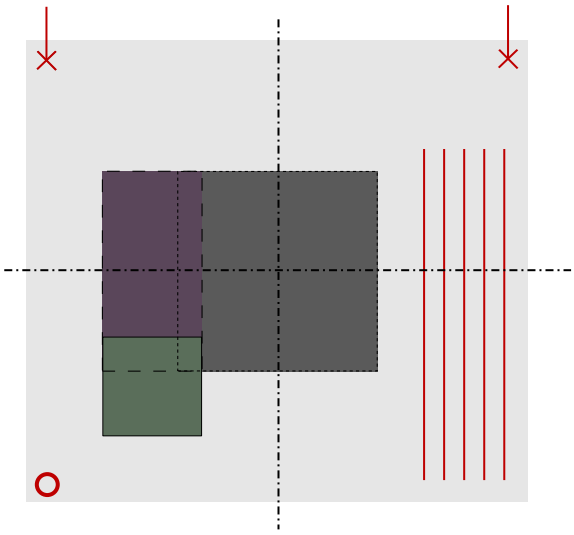

Fig. 3.27. Locations of the measured areas. The grey area of dimensions 200 mm $\times$ 200 mm enclosed in the densely dashed line is located at the centre of the plate. The purple area of dimensions 200 mm $\times$ 100 mm enclosed in the loosely dashed line is located at the centre of the left-half of the plate. The green area of dimensions 100 mm $\times$ 100 mm is located at the centre of the left-bottom-quarter.

In Fig. 3.28, the storage moduli obtained using T-200x100-5-D are compared to those calculated from T-200x200-5 displacement field measured at the centre of the plate. As can be noted, a slight discrepancy of the longitudinal storage moduli is found between the two tests. However, such a discrepancy remains lower then 3 GPa and could be related to reproducibility error. Con-

versely, in the transverse direction a good superposition of the curves relative to the two tests is observed. Moreover, the increase of the dispersion noticeable on the curves related to the T-200x100-5-D test is due to the reduction of the AOI size and not to the influence of the boundary conditions. Indeed, a smaller area closer to the excitation point is tested in T-100x100-5-D configuration. The identified storage moduli are then compared in Fig. 3.29 with those obtained on an AOI of the same dimensions located at the centre of the plate (i.e. T-100x100-5 test). As already observed, in the case of small areas, the results are much more dispersed than those derived from wider AOI. Nevertheless, the comparison between the results of T-100x100-5-D and the T-100x100-5 does not highlight significant differences neither in the longitudinal nor in the transverse directions. It can be concluded that the location of the AOI has not an important impact on the identified storage moduli.

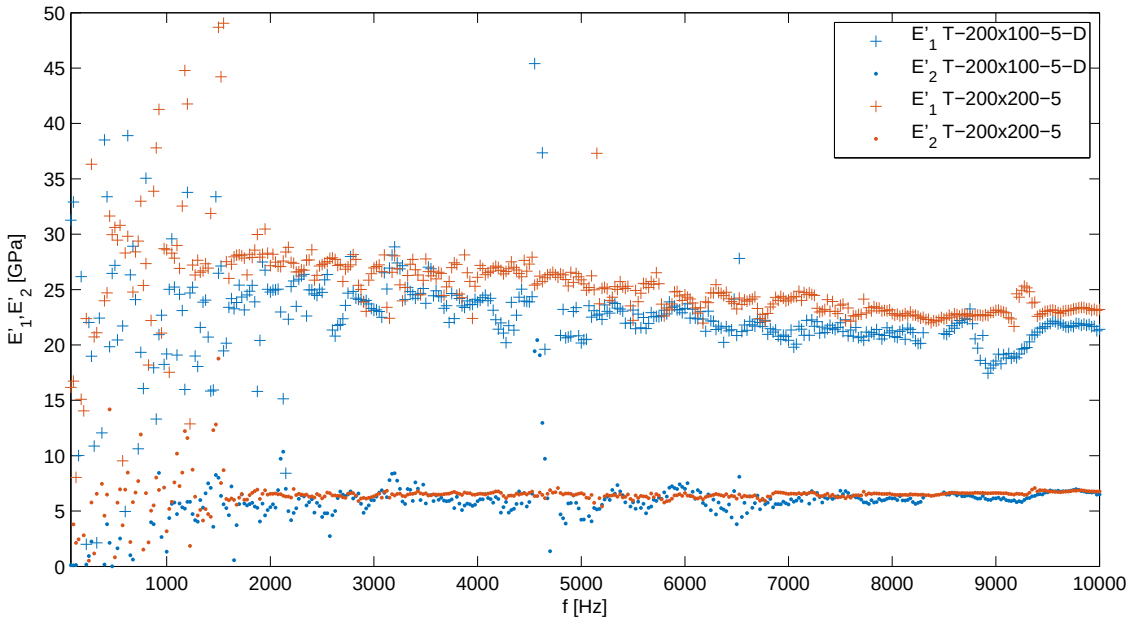

Fig. 3.28. Comparison of longitudinal and transverse storage moduli obtained from T-200x100-5-D and T-200x200-5 tests

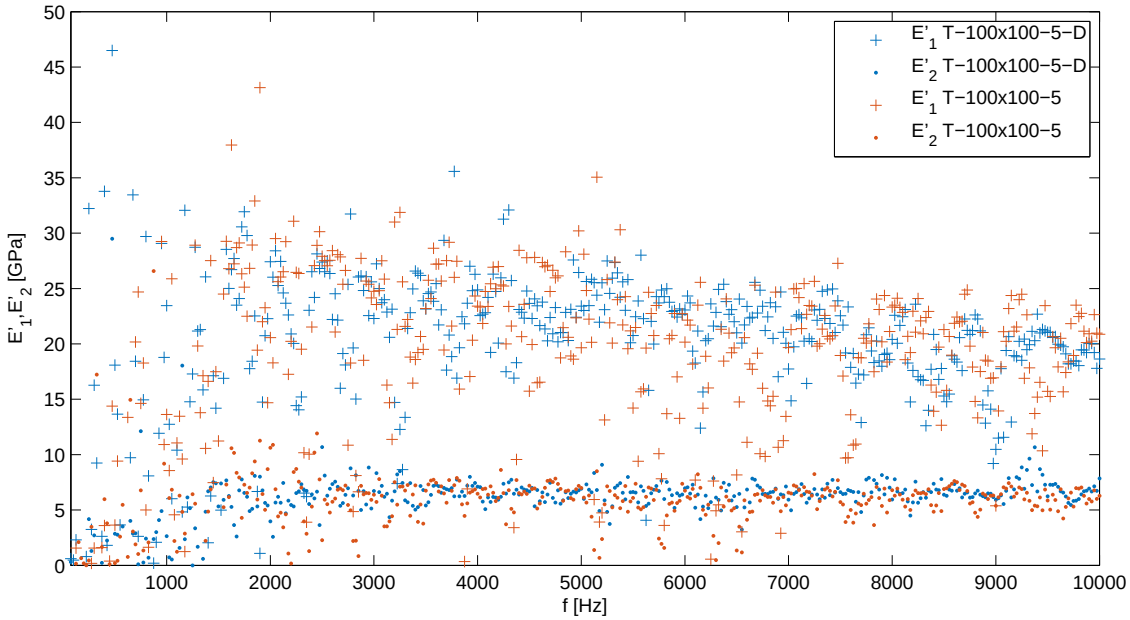

Fig. 3.29. Comparison of longitudinal and transverse storage moduli obtained from T-100x100-5-D and T-100x100-5 tests

3.9 Conclusions

This chapter presents a sensitivity analysis of the dynamic properties identification method used in this Ph.D study. Four parameters are taken into account: the spatial resolution Δ, the size of the area of interest, its shape as well as its location in the plate plane. A repeatability analysis conducted on two plates shows in a maximum discrepancy of 3 GPa on the longitudinal identified storage modulus and 0.6 GPa on the transverse one. It is concluded that a relative gap of 6 % on results is associated to repeatability errors.

Several parameters are then examined in a reproducibility analysis: the plate orientation, the environmental conditions and the equipments used for the measurement and excitation. Neither for the longitudinal storage modulus nor for the transverse storage modulus, no distinction can be made on the basis of the testing orientation angle. The comparison of results obtained from measurements carried out in different laboratories shows a good correlation for the identified longitudinal storage modulus, confirming that the experimental equipments and the environmental conditions do not have an influence on the results. Nevertheless, such a comparison highlights the ageing of the PA11 matrix, with a 30 % increase of the transverse storage modulus; this is consistent with results presented in chapter 1. Moreover, tests conducted on 7 plates show a longitudinal storage modulus in a range between 30 GPa and 20 GPa characterized by a decreasing trend with the increasing frequency of about 0.001 GPa Hz^{-1} whereas the transverse storage modulus present a rather constant value of about 5 GPa.

The influence of the noise affecting the displacement measurements using an analytical displacement field is firstly considered in the sensitivity analysis. It is observed that when data are affected by an important level of noise, the FAT-based method does not allow a correct property identification, especially in the case of loss factors. Moreover an artificial increasing trend of the identified storage moduli with the frequencies is observed on results obtained using the calculated analytical displacement field not affected by noise. The crucial effect of the noise on the identified parameters makes essential the good selection of the low-pass filter. An analysis on the validity of the automatic selection of the filter parameter k_c is then carried out. The comparison of the obtained results with those coming from a manual selection confirms the good results of the automatic selection.

The effect of the spatial resolution Δ is also studied in the sensitivity analysis. A discussion

is firstly addressed on results obtained using an analytical non noisy displacement field, showing that an increase of the spatial resolution leads to an increasing trend of the identified dynamic properties with the frequency. The experimental variation of such a parameter confirms the crucial impact on the identified storage moduli. The equivalence of the numerical variation of the spatial resolution with the experimental variation is verified. An increase of both the longitudinal and transverse storage moduli is observed with the increase of the spatial resolution Δ. Nevertheless, such a trend is not proportional to the increase of Δ. On noisy data, a larger value of spatial resolution acts as a low-pass filter of measurement noise. However, an excessive increase of the distance between two measured points leads to an improper sampling of small wavelength related to high frequencies.

Since an estimation of the noise is a priori not possible, measurements may be conducted on a dense grid and a criterion to find the optimum spatial step allowing both the good approximation of the derivatives and the reduction of the noise should be applied. A criterion for the selection of the optimal Δ to use is proposed with a λ/Δ ratio in the range from 7 to 30 for an optimal approximation of the fourth order derivatives at a selected frequency. An improved method for the dynamic property identification is then proposed in order to automatically adjust the spatial resolution with the frequency. It results that, for a λ/Δ ratio equal to 7, the spatial resolution ranges between 15 mm at 2000 Hz and 7 mm at 10000 Hz. Concerning the transverse direction, the Δ respecting the $\lambda/\Delta = 7$ is between 10 mm at 2000 Hz and 4 mm at 10000 Hz. A constant value of $\Delta = 5$ mm in both longitudinal and transverse direction is then selected for further analysis.

The influence of the area of interest size on the identified dynamic properties is then analysed. The displacement fields are measured on square areas located at the centre of the plate. A reduction of the dispersion with the increasing dimensions is observed. Furthermore, a lower dispersion in the estimation of the loss factors η_1 and η_2 is also noted for the two largest AOI. Such an improvement of the quality can be related to the ratio between the AOI dimensions and the wavelength λ. A minimum ratio of the AOI dimensions L and the wavelength λ equal to 2 is then suggested to meet a good result quality.

On the wake of this assumption, a rectangular AOI is considered, so that the dimensions of the AOI respect the abovementioned ratio. Results confirm that the preliminary knowledge of the Young's moduli allows to select a minimal area of interest which dimensions are in agreement with the L/λ ratio suggested. In such a way a strong reduction of the experimental time can be

achieved.

In order to verify the impact of the boundary conditions on the method results, the location of the area of interest in the plate plane is then analysed. Two areas offset from the centre are considered. A slight discrepancy lower then 3 GPa is found for the longitudinal storage moduli and could be related to reproducibility errors. Although some results are affected by a significant dispersion, it can be concluded that the location has not a significant impact on the identification method.

General conclusion

The growing consciousness on energy and environmental issues leads the automotive manufacturers to improve efficiency and to reduce vehicle mass. In the light-weighting process, the substitution of traditional materials such as steel with fibre reinforced polymers matrix composites is generally chosen. In particular, special attention is focused on natural fibre reinforced biopolymers. Such materials present many advantages: lower environmental and energy impacts, light-weighting capacity and low price. Another important characteristic is their good damping properties, making them suitable to be used in applications where vibration and noise control is important. In such applications, the knowledge of the material dynamic properties over a large range of frequencies is fundamental. The main objective of this study is to characterize the dynamic behaviour of a flax fibre reinforced polyamide 11 (FF/PA11) over a range of frequencies between 25 Hz and 10 kHz.

Assessment of the presented results

In the first chapter, a bibliographic study is conducted, showing a description of the flax fibre. For this purpose, the attention is firstly focused on the growing process, from the sowing to the spinning. The microstructure as well as the mechanical properties are also discussed. Similarly, a description of the polyamide 11 is presented, from the synthesis process to the final mechanical properties. An overall description of the film stacking and hot moulding process as well as on the parameters involved in the process gives important information on the optimal cycle to use in the manufacturing of the flax fibre reinforced polyamide 11 (FF/PA11). A review of the studies conducted on static and dynamic properties highlights the lack of information available on the latter over a wide range of frequencies. The literature review on the FF/PA11 is completed by presenting results on its aptitude to impact resistance and recycling. Then, the material elaborated for this study is described. A number of 10 plates are manufactured using unidirectional flax fibres and films of polyamide 11 with a fibre volume ratio of 42 %. The film stacking and hot moulding process is employed to obtain the composite plates. Microstructure observations are carried out by Scanning Electron Microscopy (SEM) and X-ray tomography. Such observations show that the manual film stacking process has not a strong impact on the fibre alignment. Moreover, SEM observations highlight a good fibre impregnation as well as the absence of porosity. Quasi-static

tensile tests are then carried out to obtain Young's moduli and Poisson's ratios in both fibre and transverse directions. The obtained Young's modulus values are compared with those available in literature showing a good agreement. Furthermore, tests performed in different time periods highlight the effect of the material long-time ageing on the transverse Young modulus. Stress relaxation tests are also performed with the aim to correlate the visco-elastic parameters with the dynamic properties obtained over a wide frequency range. For a lack of time, this correlation is not carried out.

In order to characterize FF/PA11 dynamic behaviour over a range of frequencies between 25 Hz and 10 kHz, a FAT-based method already presented in literature, is used in this work and described in the second chapter. The material dynamic property identification is performed using the local equation of motion of a thin plate, together with the measured displacement field of a vibrating plate and its approximated derivatives. The expressions of window and filter used to reduce the measurement noise influence are also presented. Digital Image Correlation (DIC) is first used as the displacement field measurement technique. Although such a technique allows the measurement of the entire displacement field at once, representing a significant time saving, the noise impacting the measured data does not allow the proper identification of the material dynamic properties. The laser Doppler vibrometer (LDV) is then selected for further analysis because of its better reliability and higher sampling frequency. Such a technique is firstly applied on a sheet moulding compound (SMC) plate and leads to the identification of the storage moduli over the principal directions of the plate, which values are in line with the previous quasi-static tensile tests. The same measurement technique and FAT-based method are then employed to characterize the dynamic properties of 3 flax fibre reinforced PA11 plates, i.e. the storage moduli and loss factors over the fibre and transverse directions and over a frequency range between 25 Hz and 10 000 Hz. For this purpose, Poisson's ratios obtained from the quasi-static tensile tests presented in the first chapter, together with the plate thickness, material density and the measured displacements are used. The applied method allows the dynamic properties identification over the entire frequency range. Nevertheless, a strong dispersion of the storage moduli is observed for frequencies below 2000 Hz. Moreover, a decreasing trend with the frequency of the storage modulus in fibre direction is noteworthy. The FAT-based method results are compared with the ones obtained from a dynamic mechanical analysis using the time-temperature superposition principle. The identified values on longitudinal storage modulus are in line with each other. Conversely, a discrepancy of 35 % is

observed for transverse storage modulus. Such a discrepancy may be due to the dimensions of the DMA specimens. A good agreement is moreover observed between the loss factor values over both the longitudinal and transverse directions.

The third chapter is addressed to a study of different parameters influencing the FAT-based method. Firstly, a repeatability and reproducibility analysis is performed. A deviation of 8 % and 6 % for respectively the identified longitudinal and transverse storage moduli, can be associated to repeatability errors. Moreover the reproducibility analysis highlights that the method is not influenced by the plate orientation, environmental conditions and equipments used for the excitation or measurements. However, it is noteworthy a sensitivity of the method to the material long-term ageing, also observed from quasi-static tensile tests. A sensitivity analysis is then carried out. An analytical study on the noise influence shows that an important noise level does not allow a proper identification. Moreover, a discussion on the parameter involved in the window and filter application is addressed showing that, even if the automatic selection of such a parameter leads to acceptable results, any improvements can be made in order to adapt the filter cut-off wave-number according to the fibre and transverse directions. Furthermore, an analysis of the measurement spatial resolution is carried out showing that the spatial resolution used in the measurement has a strong impact on the results. Indeed, small values of this parameter contribute to increase the measurement noise influence in the derivative approximations whereas greater values act as noise filter but restrict the analysis to low frequencies corresponding to vibrations having long wavelength, according to the Shannon principle. A criterion for the choice of the spatial resolution optimum value is then formulated. Such a criterion is based on the ratio between the wavelength and the spatial resolution. An analytical study allows to fix the lower and upper threshold values of this ratio, respectively equal to 7 and 30. The comparison of experimental results obtained for different spatial resolutions confirms these threshold values. An improved method is then proposed in order to automatically select an optimal spatial resolution value over the entire frequency range during the dynamic properties calculation. Moreover, the influence of the area of interest size is analysed, highlighting that an increase of this parameter leads to a reduction of the dispersion affecting the FAT-based method results. An optimal ratio between the AOI dimensions and the wavelength, i.e. L/λ equal to 2 is observed. A reduction of the area of interest can be considered in agreement with the minimal L/λ ratio. An analysis on the impact of the boundary conditions highlights that the FAT-based method results are not influenced by the AOI location.

Perspectives

This study has allowed the dynamic behaviour characterization of the FF/PA11. Nevertheless, further analysis can be carried out. To the knowledge of the author, no study is carried out on the long-term ageing of flax fibre reinforced PA11. Moreover, as highlighted in the previous section, stress-relaxation test results can be used to obtain information about the material visco-elastic parameters. Such results, notably the storage modulus and loss factors, can be compared with those obtained by the identification method obtained in the present work.

Additional works could be carried out to improve the reliability of the digital image correlation technique for the displacement field measurements. Indeed, the sampling frequency of high speed cameras used to perform DIC is limited to 5400 Hz and, according with the Shannon-Nyquist principle, the analysis is restricted to 2000 Hz. Moreover, as previously seen, the results obtained so far by the dynamic behaviour characterization method are limited to a range of frequencies between 2000 Hz and 10 000 Hz. Such limitation could be due to the limited dimensions of measurement area. In order to extend results over a lower range of frequencies, a wider area has to be considered.

As shown in the second chapter, the calculation of the approximated derivatives is performed on the noisy displacement field and the filter used to reduce the measurement noise is applied to the displacement field and its derivatives only afterwards. Even though such an algorithm allows to save computation time because the derivative fields are calculated only once for each selected frequency, the calculation of the derivatives on a raw displacement field amplifies the influence of noise. Better results could be obtained applying the filter upstream of the derivative approximation. The architecture of the algorithm could be changed in this direction.

Another important improvement of the method can be made adjusting the filter cut-off wavenumber according to the direction of fibre and the transverse one. Actually, this parameter depends on the natural wavelengths of the plate which are different in the two directions for an orthotropic material. Such improvements could lead to a better identification of loss factors in the two directions.

Bibliography

[1] European commission. https://ec.europa.eu/clima/. Accessed: 2018-09-11.

[2] N. Scarlat, J. F. Dallemand, F. Monforti-Ferrario, M. Banja, and V. Motola. Renewable energy policy framework and bioenergy contribution in the european union–an overview from national renewable energy action plans and progress reports. *Renewable and Sustainable Energy Reviews*, 51:969–985, 2015.

[3] International Energy Agency. Key world energy statistics 2017. www.iea.org. Accessed: 2018-09-11.

[4] H. L. MacLean, L. B. Lave, R. Lankey, and S. Joshi. A life-cycle comparison of alternative automobile fuels. *Journal of the air & waste management association*, 50(10):1769–1779, 2000.

[5] C. Manzie, H. Watson, and S. Halgamuge. Fuel economy improvements for urban driving: Hybrid vs. intelligent vehicles. *Transportation Research Part C: Emerging Technologies*, 15(1):1–16, 2007.

[6] S. Das. *The cost of automotive polymer composites: a review and assessment of DOE's lightweight materials composites research*. Oak Ridge National Laboratory Oak Ridge, Tennessee, USA, 2001.

[7] F. Ning, W. Cong, J. Qiu, J. Wei, and S. Wang. Additive manufacturing of carbon fiber reinforced thermoplastic composites using fused deposition modeling. *Composites Part B: Engineering*, 80:369–378, 2015.

[8] Z. Quan, A. Wu, M. Keefe, X. Qin, J. Yu, J. Suhr, J. H. Byun, B. S. Kim, and T. W. Chou. Additive manufacturing of multi-directional preforms for composites: opportunities and challenges. *Materials Today*, 18(9):503–512, 2015.

[9] R. A. Witik, J. Payet, V. Michaud, C. Ludwig, and J. A. E. Månson. Assessing the life cycle costs and environmental performance of lightweight materials in automobile applications. *Composites Part A: Applied Science and Manufacturing*, 42(11):1694–1709, 2011.

[10] L. Puech, K. R. Ramakrishnan, N. Le Moigne, S. Corn, P. R. Slangen, A. Le Duc, H. Boudhani, and A. Bergeret. Investigating the impact behaviour of short hemp fibres reinforced

polypropylene biocomposites through high speed imaging and finite element modelling. *Composites Part A: Applied Science and Manufacturing*, 109:428–439, 2018.

[11] D. G. Hepworth, R. N. Hobson, D. M. Bruce, and J. W. Farrent. The use of unretted hemp fibre in composite manufacture. *Composites Part A: Applied Science and Manufacturing*, 31(11):1279–1283, 2000.

[12] A. Bourmaud and C. Baley. Investigations on the recycling of hemp and sisal fibre reinforced polypropylene composites. *Polymer Degradation and stability*, 92(6):1034–1045, 2007.

[13] A. Arbelaiz, B. Fernandez, J. A. Ramos, A. Retegi, R. Llano-Ponte, and I. Mondragon. Mechanical properties of short flax fibre bundle/polypropylene composites: Influence of matrix/fibre modification, fibre content, water uptake and recycling. *Composites Science and Technology*, 65(10):1582–1592, 2005.

[14] J. Biagiotti, D. Puglia, and J. M. Kenny. A review on natural fibre-based composites-part i: structure, processing and properties of vegetable fibres. *Journal of Natural Fibers*, 1(2): 37–68, 2004.

[15] Lotus cars. `http://www.lotuscars.com/engineering/eco-elise`. Accessed: 2018-09-11.

[16] A. K. Mohanty, M. Misra, and L. T. Drzal. *Natural fibers, biopolymers, and biocomposites*. Taylor & Francis Boca Raton, 2005.

[17] M. Z. Rahman, K. Jayaraman, and B. R. Mace. Vibration damping of flax fibre-reinforced polypropylene composites. *Fibers and Polymers*, 18(11):2187–2195, 2017.

[18] S. Prabhakaran, V. Krishnaraj, M. S. Kumar, and R. Zitoune. Sound and vibration damping properties of flax fiber reinforced composites. *Procedia Engineering*, 97:573–581, 2014.

[19] F. Duc, P. E. Bourban, C. J. G. Plummer, and J. A. E. Månson. Damping of thermoset and thermoplastic flax fibre composites. *Composites Part A: Applied Science and Manufacturing*, 64:115–123, 2014.

[20] T. Dias and R. Monaragala. Sound absorbtion in knitted structures for interior noise reduction in automobiles. *Measurement Science and Technology*, 17(9):2499, 2006.

[21] Flexform technologies. www.naturalfibersforautomotive.com/. Accessed: 2018-09-11.

[22] D. B. Dittenber and H. V. S Gangarao. Critical review of recent publications on use of natural composites in infrastructure. *Composites Part A: Applied Science and Manufacturing*, 43(8):1419–1429, 2012.

[23] O. Faruk, A. K. Bledzki, H. P. Fink, and M. Sain. Biocomposites reinforced with natural fibers: 2000–2010. *Progress in Polymer Science*, 37(11):1552–1596, 2012.

[24] DU Shah, PJ Schubel, and MJ Clifford. Can flax replace e-glass in structural composites? a small wind turbine blade case study. *Composites Part B: Engineering*, 52:172–181, 2013.

[25] P. Wambua, J. Ivens, and I. Verpoest. Natural fibres: can they replace glass in fibre reinforced plastics? *Composites Science and Technology*, 63(9):1259–1264, 2003.

[26] L. Yan, N. Chouw, and K. Jayaraman. Flax fibre and its composites–a review. *Composites Part B: Engineering*, 56:296–317, 2014.

[27] C. Baley, F. Busnel, Y. Grohens, and O. Sire. Influence of chemical treatments on surface properties and adhesion of flax fibre–polyester resin. *Composites Part A: Applied Science and Manufacturing*, 37(10):1626–1637, 2006.

[28] A. Lefeuvre, A. Bourmaud, C. Morvan, and C. Baley. Tensile properties of elementary fibres of flax and glass: Analysis of reproducibility and scattering. *Materials Letters*, 130: 289–291, 2014.

[29] K. Van de Velde and E. Baetens. Thermal and mechanical properties of flax fibres as potential composite reinforcement. *Macromolecular Materials and Engineering*, 286(6):342–349, 2001.

[30] K. Charlet, C. Baley, C. Morvan, J. P. Jernot, M. Gomina, and J. Bréard. Characteristics of Hermès flax fibres as a function of their location in the stem and properties of the derived unidirectional composites. *Composites Part A: Applied Science and Manufacturing*, 38(8): 1912–1921, 2007.

[31] K. H. Kromer. Physical properties of flax fibre for non-textile-use. *Research in Agricultural Engineering*, 55(2):52–61, 2009.

[32] E. Locatelli. Private Communication, 2015.

[33] J. Gassan, A. Chate, and A. K. Bledzki. Calculation of elastic properties of natural fibers. *Journal of Materials Science*, 36(15):3715–3720, 2001.

[34] A. V. R. Prasad and K. M. Rao. Mechanical properties of natural fibre reinforced polyester composites: Jowar, sisal and bamboo. *Materials & Design*, 32(8-9):4658–4663, 2011.

[35] H. L. Bos, M. J. A. Van Den Oever, and O. C. J. J. Peters. Tensile and compressive properties of flax fibres for natural fibre reinforced composites. *Journal of Materials Science*, 37(8): 1683–1692, 2002.

[36] C. Baley. Analysis of the flax fibres tensile behaviour and analysis of the tensile stiffness increase. *Composites Part A: Applied Science and Manufacturing*, 33(7):939–948, 2002.

[37] K. Charlet, J. P. Jernot, M. Gomina, C. Baley, L. Bizet, and J. Bréard. Morphology and mechanical behavior of a natural composite: the flax fiber. In *16th International Conference on Composite Materials. Kyoto, Japan*, 2007.

[38] A. Lefeuvre, A. Bourmaud, C. Morvan, and C. Baley. Elementary flax fibre tensile properties: Correlation between stress–strain behaviour and fibre composition. *Industrial Crops and Products*, 52:762–769, 2014.

[39] A. Thuault, S. Eve, J. Bazin, K. Charlet, F. Destaing, M. Gomina, and J. Bréard. Morphologie, biocomposition et comportement mécanique des fibres de lin. *Matériaux & Techniques*, 99(3):275–280, 2011.

[40] C. Baley and A. Bourmaud. Average tensile properties of french elementary flax fibers. *Materials letters*, 122:159–161, 2014.

[41] A. Bourmaud, A. Le Duigou, C. Gourier, and C. Baley. Influence of processing temperature on mechanical performance of unidirectional polyamide 11–flax fibre composites. *Industrial Crops and Products*, 84:151–165, jun 2016. ISSN 09266690. doi: 10.1016/j.indcrop.2016.02.007. URL `http://dx.doi.org/10.1016/j.indcrop.2016.02.007http://linkinghub.elsevier.com/retrieve/pii/S0926669016300759`.

[42] C. Baley, A. Le Duigou, A. Bourmaud, and P. Davies. Influence of drying on the mechanical behaviour of flax fibres and their unidirectional composites. *Composites Part A: Applied Science and Manufacturing*, 43(8):1226–1233, 2012.

[43] J. M. Michel. Contribution à l'histoire industrielle des polymères en france. *Société Chimique de France (Avril 2012)*, 2013.

[44] Arkema. `https://www.arkema.com/en/`. Accessed: 2018-06-28.

[45] V. Girard. *Amélioration d'un procédé propre de production de poudre de polyamide 11*. PhD thesis, Vandoeuvre-les-Nancy, INPL, 2011.

[46] C. Gourier. *Contribution à l'étude de matériaux biocomposites à matrice thermoplastique polyamide-11 et renforcés par des fibres de lin*. PhD thesis, Université Bretagne Sud, 2016. URL `https://tel.archives-ouvertes.fr/tel-01445578`.

[47] P. Zierdt, T. Theumer, G. Kulkarni, V. Däumlich, J. Klehm, U. Hirsch, and A. Weber. Sustainable wood-plastic composites from bio-based polyamide 11 and chemically modified beech fibers. *Sustainable Materials and Technologies*, 6:6–14, 2015.

[48] M. Feldmann and A. K. Bledzki. Bio-based polyamides reinforced with cellulosic fibres–processing and properties. *Composites Science and Technology*, 100:113–120, 2014.

[49] L. Martino, L. Basilissi, H. Farina, M. A. Ortenzi, E. Zini, G. Di Silvestro, and M. Scandola. Bio-based polyamide 11: synthesis, rheology and solid-state properties of star structures. *European Polymer Journal*, 59:69–77, 2014.

[50] R. Patel, D. A. Ruehle, J. R. Dorgan, P. Halley, and D. Martin. Biorenewable blends of polyamide-11 and polylactide. *Polymer Engineering & Science*, 54(7):1523–1532, 2014.

[51] P. Frübing, A. Kremmer, R. Gerhard-Multhaupt, A. Spanoudaki, and P. Pissis. Relaxation processes at the glass transition in polyamide 11: From rigidity to viscoelasticity. *The Journal of Chemical Physics*, 125(21):214701, 2006.

[52] Y. Lebaupin. *Comportement à l'impact et post-impact d'un composite lin/polyamide 11 élaboré par thermocompression*. PhD thesis, ISAE-ENSMA Ecole Nationale Supérieure de Mécanique et d'Aérotechique-Poitiers, 2016.

[53] F. Destaing. *Contribution à l'étude du comportement mécanique de matériaux composites biosourcés lin/PA11 élaborés par thermocompression*. PhD thesis, Université de Caen Basse-Normandie, 2012.

[54] K. G. Satyanarayana, G. G. C. Arizaga, and F. Wypych. Biodegradable composites based on lignocellulosic fibers—an overview. *Progress in Polymer Science*, 34(9):982–1021, 2009.

[55] P. Ouagne, L. Bizet, C. Baley, and J. Bréard. Analysis of the film-stacking processing parameters for plla/flax fiber biocomposites. *Journal of Composite Materials*, 44(10):1201–1215, 2010.

[56] R. Ali, S. Iannace, and L. Nicolais. Effects of processing conditions on the impregnation of glass fibre mat in extrusion/calendering and film stacking operations. *Composites Science and Technology*, 63(15):2217–2222, 2003.

[57] S. K. Garkhail, E. Meurs, T. Van de Beld, and T. Peijs. Thermoplastic composites based on biopolymers and natural fibres. In *ICCM-12 Europe 12th International Conference on Composite Materials. Paris, France*, 05-09 July 1999.

[58] E. Bodros, I. Pillin, N. Montrelay, and C. Baley. Could biopolymers reinforced by randomly scattered flax fibre be used in structural applications? *Composites Science and Technology*, 67(3-4):462–470, 2007.

[59] M. Bernard, A. Khalina, A. Ali, R. Janius, M. Faizal, K. S. Hasnah, and A. B. Sanuddin. The effect of processing parameters on the mechanical properties of kenaf fibre plastic composite. *Materials & Design*, 32(2):1039–1043, 2011.

[60] M. D. Wakeman, T. A. Cain, C. D. Rudd, R. Brooks, and A. C. Long. Compression moulding of glass and polypropylene composites for optimised macro-and micro-mechanical properties ii. glass-mat-reinforced thermoplastics. *Composites Science and Technology*, 59(5):709–726, 1999.

[61] A. Le Duigou, A. Bourmaud, C. Gourier, and C. Baley. Multi-scale shear properties of flax fibre reinforced polyamide 11 biocomposites. *Composites Part A: Applied Science and Manufacturing*, 85:123–129, jun 2016. ISSN 1359835X. doi: 10.1016/j.compositesa.2016.03.014. URL `http://dx.doi.org/10.1016/j.compositesa.2016.03.014http://linkinghub.elsevier.com/retrieve/pii/S1359835X16300318`.

[62] Y. Lebaupin, M. Chauvin, T. Q. Truong Hoang, F. Touchard, and A. Beigbeder. Influence of constituents and process parameters on mechanical properties of flax fibre-reinforced polyamide 11 composite. *Journal of Thermoplastic Composite Materials*, 30(11):1503–1521, nov 2017. ISSN 0892-7057. doi: 10.1177/0892705716644669.

[63] S. H. Aziz and M. P. Ansell. The effect of alkalization and fibre alignment on the mechanical and thermal properties of kenaf and hemp bast fibre composites: Part 1–polyester resin matrix. *Composites Science and Technology*, 64(9):1219–1230, 2004.

[64] K. C. M. Nair, S. Thomas, and G. Groeninckx. Thermal and dynamic mechanical analysis of polystyrene composites reinforced with short sisal fibres. *Composites Science and Technology*, 61(16):2519–2529, 2001.

[65] V. Michaud and J. A. E. Månson. Impregnation of compressible fiber mats with a thermoplastic resin. part i: theory. *Journal of Composite Materials*, 35(13):1150–1173, 2001.

[66] D. U. Shah. Developing plant fibre composites for structural applications by optimising composite parameters: a critical review. *Journal of Materials Science*, 48(18):6083–6107, 2013.

[67] B. Madsen. *Properties of plant fibre yarn polymer composites*. PhD thesis, Technical University of Denmark, 2004.

[68] M. T. Shaw and W. J. MacKnight. *Introduction to polymer viscoelasticity*. John Wiley & Sons, 2018.

[69] A. K. Bledzki, V. E. Sperber, and O. Faruk. *Natural and wood fibre reinforcement in polymers*, volume 13. Smithers Rapra Publishing, 2002.

[70] D. S. de Vasconcellos, F. Sarasini, F. Touchard, L. Chocinski-Arnault, M. Pucci, C. Santulli, J. Tirillò, S. Iannace, and L. Sorrentino. Influence of low velocity impact on fatigue behaviour of woven hemp fibre reinforced epoxy composites. *Composites Part B: Engineering*, 66:46–57, 2014.

[71] H. N. Dhakal, Z. Y. Zhang, M. O. W. Richardson, and O. A. Z. Errajhi. The low velocity impact response of non-woven hemp fibre reinforced unsaturated polyester composites. *Composite Structures*, 81(4):559–567, 2007.

[72] S. H. Jansma, B. Rietman, L. Warnet, R. Akkerman, and S. V. Lomov. Influence of moisture content on impact properties of flax fibre reinforced polymers. In *TexCompu-11 conference. Leuven, Belgium*, 16-20 September 2013.

[73] Y. Lebaupin, T. Q. Hoang, M. Chauvin, and F. Touchard. Influence of the stacking sequence on the low-energy impact resistance of flax/pa11 composite. *Journal of Composite Materials*, page 0021998319837339, 2019.

[74] S. V. Joshi, L. T. Drzal, A. K. Mohanty, and S. Arora. Are natural fiber composites environmentally superior to glass fiber reinforced composites? *Composites Part A: Applied Science and Manufacturing*, 35(3):371–376, 2004.

[75] N. P. J. Dissanayake, J. Summerscales, S. M. Grove, and M. M. Singh. Energy use in the production of flax fiber for the reinforcement of composites. *Journal of Natural Fibers*, 6 (4):331–346, 2009.

[76] Groupe Depestele. `http://www.groupedepestele.com/`. Accessed: 2018-06-28.

[77] M. Rask, B. Madsen, B. F. Sørensen, J. L. Fife, K. Martyniuk, and E. M. Lauridsen. In situ observations of microscale damage evolution in unidirectional natural fibre composites. *Composites Part A: Applied Science and Manufacturing*, 43(10):1639–1649, 2012.

[78] C. Gourier, A. Le Duigou, A. Bourmaud, and C. Baley. Mechanical analysis of elementary flax fibre tensile properties after different thermal cycles. *Composites Part A: Applied Science and Manufacturing*, 64:159–166, sep 2014. ISSN 1359835X. doi: 10.1016/j.compositesa.2014.05.006. URL `http://dx.doi.org/10.1016/j.compositesa.2014.05.006http://linkinghub.elsevier.com/retrieve/pii/S1359835X14001419`.

[79] D. U. Shah, P. J. Schubel, M. J. Clifford, and P. Licence. The tensile behavior of off-axis loaded plant fiber composites: An insight on the nonlinear stress–strain response. *Polymer Composites*, 33(9):1494–1504, 2012.

[80] D. P. Raghavalu Thirumalai, H. Lilholt, F. Aviles, T. Løgstrup Andersen, and H. Knudsen. Fibre waviness and misalignment measurement of unidirectional glass/LPET commingled composites-Effect on mechanical properties. In *34th Risø International Symposium on Materials Science. Lyngby, Denmark*, volume 34, pages 349–363, 02-05 September 2013.

[81] X. Yang, A. Nanni, S. Haug, and C. L. Sun. Strength and modulus degradation of carbon fiber-reinforced polymer laminates from fiber misalignment. *Journal of Materials in Civil Engineering*, 14(4):320–326, 2002.

[82] C. Poilâne, Z. E. Cherif, F. Richard, A. Vivet, B. Ben Doudou, and J. Chen. Polymer reinforced by flax fibres as a viscoelastoplastic material. *Composite Structures*, 112:100–112, 2014.

[83] V. Placet and M. Cissé, O.and Boubakar. Nonlinear tensile behaviour of elementary hemp fibres. part i: Investigation of the possible origins using repeated progressive loading with in situ microscopic observations. *Composites Part A: Applied Science and Manufacturing*, 56:319–327, 2014.

[84] J. Andersons, J. Modniks, and E. Spārniņš. Modeling the nonlinear deformation of flax-fiber-reinforced polymer matrix laminates in active loading. *Journal of Reinforced Plastics and Composites*, 34(3):248–256, 2015.

[85] D.H. Page and F. El-Hosseiny. mechanical properties of single wood pulp fibres. vi. fibril angle and the shape of the stress-strain curve. *Pulp & paper Canada*, 1983.

[86] P. Navi, P. K Rastogi, V. Gresse, and A. Tolou. Micromechanics of wood subjected to axial tension. *Wood Science and Technology*, 29(6):411–429, 1995.

[87] G. Coroller, A. Lefeuvre, A. Le Duigou, A. Bourmaud, G. Ausias, T. Gaudry, and C. Baley. Effect of flax fibres individualisation on tensile failure of flax/epoxy unidirectional composite. *Composites Part A: Applied Science and Manufacturing*, 51:62–70, 2013.

[88] F. Amenini, J. Brocail, M. Chauvin, and S. Thuillier. Dynamical properties of flax fibre reinforced pa11 over a large frequency range. *Composites Science and Technology*, 171: 234–243, 2019.

[89] D. D. L. Chung. Materials for vibration damping. *Journal of Materials Science*, 36(24): 5733–5737, 2001.

[90] M. Rueppel, J. Rion, C. Dransfeld, C. Fischer, and K. Masania. Damping of carbon fibre and flax fibre angle-ply composite laminates. *Composites Science and Technology*, 146: 1–9, 2017.

[91] S. A. Suarez, R. F. Gibson, C. T. Sun, and S. K. Chaturvedi. The influence of fiber length and fiber orientation on damping and stiffness of polymer composite materials. *Experimental Mechanics*, 26(2):175–184, 1986.

[92] R. F. Gibson, S. J. Hwang, and H. Kwak. Micromechanical modeling of damping in composites including interphase effects. In *Proceedings of 36th International SAMPE Symposium. San Diego, California*, volume 1, pages 592–606, 15-18 April 1991.

[93] D. J. Nelson and J. W. Hancock. Interfacial slip and damping in fibre reinforced composites. *Journal of Materials Science*, 13(11):2429–2440, 1978.

[94] K. P. Menard. *Dynamic mechanical analysis: a practical introduction*. CRC press, 2008.

[95] R. M. Crane and J. W. Gillespie Jr. Characterization of the vibration damping loss factor of glass and graphite fiber composites. *Composites Science and Technology*, 40(4):355–375, 1991.

[96] S. Mahmoudi, A. Kervoelen, G. Robin, L. Duigou, E.M. Daya, and J.M. Cadou. Experimental and numerical investigation of the damping of flax–epoxy composite plates. *Composite Structures*, 208, 10 2018. doi: 10.1016/j.compstruct.2018.10.030.

[97] M. Berges, R. Léger, V. Placet, V. Person, S. Corn, X. Gabrion, J. Rousseau, E. Ramasso, P. Ienny, and S. Fontaine. Influence of moisture uptake on the static, cyclic and dynamic behaviour of unidirectional flax fibre-reinforced epoxy laminates. *Composites Part A: Applied Science and Manufacturing*, 88:165–177, 2016.

[98] P. Butaud, V. Placet, J. Klesa, M. Ouisse, E. Foltête, and X. Gabrion. Investigations on the frequency and temperature effects on mechanical properties of a shape memory polymer (veriflex). *Mechanics of Materials*, 87:50–60, 2015.

[99] C. W. Bert. Material damping: An introductory review of mathematic measures and experimental technique. *Journal of Sound and Vibration*, 29(2):129–153, 1973.

[100] J. Berthaut, M. N. Ichchou, and L. Jezequel. K-space identification of apparent structural behaviour. *Journal of Sound Vibration*, 280:1125–1131, 2005.

[101] C. R. Halkyard. Maximum likelihood estimation of flexural wavenumbers in lightly damped plates. *Journal of Sound and Vibration*, 300(1-2):217–240, 2007.

[102] M. Rak, M. Ichchou, and J. Holnicki-Szulc. Identification of structural loss factor from spatially distributed measurements on beams with viscoelastic layer. *Journal of Sound and Vibration*, 310(4-5):801–811, 2008.

[103] R. Cherif, J. D. Chazot, and N. Atalla. Damping loss factor estimation of two-dimensional orthotropic structures from a displacement field measurement. *Journal of Sound and Vibration*, 356:61–71, 2015.

[104] R. Viala, V. Placet, and S. Cogan. Identification of the anisotropic elastic and damping properties of complex shape composite parts using an inverse method based on finite element model updating and 3d velocity fields measurements (femu-3dvf): Application to bio-based composite violin soundboards. *Composites Part A: Applied Science and Manufacturing*, 106:91–103, 2018.

[105] C. Pezerat. *Méthode d'identification des efforts appliqués sur une structure vibrante, par résolution et régularisation du problème inverse*. PhD thesis, INSA de Lyon, 1996.

[106] C. Pezerat and J. L. Guyader. Two inverse methods for localization of external sources exciting a beam. *Acta Acustica*, 3(1):1–10, 1995.

[107] C. Pezerat and J. L. Guyader. Force analysis technique: reconstruction of force distribution on plates. *Acta Acustica united with Acustica*, 86(2):322–332, 2000.

[108] M. C. Djamaa, N. Ouelaa, C. Pezerat, and J. L. Guyader. Reconstruction of a distributed force applied on a thin cylindrical shell by an inverse method and spatial filtering. *Journal of Sound and Vibration*, 301(3-5):560–575, 2007.

[109] C. Renzi and C. Pezerat. Identification of dynamic excitations on a structure using displacement measurements injected in a finite element model. In *Noise and Vibration in Emerging Methods 2009. Ibiza, Spain*, 07-09 May 2009.

[110] Q. Leclere and C. Pézerat. Vibration source identification using corrected finite difference schemes. *Journal of Sound and Vibration*, 331(6):1366–1377, 2012.

[111] F. Ablitzer, C. Pézerat, J. M. Génevaux, and J. Bégué. Identification of stiffness and damping properties of plates by using the local equation of motion. *Journal of Sound and Vibration*, 333(9):2454–2468, 2014. doi: 10.1016/j.jsv.2013.12.013.

[112] F. Ablitzer, C. Pézerat, B. Lascoup, and J. Brocail. Identification of the flexural stiffness parameters of an orthotropic plate from the local dynamic equilibrium without a priori knowledge of the principal directions. *Journal of Sound and Vibration*, 404:31–46, 2017.

[113] B. Lascoup, F. Ablitzer, and C. Pézerat. Broadband identification of material properties of an orthotropic composite plate using the force analysis technique. *Experimental Mechanics*, 58(9):1339–1350, 2018.

[114] Q. Leclère, F. Ablitzer, and C. Pézerat. Practical implementation of the corrected force analysis technique to identify the structural parameter and load distributions. *Journal of Sound and Vibration*, 351:106–118, 2015.

[115] T. Wassereau, F. Ablitzer, C. Pézerat, and J.L. Guyader. Experimental identification of flexural and shear complex moduli by inverting the timoshenko beam problem. *Journal of Sound and Vibration*, 399:86–103, 2017.

[116] M.E. McIntyre and J. Woodhouse. On measuring the elastic and damping constants of orthotropic sheet materials. *Acta Metallurgica*, 36(6):1397–1416, 1988.

[117] L. Sevgi. *A Practical Guide to EMC Engineering*. Artech House electromagnetic analysis series. Artech House, 2017. ISBN 9781630814007. URL `https://books.google.fr/books?id=r4Q0DwAAQBAJ`.

[118] K. M. M. Prabhu. *Window functions and their applications in signal processing*. CRC press, 2013.

[119] MATLAB. *version 9.0.0 (R2016a)*. The MathWorks Inc., Natick, Massachusetts, 2016.

[120] T. Proulx. *Application of Imaging Techniques to Mechanics of Materials and Structures, Volume 4: Proceedings of the 2010 Annual Conference on Experimental and Applied Mechanics*, volume 14. Springer Science & Business Media, 2012.

[121] T. Siebert, R. Wood, and K. Splitthof. High speed image correlation for vibration analysis. In *Journal of Physics: Conference Series*, volume 181, page 012064. IOP Publishing, 2009.

[122] W. Wang, J. E. Mottershead, A. Ihle, T. Siebert, and H. R. Schubach. Finite element model updating from full-field vibration measurement using digital image correlation. *Journal of Sound and Vibration*, 330(8):1599–1620, 2011.

[123] F. Trebuňa and M. Hagara. Experimental modal analysis performed by high-speed digital image correlation system. *Measurement*, 50:78–85, 2014.

[124] F. Amenini. Impiego della correlazione delle immagini nell'ambito dell'analisi modale sperimentale. Master's thesis, Politecnico di Milano, 2015.

[125] R. Huňady and M. Hagara. A new procedure of modal parameter estimation for high-speed digital image correlation. *Mechanical Systems and Signal Processing*, 93:66–79, 2017.

[126] G Musotto. Digital image correlation: applicazione di tecniche convenzionali e sviluppo di soluzioni innovative per la stima e l'incremento dell'accuratezza. Master's thesis, Politecnico di Milano, 2012.

[127] F. Ablitzer. Private Communication, 2017.

[128] M. N. Helfrick, C. Niezrecki, P. Avitabile, and T. Schmidt. 3d digital image correlation methods for full-field vibration measurement. *Mechanical systems and signal processing*, 25(3):917–927, 2011.

[129] T. J. Beberniss and D. A. Ehrhardt. High-speed 3d digital image correlation vibration measurement: Recent advancements and noted limitations. *Mechanical Systems and Signal Processing*, 86:35–48, 2017.

[130] S. Zouari. *Bandes interdites d'ondes de flexion dans une méta-plaque composite: effet de finitude de la structure et des dispersions de fabrication*. PhD thesis, Le Mans, 2017.

[131] J. D. Ferry. *Viscoelastic properties of polymers*. John Wiley & Sons, 1980.

[132] Y. Lebaupin. Private Communication, 2016.

[133] H. Daoud, J. L. Rebiere, A. El Mahi, M. Taktak, and M. Haddar. Propriétés dynamiques d'un composite en fibres de lin avec une couche viscoélastique naturelle. In *Journées Nationales sur les Composites 2017, Paris, France*, 28-30 September 2017.

Appendices

A

Impact de la dispersion de l'orientation des plis sur le comportement vibratoire d'un éco-composite stratifié

The present poster has been presented at the conference "Jounées Jeunes Chercheurs", the 6-7 April 2016 in Clermont-Ferrand, France.

It deals with a numerical modal analysis on a FF/PA11 plate. In order to take into account the effect of the variability which could occur in the fibre alignment and to analyse its effect on the dynamic plate behaviour, several angle configurations are compared. A FF/PA11 plate manufactured by film stacking and hot moulding process with 8 layers of unidirectional FF and PA11 films in such a way that the fibre volume ratio is equal to 40 %, is used to carried out a preliminary experimental modal analysis. For this purpose, a plate of dimensions 250 mm (in fibre direction) $\times$ 100 mm (in transverse direction), is suspended to a frame and excited by using a PCB 086C03 impact hammer which allows to record the force signal. The plate is excited in several points arranged on a regular grid (9 points $\times$ 4 points). A PCB accelerometer is glued on a point of the grid and used to record the acceleration in that point. In order to reduce the measurement noise, the impacting force and the acceleration are recorded and averaged 5 times. Once the signals are recorded in time domain the signal in frequency domain is calculated. A range of frequencies between 0 Hz and 600 Hz is excited. The experimental modal analysis performed on the recorded signals allows to calculate the natural frequencies and the mode shape of the plate over the excited

range of frequencies. Over the frequency range taken into account, three vibration modes are identified: the first one at frequency f = 193 Hz is characterized by a torsional mode shape, the second one corresponding to a flexural mode has a natural frequency f = 338 Hz and the third one, characterized by a combination of torsional and flexural shape, at frequency f = 528 Hz.

To perform the numerical modal analysis, the Finite Element software Abaqus is used. A linear elastic material having density $\rho = 1200\,\mathrm{kg\,m^{-3}}$, Young's moduli in fibre and transverse direction respectively $E_x = 34$ GPa and $E_y = 4$ GPa, Poisson's ratio 0.4 and shear moduli $G_{xy} = 1.6$ GPa, $G_{yz} = 8$ GPa and $G_{xz} = 8$ GPa, is considered [132]. Such characteristics are applied at the 8 plies of material constituting the plate. The plate is then meshed using four-node shell elements. A modal analysis is then performed to obtain the first 30 natural frequencies and mode shapes. In order to validate the numerical model used in this study, results of the experimental modal analysis are used. The 3 experimental modes are compared with the first 3 modes calculated by the numerical modal analysis and a good correlation is obtained.

In order to analyse the influence of the ply angle on the dynamic behaviour of the plate, 4 different angle sequences are considered. A unidirectional configuration with all layers orientated with an angle equal to 0° taken as reference, is compared with a configuration for which all layers have an orientation angle of 2.5° and two other configurations for which the orientation angle is randomly chosen among three values (−2.5°, 0° and 2.5°) or in a range between −3° and 3°. For each configuration the modes shapes and natural frequencies are calculated. The compared results show that there is a good correlation of the natural frequencies of the first 30 modes for all configurations which results in a deviation lower than 5 %, confirming that values of fibre alignment lower than 3° have not an impact on the structure dynamic behaviour. In [133] an experimental modal analysis is conducted on flax fibre reinforced bio-epoxy rectangular specimens to compare the first 4 vibration modes. The specimens are cut from an unidirectional plate at several orientation angle: 0°, 15°, 30°, 45°, 60°, 75° and 90°. The experimental modal analysis is conducted exciting the specimens with an impact hammer and measuring the displacement field with a Laser Doppler Vibrometer, while the specimens are in a clamped-free configuration. A slight decrease of the obtained natural frequency values for the first 4 modes with an increment of the orientation angle up to 60°, is observed. In particular, the natural frequencies of the vibration mode decrease by less then 30 % from a 0° configuration to a 15° configuration.

IMPACT DE LA DISPERSION DE L'ORIENTATION DES PLIS SUR LE COMPORTEMENT VIBRATOIRE D'UN ECO-COMPOSITE STRATIFIE

F. AMENINI+*, J. BROCAIL*, M. CHAUVIN*, S. THUILLIER**
*ESTACA, rue Georges Charpak, BP 76121, F-53061 Laval Cedex 9, France
**Univ. Bretagne Sud, FRE CNRS 3744, IRDL, F-56100 Lorient, France
+ federico.amenini@estaca.fr

Contexte & Objectif

Pourquoi ?

Problématique ?

Variabilité des propriétés aux échelles microscopique, mésoscopique et macroscopique.

Que faire ?

Première approche de la variabilité :

influence de l'orientation des plis sur l'analyse modale d'une plaque en PA11 renforcée par des fibres continues en lin.

Expérimentation

Matériau

8 couches unidirectionnelles à 0° par thermocompression, t=8mm

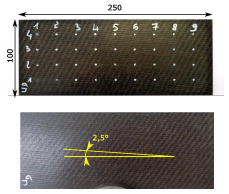

Défaut d'orientation

Propriétés du pli	
ρ	1200 kg/m³
E_x	34 GPa
E_y	4 GPa
ν	0,4
G_{xy}	1,6 GPa
G_{yz}	8 GPa
G_{xz}	8 GPa

→ Abaqus

Dispositif

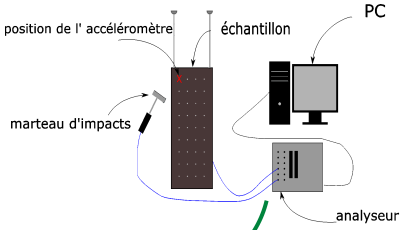

Acquistion temporelle sur chaque point

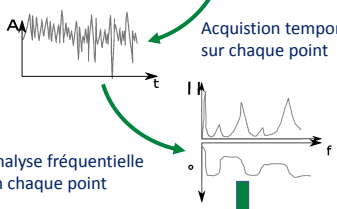

Analyse fréquentielle en chaque point

Cartographie de la réponse sur la plaque entière en libre/libre

Résultats

Expérimentaux

Orientation à 2,5°

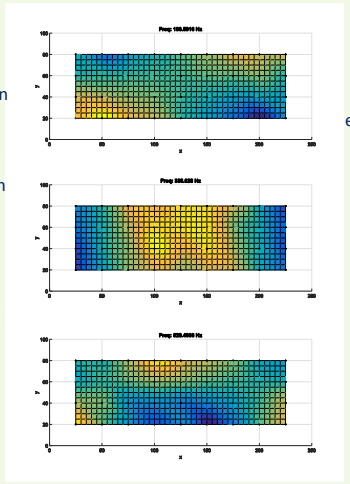

Mode 1, torsion
f = 193 Hz

Mode 2, flexion
f = 338 Hz

Mode 3, Flexion + torsion
f = 528 Hz

Corrélation expérimentale et numérique

Numériques

Orientation à 2,5°

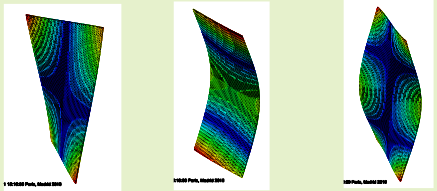

f = 195 Hz Mode 1 | f = 349 Hz Mode 2 | f = 527 Hz Mode 3

Orientation à 0°

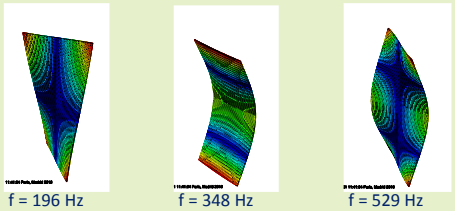

f = 196 Hz Mode 1 | f = 348 Hz Mode 2 | f = 529 Hz Mode 3

Défaut d'orientation

Changement d'orientation et analyse hautes fréquences

Séquence d'empilement

Pli	A[°]	B[°]	C[°]	D[°]
1	0	2,5	2,5	-2,08
2	0	2,5	2,5	-1,31
3	0	2,5	-2,5	-0,36
4	0	2,5	2,5	0,16
5	0	2,5	2,5	-0,26
6	0	2,5	0	2,25
7	0	2,5	2,5	0,11
8	0	2,5	-2,5	2,66

A : tous les plis de la plaque sont alignés avec le bord e la plaque
B : tous les plis sont désorientés de 2,5°
C & D : distribution aléatoire, soit limitée à trois valeur de désorientation, soit comprises entre -3° et 3°

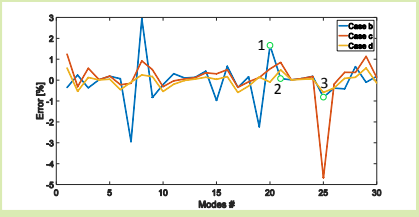

Ecart relatif entre les fréquences propres, A=ref

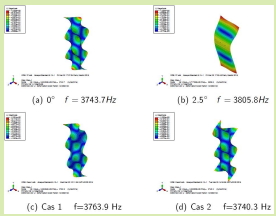

1 - Mode 20

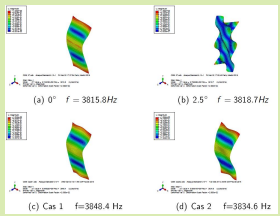

2 - Mode 21

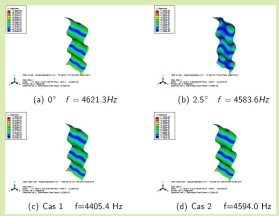

3 - Mode 25

Conclusion & Perspectives

Pour les fréquences propres inférieures à 600 Hz :
- Corrélation du modèle expérimental et numérique .

Pour les fréquences propres supérieures à 600 Hz :
- Inversion de quelques modes propres.

En perspective,
- Comparaison quantitative des déformées modales (indice de Mac);
- Mesures expérimentales à hautes fréquences par corrélation d'images ;
- Influence d'autres défauts sur l'analyse modale;
- Mise en place d'un modèle analytique.

Titre : Identification des propriétés dynamiques par une méthode basée sur la Force Analysis Technique : application au PA11 renforcé avec fibres de lin

Mots clés : Fibre de lin, PA11, comportement dynamique, amortissement, Force Analysis Technique

Résumé : Ce travail a pour objectif la caractérisation du comportement dynamique d'un matériau composite bio-sourcé au travers d'une méthode vibratoire. Dans le but d'étendre le champ d'application de ces matériaux au domaine vibratoire, une connaissance des propriétés dynamiques en fonction de la fréquence est nécessaire. A cet effet, une méthode a été appliquée pour identifier le module de stockage et le facteur de perte sur une vaste gamme de fréquences. Cette méthode basée sur la *Force Analysis Technique* utilise la mesure d'un champ de déplacements d'une plaque soumise à des vibrations. Dans un premier temps, le matériau, composé de fibres de lin unidirectionnelles et d'une matrice thermoplastique naturelle en PA11, a été élaboré par thermocompression. La microstructure est analysée par microscopie électronique en balayage et par tomographie et le comportement mécanique est caractérisé en condition quasi-statique. Dans un deuxième temps, une analyse de sensibilité de la méthode dynamique a été effectuée pour mettre en évidence les paramètres à prendre en compte lors de la mesure du champ des déplacements et du traitement des données. Deux techniques de mesure ont été comparées : la corrélation d'images et le vibromètre laser. Ensuite, l'identification du module de stockage et du facteur de perte a été faite sur une plage de fréquences jusqu'à 10000 Hz, en utilisant le champ de déplacement d'une plaque simplement suspendue et mise en vibrations avec un pot vibrant, mesuré avec un vibromètre laser. Afin de confirmer ces résultats, une comparaison a été réalisée avec les valeurs obtenues par une analyse mécanique dynamique (DMA) en appliquant le principe d'équivalence température – fréquence. En conclusion, la méthode citée permet une bonne identification du module de stockage du Lin/PA11 sur toute la gamme de fréquences.

Title : Identification of dynamic properties via a method based on Force Analysis Technique: application to flax fibre reinforced PA11

Keywords : Flax fibre, PA11, dynamic behaviour, damping, Force Analysis Technique

Abstract: The aim of this work is to characterize the dynamic behaviour of a biocomposite material using a vibratory method. In order to extend the application field of these materials to the vibration domain, the knowledge of the dynamic properties as a function of the frequency is necessary. For this purpose, a method is applied to identify the storage modulus and the loss factor over a large range of frequencies. This method, which is based on the Force Analysis Technique, uses the measurement of a vibrating plate displacement field. Firstly, the material, composed of a thermoplastic natural matrix PA11 reinforced by unidirectional flax fibres, is elaborated by thermocompression. The microstructure is analysed by scanning electron microscopy and tomography and the mechanical behavior is investigated under quasi-static conditions. In a second step, a sensitivity analysis of the dynamic method is carried out to highlight the parameters that should be taken into consideration during the displacement field measurement and the data post-treatment. Two measurement techniques are compared: the digital image correlation and the laser Doppler vibrometer. Afterwards, the identification of the storage modulus and the loss factor of the biocomposite flax/PA11 is obtained over a range of frequencies up to 10000 Hz, by using the displacement field of suspended plates measured with a laser vibrometer. In support of these results, a comparison is carried out with values obtained by a dynamic mechanical analysis (DMA) using the temperature-frequency superposition principle. In conclusion, the method gives a correct identification of the flax/PA11 storage modulus over the entire range of frequencies.